Free-surface film flow of a suspension and a related concentration instability

A Thesis
Presented to
The Academic Faculty

by

Brian D. Timberlake

In Partial Fulfillment
of the Requirements for the Degree of
Doctor of Philosophy in Chemical Engineering

School of Chemical and Biomolecular Engineering
Georgia Institute of Technology
March 2004

Free-surface film flow of a suspension and a related concentration instability

Approved by:

Peter J. Ludovice, Committee Chair

Jeffrey F. Morris, Adviser

Jay H. Lee

J. Carson Meredith

G. Paul Neitzel

Date Approved: 29 March 2004

To my parents,

Robert D. and Doris H. Timberlake,

without whose support this would not have been possible.

ACKNOWLEDGEMENTS

When I arrived at Georgia Tech, I did not know exactly what I intended to study. I met Dr. Jeffrey Morris as the instructor for my first graduate fluid dynamics class and remember being impressed with the level of sophistication that he expected from his students. I also remember enjoying the subject matter, although it was intimidating. I am thankful that I was able to spend my time at Georgia Tech under the supervision of Jeff. His academic integrity, endless enthusiasm for research, and high expectations for everyone he works with made him an ideal adviser. I sincerely thank him for the opportunity to explore the subject of fluid dynamics with his guidance and continuous support. I very much enjoyed working with him.

I want to acknowledge the effort made in reviewing this work by Dr. Jay Lee, Dr. Peter Ludovice, Dr. Carson Meredith, and Dr. G. Paul Neitzel. It has definitely been improved by their efforts.

I have enjoyed the comradery that I have had with Roy Furbank, Dave Desrocher, and Craig Sellars. My time at Georgia Tech would not have been nearly as enjoyable had it not been for their friendship.

I wish to thank Allison Yasitis who has given me daily encouragement and support, especially in the latter stages of this process. Her tolerance with me during this time, even while she recovers from surgery, has not gone unappreciated.

Finally, I am grateful for the support of my family who have continuously encouraged me over the past 5 years.

TABLE OF CONTENTS

LIST OF TABLES

LIST OF FIGURES

SUMMARY

Film flow of a suspension has been investigated both experimentally and theoretically. Gravity-driven free-surface inclined plane flow of a suspension of neutrally buoyant particles has been investigated using a stereoscopic particle imaging velocimetry technique. Particles have been shown to migrate away from the solid surface, and the film thickness has been shown to decrease as the fluid moves down the inclined plane. The free surface has been characterized using a light reflection technique, which shows that surface topography is affected by the inclination angle, and the particle concentration.

This flow has been modeled based on the normal stress approach of Morris and Boulay [1]. A boundary condition at the free surface has been examined, and model predictions have been compared with experimental results. The model predicts that the film thickness, relative to its initial value, will decrease with the bulk particle concentration.

The thin film flow over the inner cylinder in partially filled Couette flow of a suspension has been experimentally investigated as well as modeled. Concentration bands have been shown to form under a variety of different fill fractions, bulk particle concentrations, inclination angles, ratio of inner to outer cylinder, and rotation rates of the inner cylinder. The banding phenomena ranges from a regime where bands are

small, mobile and relatively similar in concentration to the bulk, to a regime where the concentration bands are larger, stationary, and where the space between them is completely devoid of particles.

The role of the film thickness in the band formation process has been investigated, and has led to a model for the band formation process based on a difference in the rate that fluid can drain from height fluctuations relative to the particles.

CHAPTER I

INTRODUCTION

1.1 Goals and motivation

Suspension mechanics, in the sense of particle motions and their effects upon bulk properties, is an area of active study in fluid mechanics. A group of problems which has received little attention from a suspension mechanical perspective is the behavior of a mixture of solids and liquid in the presence of a deformable interface. This is an important but little understood phenomenon and many engineering applications would benefit from a better understanding of how particles interact with each other in the presence of a free surface. These include coating flows, drop formation involving suspensions, and ceramic injection molding. This work will focus primarily on flows of suspensions involving thin films with a free surface, a class of flows which includes coating flows. A relatively simple suspension flow involving a free surface is gravity-driven flow down an inclined plane. This is the first problem we choose to address here.

Suspension film flow is one in which particle migration is reasonably expected to occur toward the free surface, with the question then arising of how the free surface interacts with the solid phase. The expectation comes from the fact that gravity-driven thin film suspension flow down an inclined plane is similar to pressure driven

flow of a suspension in a thin rectangular channel, which has been experimentally investigated by Koh *et al.* [2] as well as Lyon and Leal [3]. Lyon and Leal used a laser-Doppler velocimetry (LDV) method to determine the velocity profile in the flow as well as the particle concentration as a function of position. These authors found that particles migrate away from regions of high shear, near the walls, towards regions of low shear, in the center of the channel. This phenomenon has been seen in other flows such as Couette flow of a suspension [4, 5].

This expectation does not take any effects of the free surface into account. The presence of the free surface introduces capillary forces which are expected to balance the forces placed on the particles by shear induced migration on some scale. The steady developed flow on an inclined plane of a Newtonian fluid is equivalent to that seen in one half of a symmetric channel flow (neglecting the wall effect), and this flow is considered first. In this flow $u_x = |\frac{dP}{dz}|\frac{h}{\eta}\left[z - \frac{z^2}{2h}\right]$, where the channel is $2h$ wide, and z is zero at the wall and h at the centerline, and thus the shear rate $\dot{\gamma} = |\frac{dP}{dz}|\,[h - z]$ varies across the channel. As shown by a number of authors the particle migration may be explained by a phenomenological model based upon variation of the shear rate [6, 7, 8], or by the suspension normal stresses [1]. The latter modeling, where the migration is assumed to be the result of normal stresses created by the presence of the particles in the flow, has proven valid in a wide range of flows and provides an interpretation of value here. According to this model, the particle flux across the channel (in the z direction, $\perp$ to the walls) is

$$j_z \sim \frac{\partial}{\partial z}\Sigma_{zz} \sim \frac{\partial}{\partial z}(-\eta_n \dot{\gamma}) \tag{1.1}$$

where j_z is the z component of the particle flux, Σ_{zz} is the normal particle stress in the z direction, η_n is the dimensionless suspension viscosity, and $\dot{\gamma}$ is the shear rate. This implies that the particle flux is everywhere towards the center of the channel, with

strong accumulation at the centerline. This flux has been shown to require modeling of the stresses as nonlocal in shear rate [9] in order to avoid an aphysical maximum packing, based upon experiment [2] and simulation [7]. The flux expression in the case of the inclined plane flow is, again starting with $\nabla\phi = 0$, identical to (1.1), which leads to the strange prediction that particles will pass through the surface of the film. Experience shows that this does not occur, and that surface tension apparently comes into play to retain the particles in the film by exertion of a normal force on the particle phase to balance the particle phase Σ_{zz}. This balance between the bulk shearing effects and surface tension is the coupling of interest noted above and serves as a basic motivation for this problem.

The presence of a deformable interface introduces the problem of determining the domain of the flow, which is of unknown and transient shape. This requires determination of the interface shape as well as solution of the equations which govern the bulk fluid motion to obtain complete information about the flow. For the interests of this study the governing equations are Stokes equations, since we are interested in the case where the particle-scale Reynolds number is nearly zero, with the Reynolds number defined as $Re \equiv \frac{\rho\dot{\gamma}a^2}{\eta}$, where ρ is the fluid density, a is the particle diameter, and η is the fluid viscosity. While Stokes equations are linear, deformability of the interface causes the problem for the interface-plus-flow to be nonlinear. This nonlinearity is with respect to the driving force for the flow and arises because the interface introduces a balance between surface tension and viscous stresses, a particle scale capillary number ($Ca_p = \frac{2\rho g_x a^2}{\sigma}$), where g_x is the component of gravity in the flow direction, and σ is the surface tension. The balance between surface tension and viscous stresses has been examined numerous times for pure liquid drop deformation and breakup [10], and for the motion of single particles near an interface [11].

The linking of capillary forces and shear induced migration effects has been observed by Li and Pozrikidis [12, 13] using a boundary integral approach to simulate the particle motion and free surface shape for film flow of a suspension. They have studied liquid drops [12], and solid particles [13] in gravity-driven inclined plane flow of a suspension, where both the drops and solids were neutrally buoyant. They find that both the drops and the solid particles move away from the solid surface as well as the free surface, although the results for the solid particles are very limited. This result differs from their finding for liquid drops in pressure driven channel flow [14] where the drops only were found to move away from the solid walls.

The free surface of a suspension in simple shear driven by belts, where the free surface lies in the vorticity direction, has been studied experimentally by Loimer *et al.* [15]. Using a light refraction technique they find the one dimensional power spectral densities of light intensity from images of the free surfaces and notice that there are many different wave lengths present. The natural scale of surface deformations is that of the particles however, a range of scales showing a spectrum of 1/f type is observed.

In order to study the internal dynamics of free-surface flow of a suspension in gravity-driven inclined plane flow, we chose to use a stereoscopic particle imaging velocimetry technique, described in Chapter 2. The surface deformation, resulting from particle interactions in the bulk, has been characterized by a light reflection method, and can be seen at regular and high magnification in Figure 1.1. The dark spots in Figure 1.1 (c) are individual particles and the bright spots in all three images are locations on the surface which are reflecting light from a point source. We use direct surface imaging of reflected light from above, which is similar to Loimer *et al.*, to determine the surface topography under various conditions, with power spectral analysis of the images as a characterization tool. The light reflection technique is described in Chapter 2.

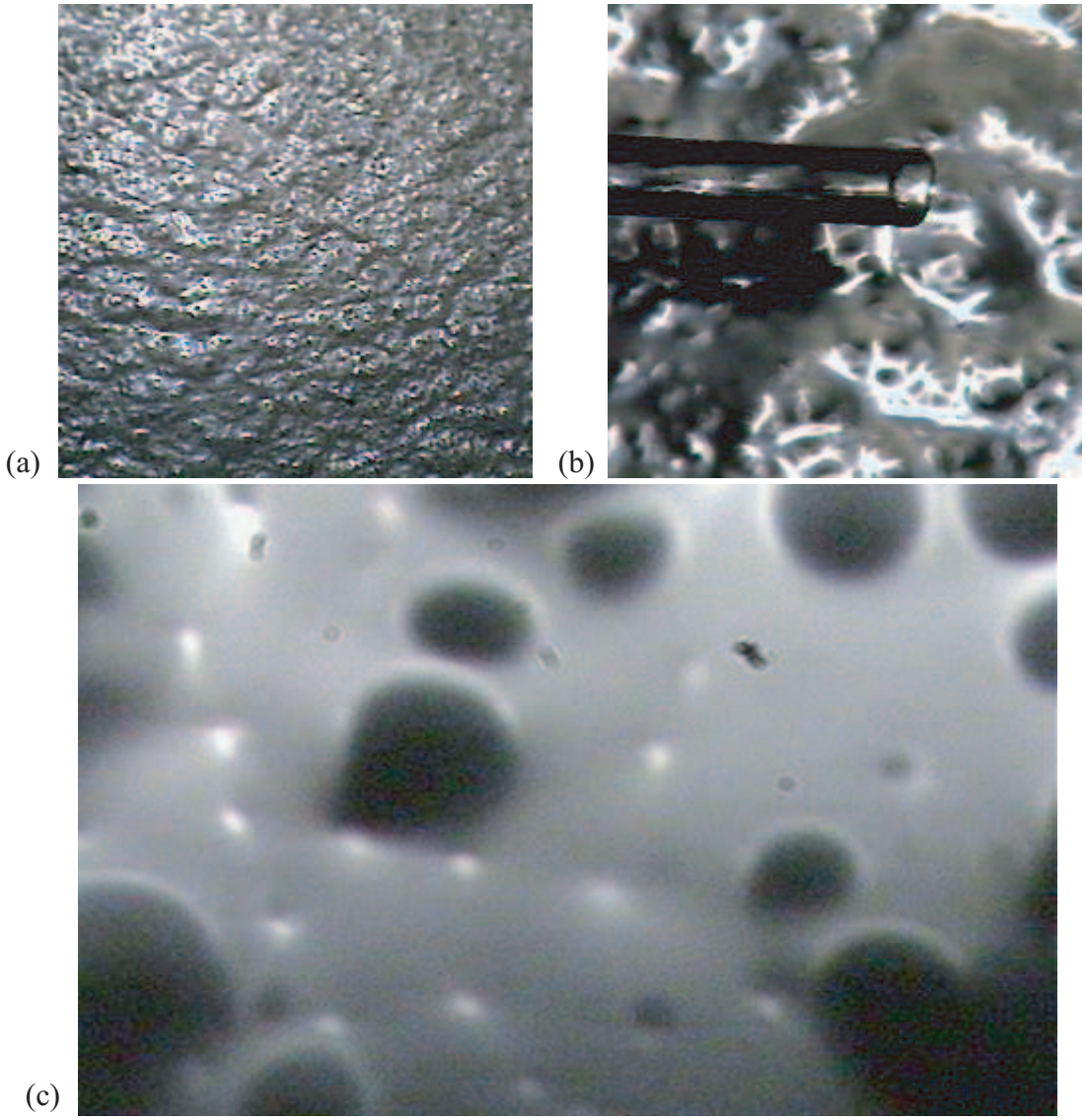

Figure 1.1: (a) Reflection of light from the free surface of a suspension flowing down an inclined plane, for $2\overline{a} = 178$ μm, $\alpha = 60.8^o$, $h_o = 2.1$ mm and $\phi = 0.30$ The image is 3.0 cm tall and 2.4 cm wide. (b) Image of a glass pipet with 1.7 mm diameter just above the free surface shown in (a) at slightly higher magnification. (c) Close up of light reflecting from the free surface for $2\overline{a} = 178$ μm, $h_o = 2.2$ mm, $\phi = 0.30$, and $\alpha = 34.6^o$. The image is 0.7 mm tall and 1 mm wide.

There are many instabilities associated with free surfaces at nonzero Reynolds number, and in the case of some free-surface flows instabilities are found even at vanishing Reynolds number [16]. The interest here is in instabilities which have been observed in rotating flows of free-surface suspensions. Specifically, we are interested in a phenomenon observed in the geometries of partially-filled concentric cylinders with the inner cylinder driving the flow [17, 18] and a partially-filled single rotating cylinder [19, 16]. In each geometry, an axial segregation of particles into alternating regions of high and low particle concentration, where the high concentration regions are referred to as concentration bands, has been reported. The present work examines the Couette geometry. Experiments have been performed for a variety of different bulk particle concentrations, fill fractions of the annulus, inclination angles of the device, ratios of inner to outer cylinder diameter, and rotation rates of the inner cylinder. These results are presented in Chapter 3 and 4.

The most striking behavior found here is due to inclination of the Couette device. When the device is placed at an incline a basic symmetry is broken and concentration bands are found to migrate down the axis, away from the elevated end with bands forming periodically in the shallow end of the device. This procedure happens in a very regular manner for sufficient inclination. When the system is unforced the concentration bands are found to meander back and forth in the device, at times coalescing to form a single band from two, with a new band forming to fill the newly opened space. An example of the band motion for the unforced ($\alpha = 0$) and forced ($\alpha = 2^o$) cases, where α is the inclination angle of the device, can be seen in Figure 1.2 (a) and (b) respectively. This motion looks very similar to solutions of the Kuramoto-Sivashinsky equations [20, 21],

$$h_t = -h \cdot h_x - a - b \cdot h_x - h_{xx} - c \cdot h_{xxx} - h_{xxxx}$$

which are known to exhibit chaotic behavior. Here h is meant to represent surface elevation of the film over the inner cylinder. Forcing by gravity is similar in effect to making the constants b or c nonzero. Examples of these solutions, with periodic boundary conditions, are shown in Figure 1.2 (c,d). The solution method for this equation is given in Trefethen [20].

For the related problem of rimming flow inside a rotating cylinder, it has been shown by lubrication analysis that flow with axially varying viscosity will cause a disturbance in the film thickness axially [22]. It is believed that a similar mechanism takes place for partially filled Couette flow of a suspension. Once the film thickness over the inner cylinder has been perturbed there is a difference in the rate that the particles can leave this local region of higher thickness relative to the rate the suspending fluid can leave. Particles are able to drain from the region at a rate which is slower than that of the fluid, thus increasing the particle fraction in the local region which has more height. This increases the effective viscosity of the disturbed region which then further increases the film thickness. This process of differential drainage [23, 24] then builds on itself to create alternating regions of high and low particle fraction. The concept underlying the mechanism is that there is a deviation in velocity between the phases in gravity-driven flow caused by the fluctuations in surface elevation. The deviation in phase velocities was demonstrated for the spreading of a drop of suspension in Chapter 3. The model, described in Chapter 4, gives rise to a set of coupled equations for volume fraction, axial velocity, and variation of the film depth.

1.2 Thesis Outline

The bulk of this work is made up of two papers which have been published and one which is intended to be submitted; because of this some results and methods are

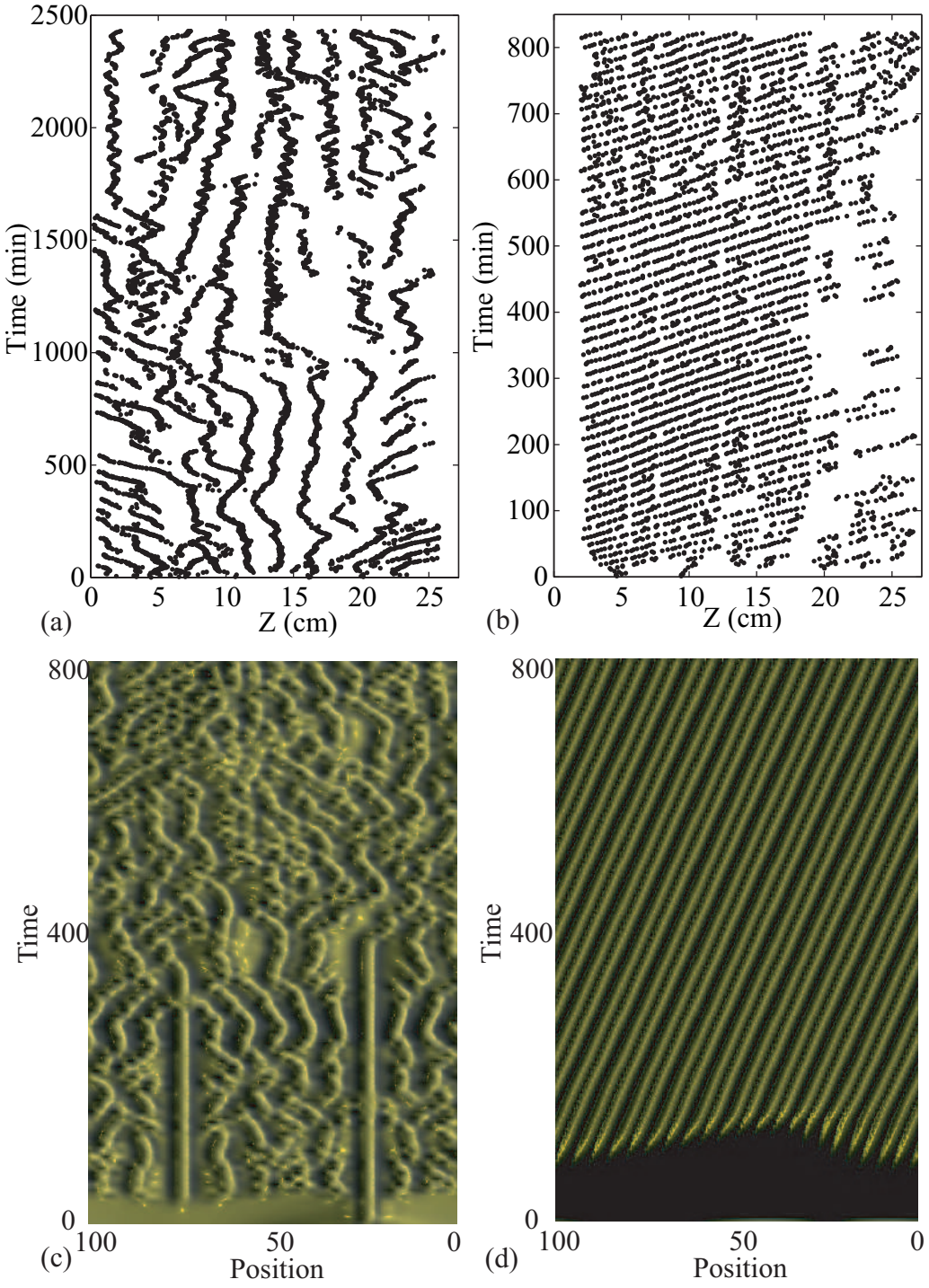

Figure 1.2: Spatiotemporal location of concentration bands in free-surface Couette flow of a suspension (a) Unforced no incline (b) Forced with inclination angle 2^o. Kuramoto-Sivashinsky solutions for (c) $a = 0$, $b = 0$, and $c = 0$ (d) $a = 0.2$, $b = 0$, and $c = 2$.

covered in multiple locations. The following is intended to outline this work for the benefit of the reader.

We approach our investigation of thin film free-surface suspension flow by experimentally obtaining information about free-surface inclined plane flow of a suspension. This problem is treated in Chapter 2. A stereoscopic PIV technique has been used to gain information about the velocity field and further analyzed to gain information about the particle concentration distribution. The free surface shape has been investigated using a light reflection technique, and images of the free surface and the corresponding power spectral density plots are presented. This flow has been modeled and comparisons have been made between the model and experimental data.

We then consider partially filled Couette flow of a suspension, a flow which has been shown to cause an instability in the particle concentration. Experiments have been performed exploring the effects of the bulk particle concentrations, fill fractions of the annulus, inclination angles of the device, ratios of inner to outer cylinder diameter, and rotation rates of the inner cylinder. The dynamics of the concentration bands has been investigated and detection methods and results are presented in Chapter 3. The relationship between the film depth over the inner cylinder and the banding phenomena has been investigated and results are presented in Chapter 4.

A mechanism for the banding phenomena has been proposed based on a difference in the rate that fluid is able to drain relative to the particles, from a height disturbance in the film. Once a height disturbance has occurred the process continues to build on itself, with the fluid draining faster than the particles, thereby increasing the effective viscosity locally and causing the height to increase further. Ideas concerning this mechanism are presented in Chapter 3, and a more complete formulation is presented in Chapter 4.

CHAPTER II

PARTICLE MIGRATION AND SURFACE TOPOGRAPHY IN FREE-SURFACE INCLINED PLANE FLOW OF A SUSPENSION

2.1 Introduction

Free-surface suspension flow has relevance to processes such as dip or blade coating [25], as well as paint coating [26]. Coating flows involving suspensions have, however, received little attention addressing the role of particles in establishing the bulk flow and the form of the surface. The latter issue has been shown to have relevance in recent work by Loimer, Nir and Semiat [15] illustrating that shear-induced motions of the particles can result in marked deformation of a suspension-air interface. This behavior reflects particle interactions in the bulk and has no obvious counterpart in pure liquid interfaces. To examine the phenomena involved in a suspension flow with a free surface, we have considered the relatively simple gravity-driven flow down an inclined plane. This work presents experimental results and flow modeling for this problem.

Based upon the similarity of the gravity-driven free-surface flow and pressure-driven channel flow, for the latter of which a suspension exhibits pronounced particle

migration [2, 3], migration is expected to play a role. A number of suspension flows exhibiting migration have been investigated. Leighton and Acrivos [4], and later Abbott *et al.* [5] have shown experimentally that particles will migrate away from regions of high shear to regions of low shear in Couette flow of a suspension. The experiments by Lyon and Leal [3] determined the velocity and concentration profile of pressure driven flow of a suspension of neutrally buoyant solid spherical particles in a rectangular channel, using a modified laser-Doppler velocimetry (LDV) method. Particle migration was away from the walls and toward the center of the channel, leading to the expectation in a gravity-driven film flow of a suspension that neutrally buoyant particles will accumulate adjacent to the free surface.

This expectation does not, however, account for factors arising from the free surface. The most obvious neglected point is that in a free-surface flow, deformation of the interface introduces capillary forces, a type absent in a channel flow. A related point is that the freedom of the interface shape introduces degrees of freedom in the system dynamics, and these have been shown in other geometries, namely a partially-filled circular Couette device and a single partially-filled rotating cylinder, to be associated with remarkably strong segregation of the particles into concentrated and dilute (or particle-free) bands along the direction perpendicular to the flow. In these flows with rotation about the axis of symmetry, banding is along the axis, and was observed to occur in low Reynolds number flow in the partially filled Couette [17, 18] and rimming flow inside a rotating cylinder [16]. Both flows involve a free-surface film of suspension flowing due to the device rotation and gravity. The finding of instability of the uniformly-mixed state in such flows indicates a need for examination of suspension flows in free-surface geometries.

The observations of Loimer *et al.* [15] that the interface with normal along vorticity in a simple shear flow is strongly deformed point to significant forces driving

particle interaction with the free surface. Our investigation considers suspension flow under conditions in which the normal stresses in the suspension are expected to play a more prominent role in the bulk through the particle migration [1]. Because capillary normal forces resist the protrusion of particles into the interface, the internal dynamics and surface deformation provide dual demonstrations of the influence of particle normal stresses. The vanishing of the average shear rate at the interface in the flow studied here provides direct evidence of the need for a nonlocal description of the dynamics in a flowing suspension. In order to study the internal dynamics of free-surface flow of a suspension, we chose to use a stereoscopic particle imaging velocimetry technique, described in §2.2.2. We use direct surface imaging of reflected light to determine the surface topography under various conditions, with power spectral analysis of the images as a characterization tool.The light reflection technique is described in §2.2.3

The expectations of particle migration toward the free surface of gravity-driven film flow are derived from a body of work modeling the bulk flow of suspensions [6, 7, 8, 1]. Leighton and Acrivos [8] proposed a phenomenological model for the shear induced particle flux along gradients in shear, which holds for some flows. Morris and Boulay [1] have developed a model for the particle flux based on normal stress differences caused by the presence of particles in sufficient concentration, and this model is employed, in §2.5, to model the axially evolving film flow.

Complementing modeling efforts are rather limited simulation studies examining the behavior of isolated particles or suspensions in film flow. The presence of a deformable interface introduces the problem of determining the domain, which is of unknown and transient shape. Li and Pozrikidis have used boundary integral techniques to simulate drops [12] and then particles [13] in two-dimensional gravity driven flow down an inclined plane. The results published for suspensions of solid

particles are limited, but the liquid drops were found to migrate to the center of the film, meaning away from both the solid and the free surface. This behavior differs from the findings for drops in pressure-driven channel flow by Li and Pozrikidis [14], providing direct (albeit numerical) evidence that the capillary forces from the film interface can have effects upon the bulk distribution in mixture film flows.

We begin by outlining the experiments in the following section. Experimental results are presented for the PIV and surface reflection studies in §2.3. The model is presented and its results are compared with experimental findings in §2.5.

2.2 Experiments

2.2.1 Suspensions and equipment

The suspending fluid used was a mixture of 76% Triton X-100 (t-Octylphenoxypoly-ethoxy-ethanol, a surfactant produced by Sigma), 16.2% zinc chloride (ZnCl), and 7.8% water, with the percentages based on mass. This mixture was density-matched ($\rho = 1.180$ g/cm^3) and roughly refractive index (RI)-matched to the poly-(methyl methacrylate) (PMMA; Elvacite Company) particles (RI = 1.491 at $T = 20^o$C). The suspending liquid viscosity had temperature dependence described by $\eta = 9.13 \cdot exp(-0.12(T - 22))$ Pa s, with T in degrees Celsius, based on measured viscosities at $T = 22^o$–28^oC. The surface tension of the suspending fluid is 33.5 dyne/cm at 23^oC, measured with a Fisher Surface Tensiometer Model 21.

Suspensions are mixed by first adding the Triton X-100 to the particles and allowing all of the resulting air bubbles to rise out. The $ZnCl_2$ is then dissolved in the water and this solution is added to the particles and Triton X-100. The suspension is then mixed and allowed to cool; cooling is needed as there is apparently a significant heat of mixing for $ZnCl_2$ and water as well as for aqueous $ZnCl_2$ and Triton X-100.

The PMMA particles used in the PIV experiments, described in §2.2.2, were sieved

to diameters ($2a$) in the range 250–300 μm, and heat treated as described below. The free surface characterization experiments, described in §2.2.3, used PMMA particles sieved to a diameter range of 106–250 μm, but which were not heat treated. A limited number of the free surface characterization experiments were done with PMMA particles that had diameters of 9.9 μm with a standard deviation of 1.4 μm (Bangs Laboratories).

Particles for use with the PIV techniques described in §2.2.2 must have the same refractive index as the suspending fluid and must also have a constant refractive index within the particle, so that only the dyed tracer particles can be seen in the flow. Improvement of the refractive index matching was obtained by the following procedure. Particles were placed for 15 minutes in an oil bath well-mixed by rapid magnetic stirring and heated to 130^{o}C, and then quenched with dry ice to -78^{o}C. The glass transition temperature of PMMA is 125^{o}C [27]. The particles were then resieved, a step needed to remove any which might have become fused. This process greatly improves the clarity of the PMMA particles, allowing visualization through the full depth of a 3 mm film of $\phi = 0.30$.

Tracer particles are required for PIV techniques and are created by allowing dye to diffuse into the PMMA particles. Several grams of PMMA particles are placed in a bath consisting of water and black RIT liquid dye. The bath is well mixed and heated until boiling. The particles are kept under these conditions for approximately two hours. The mixture is poured through a sieve to separate the particles from the bath. While the particles are still on the sieve, cold water is poured over them to remove any excess dye. Finally the dyed particles are re-sieved to remove fused particles.

Two inclined channels, both constructed from Lexan and 4.4 cm wide but differing in length, were used; one was 183 cm long and the other was 61 cm long. The longer channel was used to examine axial evolution by PIV as described in §2.2.2 and free

surface characterization as described in §2.2.3; the shorter channel was used only for experiments in which the free surface characterization was studied. To eliminate inclination of the device in the spanwise direction, the channel was leveled in the spanwise direction using a bubble level pressed flush against the solid surface of the inclined plane channel, and with its axis perpendicular to the channel (flow direction) axis. This was done at the top and bottom of the inclined plane just prior to each experiment.

Digital imaging was used in all experiments described. The cameras used were Ultrak model KC7500CN with Navitar Zoom 7000 Macro Zoom 18-108 mm F/2.5 lenses. Camera positioning is schematically illustrated in Figure 2.1. Images were captured and sent to computer memory by an IMASYS Falcon Quattro frame grabbing capture card, which is capable of taking images from 4 NTSC input lines simultaneously. Each image is marked with a time stamp when taken, accurate to one millisecond. For stereoscopic PIV, a pair of images is needed at each imaging time; pairs with time stamps differing by greater than one millisecond were discarded. The time between frames was 0.5 seconds or greater.

2.2.2 Particle imaging velocimetry

Stereoscopic particle imaging velocimetry (PIV) was used to determine the particle velocity within the film. The method consists of three basic steps. First, individual dyed tracer particles are identified in stereoscopic images. Second, their locations in a three dimensional coordinate system are determined by analysis of the image pairs. Third, once all particle positions are known for two instants within 2 seconds of each other in time, a correlation between particle positions in these two is performed to determine particle velocity as a function of location in the flow. The treatment of all data from an experiment consists of performing the first and second steps on all

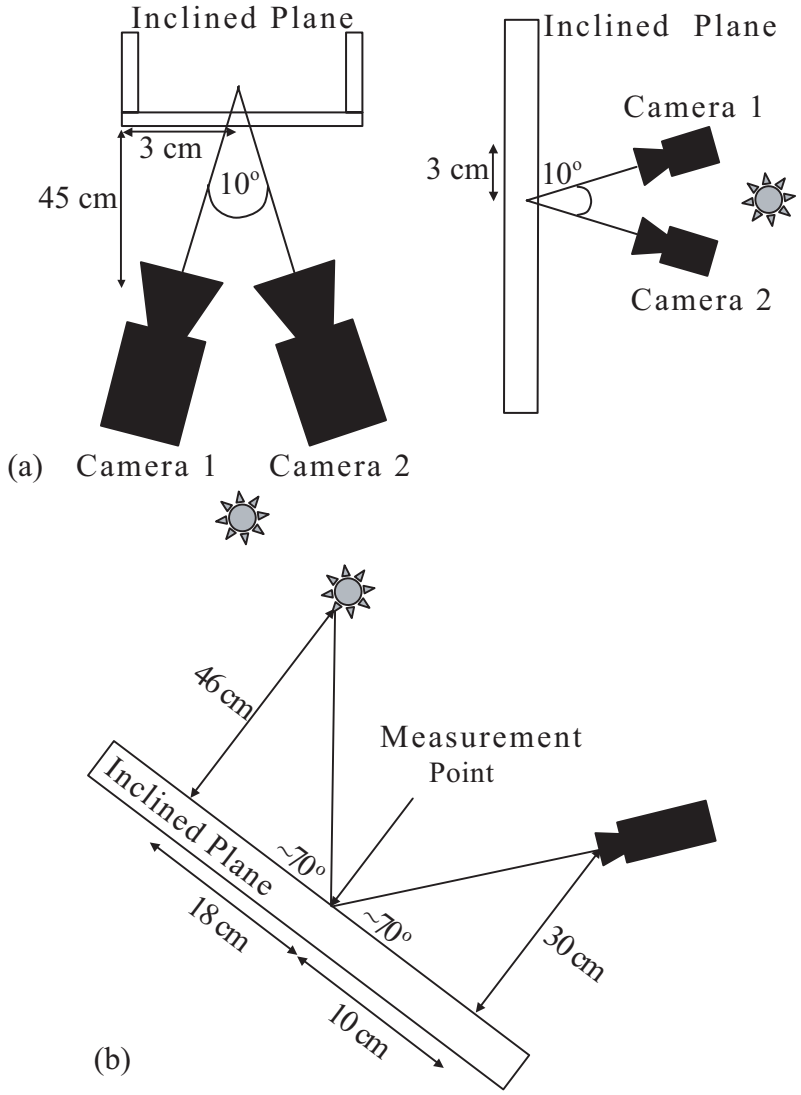

Figure 2.1: Schematic of camera and lighting positions for (a) stereoscopic particle imaging velocimetry, and (b) free surface imaging.

image pairs to obtain a set of particle locations for each imaging instant, followed by application of the last step to all particle position sets which are separated by 0.5, 1.0, 1.5, and 2 seconds in time.

Particle identification

Particles are identified in the images by first using background subtraction to remove gradients in intensity due to the lighting. Thresholding of the intensity produces a "binary" image where particles appear black and the background is white. Each group of black points is analyzed by an automated computational method to determine if they represent a spherical particle — which implies determination of whether they are sufficiently circular in the image. The analysis is based upon constructing ratios of the second, third and fourth moments ($\mu_{2,3,4}$ respectively) of the groups of points [28]

$$\begin{aligned} \mu_2 &= \frac{1}{N}\sum_{i=1}^{N} r_i^2 = \frac{1}{\pi R^2}\int_0^{2\pi}\int_0^R r^3 dr d\Theta = \frac{R^2}{2} \\ \mu_3 &= \frac{1}{N}\sum_{i=1}^{N} r_i^3 = \frac{1}{\pi R^2}\int_0^{2\pi}\int_0^R r^4 dr d\Theta = \frac{2R^3}{5} \\ \mu_4 &= \frac{1}{N}\sum_{i=1}^{N} r_i^4 = \frac{1}{\pi R^2}\int_0^{2\pi}\int_0^R r^5 dr d\Theta = \frac{R^4}{3} \end{aligned} \tag{2.1}$$

where R is the circle radius and the coordinate system is centered at the objects center of mass. The two size independent measures ($m_{1,2}$) used to determine if the object is a circle are constructed as

$$\begin{aligned} m_1 &= \frac{\mu_3}{\mu_2^{3/2}} = \frac{4\sqrt{2}}{5} \\ m_2 &= \frac{\mu_4}{\mu_2^2} = \frac{4}{3} \end{aligned} \tag{2.2}$$

If the m_i (which are radius-independent) differ significantly from the parameters of a true circle, the object is discarded; in practice, the criterion for this decision was made such that if two spherical particles, of the same size as the particles observed in

practice, overlapped by less than fifty percent of their projected area, the combined observed object would not be considered a particle. This translates into a 5% change in m_1 and a 7.5% change in m_2. If either of these criteria is not met then the object is discarded. In this case it is assumed that the object is either not a spherical particle, or that the object is the partially eclipsed image of two spherical particles.

Stereoscopic particle positioning

The stereoscopic PIV method relies on the fact that the position of an object in space can be determined by observing the object from two different camera positions. If, from each camera position, the vector to the object is first determined, the position of the object in three-dimensional space is given by the intersection of these two vectors. To obtain the necessary information, two cameras were located approximately 45 cm from the inclined plane such that the angle of incidence on the plane of their views were separated by approximately 10^o. The distance between the cameras was approximately 6 cm. This setup is illustrated by the schematic in Figure 2.1 (a).

The coordinate system in three dimensions is defined by placing an object referred to here as an "optical standard" into the field of view. The optical standard consists of a precision-machined block of aluminum with original dimension 3.5 cm $\times$ 2.5 cm $\times$ 1.0 cm; one face of this block was further machined to provide five square posts of $400 \pm 2\mu$m in width. One of the five posts is reduced in height by 2.54 mm (0.100 in) from the others, which are not reduced in this dimension from the as-received block. In use, the standard is placed with the four long posts in contact with the solid surface of the inclined plane. An image of the face of the optical standard used can be seen in Figure 2.2. The posts provide three identifiable points which lie in a plane, against the inclined plane (the fourth of these is not needed), and one identifiable point which lies out of this plane. Designating one of the points as the origin, the positions of all of these points in three-space designated by (x, y, z) are defined, and are given in

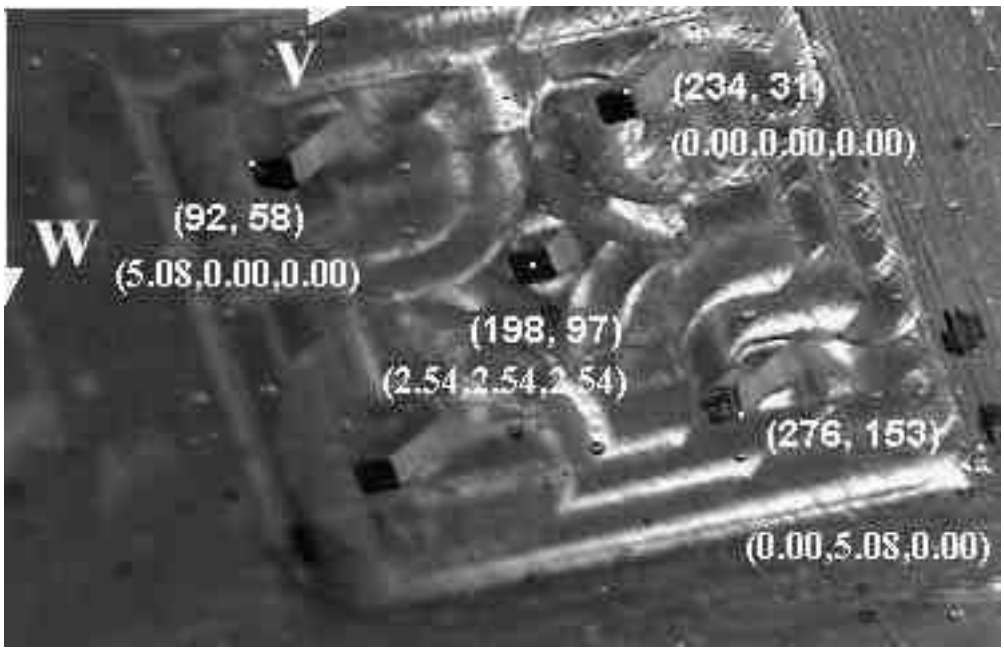

Figure 2.2: Image space positions of critical features labeled in pixels (V, W) (upper text) and three-dimensional physical position referenced to the uppermost identified point in the picture (lower text).

Table 2.1.

An image of the optical standard, as shown in Figure 2.2, provides a two-dimensional pixel location (V, W) of each point in the physical three-space. A knowledge of the actual positions of the points from the optical standard allows us to define a transformation from a point in an image to a position vector in three dimensional physical space, *i.e.* $T : (V, W) \rightarrow (x, y, z)$. The x and y coordinates in physical space are defined by the three points which lie in the plane, and in practice were always oriented such that the positive x coordinate corresponds to the long axis of the channel (the mean flow direction) and the y coordinate corresponds to the spanwise direction. The z coordinate is defined using the out of plane point, and is zero at the solid surface and positive above it. Since the lens system being used consists of a series of thin lenses it can be assumed that all of the vectors going to the camera are parallel, an

Table 2.1: Coordinates of the critical features on the optical standard shown in Figure 2.2.

Real Space Coordinates (mm)	Image Space Coordinates (pixels)
(x , y , z)	(V,W)
(0.00 , 0.00 , 0.00)	(234,31)
(5.08 , 0.00 , 0.00)	(92,58)
(0.00 , 5.08 , 0.00)	(276,153)
(2.54 , 2.54 , 2.54)	(198,97)

assumption verified later for the lens system in use. Because the vectors are assumed to be parallel, we are able to develop a linear transformation between the location at which each vector intersects the $z = 0$ plane in three-space and the two-dimensional coordinate system of the image from the camera [29]. This transformation is of the following form,

$$\mathbf{X} = T \cdot \mathbf{w} + R, \tag{2.3}$$

where $\mathbf{X}$ is a position where this particular vector intersects the $x - y$ plane ($z = 0$), $\mathbf{w}$ is the position of the object in the image space taken by the camera, T is a two by two matrix, and R is a vector of length two. Once the three points in the $x - y$ plane have been located in the coordinate system of the image, the matrix T and the vector R are then determined by solving (2.3), or more explicitly:

$$T = A \cdot B \tag{2.4}$$

$$R = -T \cdot \mathbf{d}_1 - \mathbf{c}_1. \tag{2.5}$$

The various quantities in (2.4) and (2.5) are defined as follows: the columns of A are given by $\mathbf{c}_2 - \mathbf{c}_1$ and $\mathbf{c}_3 - \mathbf{c}_1$ respectively, with $\mathbf{c}_i$ a column vector denoting the location of object i in the physical $x - y$ plane; the columns of B are given by $\mathbf{d}_2 - \mathbf{d}_1$ and $\mathbf{d}_3 - \mathbf{d}_1$ respectively, where $\mathbf{d}_i$ is a column vector denoting the location of object i in

the image (V, W) space, a subscript 1 denotes the object being used as the physical space origin, and subscripts 2 and 3 denote the physical space objects which define the x and y axes in physical space. Table 2.1 gives the image space and corresponding physical space location of the points identified in Figure 2.2. The three points with a z position of 0.00 are used to determine T and R for this camera. The image space coordinate system (V, W) is defined with $(0, 0)$ at the top left corner of the picture and is illustrated in Figure 2.2.

It is necessary to determine the direction which is associated with the vectors from each camera. Under the approximation of parallel vectors from the image to camera, the direction the camera must be from all objects which are observed can be determined from the identifiable point on the optical standard which lies out of the $(x, y, z = 0)$ plane. This is the point located at $(V = 198, W = 97)$ in the example of Figure 2.2. The relation (2.3) is used to determine the point where the vector from the out-of-plane point to the camera intersects the $(x, y, z = 0)$ plane. The direction the camera lies from all viewable objects is defined by the difference between the actual position of the out-of-plane identifiable point of the optical standard and the point determined from (2.3) above, given the (V, W) coordinates of the out-of-plane point.

The vector along which a point on an object lies is defined by the point at which the ray of light intersects the $(x, y, z = 0)$ plane, which is found using (2.3), and the direction associated with the camera, found by the procedure outlined in the previous paragraph. Recall that a vector to a point is determined for each camera, and a line along the vector direction can be defined for each. The three dimensional location of an observed object is the point where the lines associated with that object from the two cameras intersect. In practice, the object position is taken as the point which minimizes the sum of the distances between itself and each vector. This point bisects

the shortest possible line between the two vectors.

The assumption that all vectors from the camera to the measurement volume are parallel to the focal axis is justified experimentally. The optical standard is first used to define the matrix T and the vector R, which are both different for each camera, as well as to define the camera directions. The optical standard was then moved a known distance and the locations of the features were then calculated and compared to their actual positions. When the optical standard was moved 2 mm, with a micrometer driven linear translator, the error in the position of the features was less than 40 μm in each of the three directions.

Velocimetry

Particle velocities are determined by first finding the vector between each particle at time t and each particle at time $t + \Delta t$, $(\Delta \boldsymbol{x})_{ij} = \boldsymbol{x}_j(t + \Delta t) - \boldsymbol{x}_i(t)$ for i and j labeling all particles at t and $t + \Delta t$, respectively. Velocities are determined as $\boldsymbol{v} = (\Delta \boldsymbol{x})_{ij}/\Delta t$. Each velocity is assigned the position at the mid-point between the two particle positions used to create it. The $\boldsymbol{v}$ are then assigned to bins according to their z position (height above the solid surface) and then are further classified into bins according to their magnitude in the x, y, and z directions. We assume that there is no correlation between a given particle at time t and a particle at time $t+\Delta t$ which lies upstream (at smaller x), so that the distribution of negative x-directed velocities represents the expected uncorrelated distribution of velocities associated with unlike particles for a given position box. The number of velocities which lie in each velocity box is totaled and the number found with a negative v_x is subtracted from the number in the box with the corresponding positive v_x of the same magnitude. This process leaves only the correlated velocity information. The raw frequency data for the tracer study at $z = 2.6$ mm can be seen in Figure 2.3 (a) and the correlated data for this same location is shown in Figure 2.3 (b). A best fit Gaussian curve is determined for

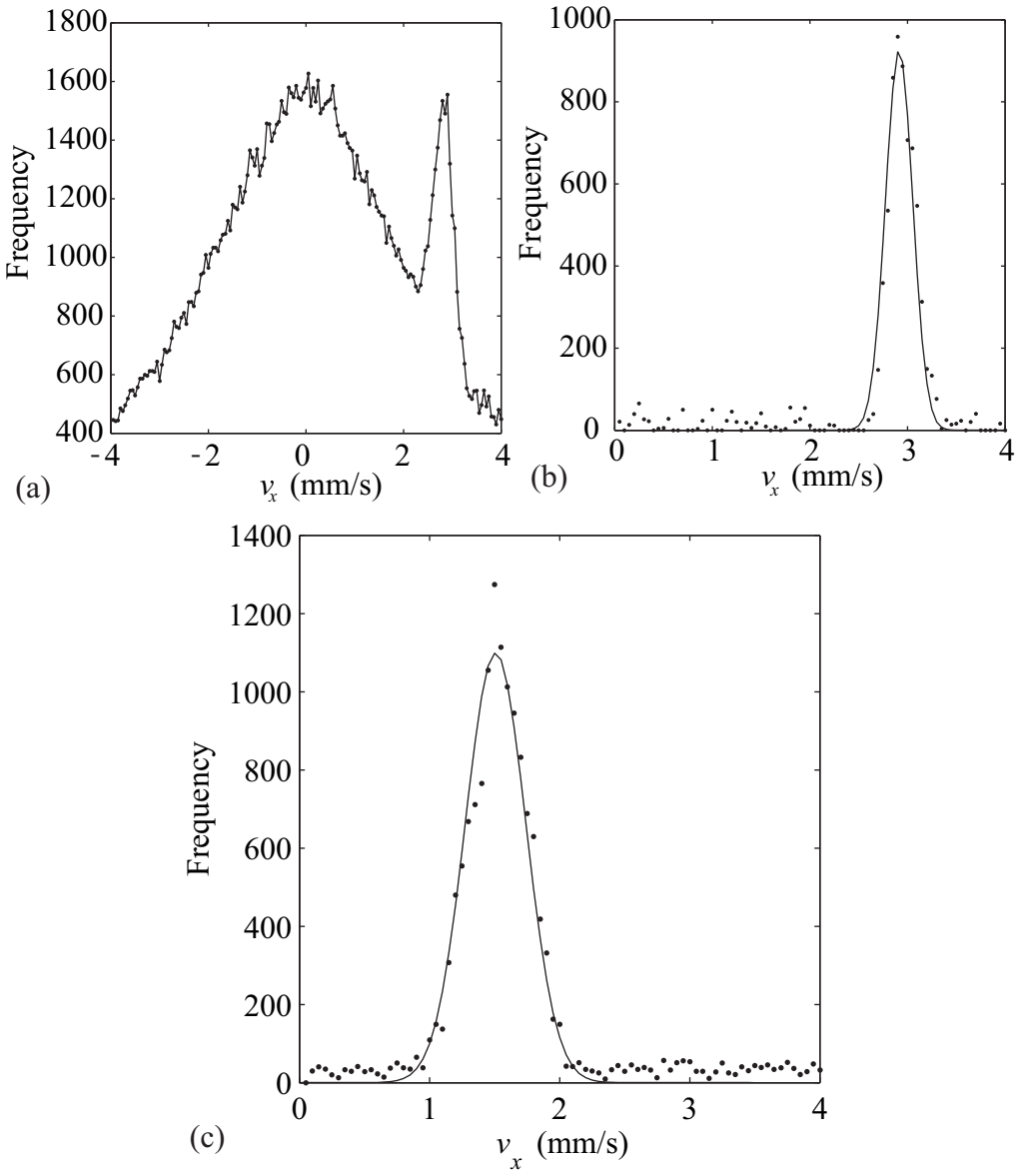

Figure 2.3: Velocimetry data. (a) Raw velocity frequency data for tracer particles ($\phi = 0.005$) for the box centered 2.6 mm above the solid surface of the inclined plane. Gaussian fit of correlated velocity frequency data for (b) tracer particles ($\phi = 0.005$) for the velocity box centered 2.6 mm above the solid surface of the inclined plane and for (c) $\phi = 0.30$, $\alpha = 60.8^o$, $h_o = 2.72$ mm, and $x = 15$ cm for the velocity box centered 1.4 mm above the solid surface of the inclined plane.

the frequency-velocity data for the bin at each distance above the solid surface, as illustrated in Figure 2.3 (b), with the velocity taken as the mean of the Gaussian. The procedure was found to apply well to concentrated suspensions, up to $\phi_B = 0.4$, with qualitatively similar fit to that of the tracer in Figure 2.3 (b) seen in the concentrated suspension data in Figure 2.3 (c).

The particle fraction as a function of height above the solid surface, z, is also of interest. While in principle this quantity is accessible using the image data used for PIV, particle fraction was only reliably determined from the detected particle positions for dilute conditions. Recall that images were taken through the solid surface. Although able to see through the entire film, we found that the probability of detecting a dyed particle near the solid surface differed from the probability closer to the the solid surface. If this probability were equal then the particle fraction as a function of height above the solid surface could be determined by simply counting the number of particles detected at each height above the solid surface. The particle fraction inside a given box is given by

$$\phi(z) = \frac{E(N \mid z)V_P}{L^2 h_b f_d}, \tag{2.6}$$

where $E(N \mid z)$ is the expected number of particles in the box, V_P is the volume of an individual particle, L is the width and length of the box, h_b is the height of the box and f_d is the fraction of particles which are dyed. The results from a tracer study ($\phi = 2 * 10^{-4}$), shown in Figure 2.4 (a), along with the results from an experiment done with $\phi = 0.3$, shown in Figure 2.4 (b), indicate a detection bias depending on the distance of the particle from the lower boundary of the film. The $\phi = 0.3$ concentration profile is inconsistent with the velocity data taken for those experiments. The shear rates found from the velocity profile does not agree with the effective viscosities implied by the particle concentrations found. The apparent

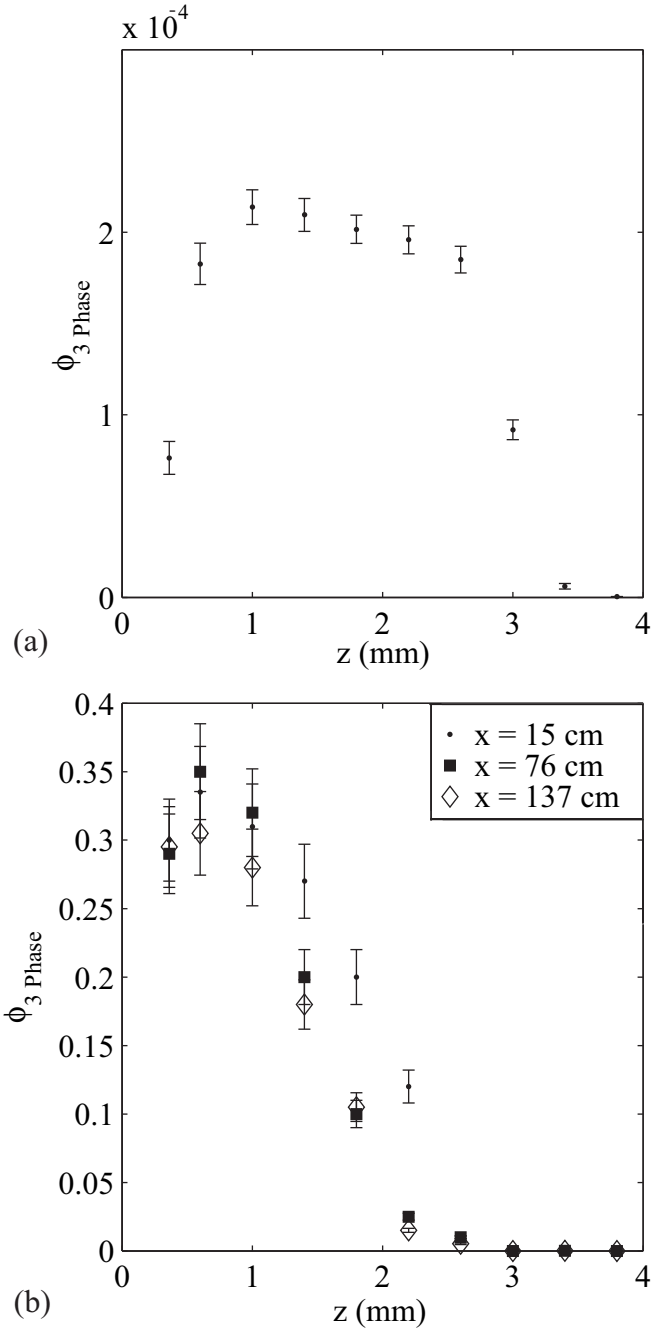

Figure 2.4: Concentration profiles from direct counting of particles in a (a) tracer experiment ($\phi_B = 2 \cdot 10^{-4}$) and (b) $\phi_B = 0.30$. Here ϕ_{3Phase} represents the particle fraction in the full system which consists of liquid, gas, and particles. This arises because of the unknown instantaneous location of the free surface.

reason for this is that the velocity data is not subject to the same detection bias as the concentration: the velocity measurement does not require that there be the same probability of detecting a particle which is present between different heights. It is possible that the failure of the method for determining the detailed particle fraction is due to insufficient index matching of the particles to the fluid.

Rather than using direct particle position sampling to retrieve information about the particle concentration, we treat the flow as inclined plane flow of two layers with different Newtonian viscosities. The choice of only two layers is described below. This two-layer model yields a three parameter model of the velocity,

$$\begin{aligned} v(z) &= \frac{h^2 \rho g \cdot sin(\alpha)}{2} \left[\frac{1-(\Delta)^2}{\eta_{S_1}} + \frac{(\Delta)^2 - (\frac{h-z}{h})^2}{\eta_{S_2}} \right] \quad for z \in [(1-\Delta)\cdot h,\ h] \\ v(z) &= \frac{h^2 \rho g \cdot sin(\alpha)}{2} \left[\frac{1-(\frac{h-z}{h})^2}{\eta_{S_1}} \right] \qquad\qquad for z \in [0,\ (1-\Delta)\cdot h) \end{aligned} \tag{2.7}$$

where the velocity is specified by choosing the viscosities (η_{S_i}) of the fluid layers as well as the location of the boundary between the two distinct layers (Δ). The variable Δ is confined to the interval between 0 and 1, and represents the fraction of the film at the measurement position made up of the layer next to the free surface (which has viscosity η_{S_2}). The model fit to measured velocity data is made by minimizing the squared error between the model velocity and the actual velocity data using a Nelder-Mead simplex [30]. A typical two layer Newtonian viscosity fit is shown in Figure 2.5.

From the implied viscosity and the relationship between particle fraction and effective viscosity, $\eta_s(\phi)$, we determine the implied particle fraction. The pure fluid viscosity is determined for each experiment by fitting a one viscosity model to the velocity profile taken nearest the start of the channel and by making the assumption that the particle concentration is uniform at the bulk concentration across the film. The assumptions are apparently justified: Table 2.2 shows that the viscosities from the

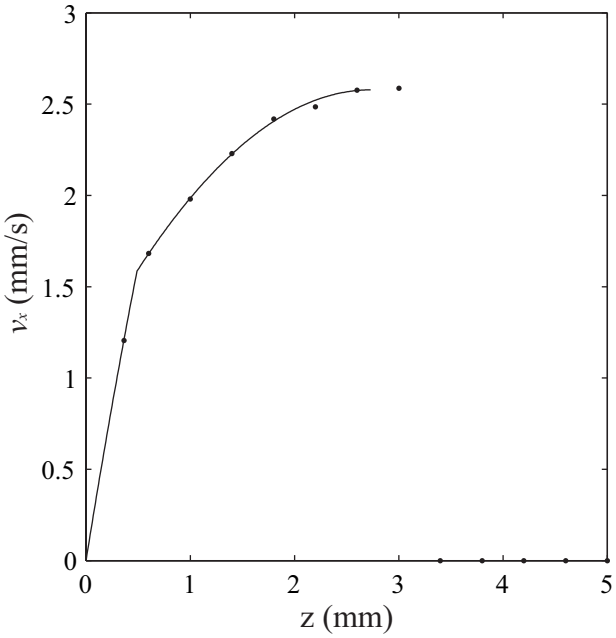

Figure 2.5: PIV velocities and two layer Newtonian viscosity model fit for $\phi = 0.30$, $\alpha = 60.8^o$, $h_o = 3.21$ mm , and $x = 137$ cm. The model parameters are $\eta_{S_1} = 7.81$ Pa s, $\eta_{S_2} = 25.84$ Pa s, and $\Delta = 0.82$.

two viscosity fit for the pure fluid (experiment 1) are almost identical to those of the one viscosity fit, while the two viscosities for the suspension at the earliest measuring location, $x = 15$ cm, were found to be relatively close in value, varying from 7.99 Pa s to 8.10 Pa s. The pure fluid viscosity is determined in this manner because of its sensitivity to temperature, which was not well controlled in the laboratory and varied from one experiment to another. In light of this lack of migration 15 cm from onset of flow the thickness at $x = 15$ cm is treated as the initial thickness of the film, h_o.

Although it is tempting to represent the flow as more than two Newtonian fluids, there is insufficient velocity data to warrant this. Typically, our velocity profiles are made up of 5 to 6 data points, and a three viscosity model requires 5 model parameters. A fit with 5 parameters with only 5 data points introduces a significant amount of noise into the results, where small changes in the measured data produce large changes in the predicted values; by using more data than there are parameters in the model, averaging takes place which makes the output much less sensitive to small changes in the input data. In light of this lack of velocity data the most we can hope to get from a model of this type is 2 viscosities, and the location where the effective viscosity changes from one to the other.

2.2.3 Free surface characterization

In order to characterize the corrugations in the free surface of inclined plane flow, a series of images is taken of the reflection of light from of the free surface. A camera is placed above the free surface such that its focal axis creates an angle of approximately 70^o from the film (or 20^o from the mean surface normal), as shown in Figure 2.1 (b). Light is provided by a 300 W Philips white light bulb without diffuser (providing an approximate point source of light), placed such that the light reflected from the mean flat surface reaches the center of the frame of the camera. If the surface is deformed

such that the surface normal vector is in a direction different from the mean normal vector, light is reflected away from the camera producing a dark region in the image.

The series of intensity images were subjected to Fourier analysis to obtain length scale information about the free surface. Both one- and two-dimensional transforms were considered, and the power spectral density (PSD) determined for each.

One dimensional PSDs were constructed in both the flow and spanwise directions. The one dimensional PSD is obtained by first dividing each image into individual data sets. Each row of pixels in each image was treated as an individual data set for determining the mean PSD in the spanwise direction and each column of pixels is treated as an individual data set for determining the mean PSD in the flow direction.

The first step in determining the PSD of an individual data set is to take the Fast Fourier Transform (FFT)

$$M(k) = fft(X(k)) = \sum_{j=1}^{N} X(j)\omega_N^{(j-1)(k-1)} \tag{2.8}$$

$$\omega_N = exp(-2\pi i/N) \tag{2.9}$$

where M is a vector of the Fourier coefficients, X is a vector of the data minus the mean of the data, i is the unit imaginary number, and N is the number of data points. The power contained within each wavenumber band for the specific data set is then determined from these Fourier coefficients. The power of a given wavenumber is defined as the Fourier coefficient associated with the wavenumber times its complex conjugate, normalized by the largest power for that specific data set

$$P(k) = \frac{M(k) \cdot M(k)^*}{max_{b=1}^{N}\{M(b) \cdot M(b)^*\}} \tag{2.10}$$

where P is the power of the given data set. The mean power spectral density in the spanwise direction is simply the mean of all spanwise power spectral densities of all

data sets in the series

$$\overline{P}(k) = \frac{1}{S}\sum_{b=1}^{S} P(k)_b \tag{2.11}$$

where $\overline{P}$ is the mean power spectral density, and S is the number of data sets in all pictures. The variable S can be thought of as the number of separate data sets in the series. This same process is used to determine the mean PSD in the flow direction. This method is similar to one of the methods used in Loimer *et al.* [15], although we have used the full field of the image rather than a narrow band from the image.

A two dimensional Fourier analysis was used to extract the PSD for frequencies coupled in the flow and spanwise directions as well as uncoupled frequencies from the image intensity. The first step in this process is to take the two dimensional FFT of the raw image after subtracting the mean intensity:

$$M(j,k) = fft(fft(X(j,k))). \tag{2.12}$$

The one-dimensional FFT is first taken of all of the columns of an image, then the FFT is taken of the rows of the Fourier coefficients from this first transform. A two dimensional PSD is constructed for each image in the series and then normalized by the largest power:

$$P(j,k) = \frac{M(j,k)\cdot M(j,k)^*}{max_{b=1,c=1}^{N_1,N_2}\{M(b,c)\cdot M(b,c)^*\}}, \tag{2.13}$$

where N_1 is the number of pixel rows and N_2 is the number of pixel columns. The reported result for a given experiment is the mean of the two dimensional PSDs over the S individual images,

$$\overline{P}(j,k) = \frac{1}{S}\sum_{b=1}^{S} P(j,k)_b. \tag{2.14}$$

Here S represents the number of individual images in the series.

2.3 Results

The goals of this work were to determine the flow of a noncolloidal suspension in free-surface film flow in Stokes flow (vanishing inertia), and to determine the form of the free surface under such flow conditions. Neglect of inertia is well justified, as the particle Reynolds number is very small,

$$Re_p = \frac{\rho\dot{\gamma}(2a)^2}{\eta} = \frac{32\rho a^3}{3\eta h^2}u_{max} < 5 \cdot 10^{-6}$$

for all experiments in this study, where a is the particle radius, u_{max} is the maximum observed velocity, η is the pure fluid viscosity, and h is the film thickness. The film Reynolds number is also small, satisfying

$$Re_f = \frac{\rho^2 g_x h_o^3}{\eta_{S_o}^2} < 0.035$$

for all experiments presented here, where η_{S_o} is the effective viscosity of a suspension with a particle concentration equal to the bulk particle concentration.

As in prior experimental examinations of suspension flows with varying shear [4, 5] and predicted by theoretical treatments of these flows [6, 7, 1], we observe the migration of particles away from regions of high shear towards regions of low shear, although we are not able to make precise statements about the migration near the free surface. We have also observed the deformation of a free surface presumably caused by particle interactions in the bulk (subsurface) flow which has been previously observed by Loimer *et al.* [15]. Note that the surfaces in the work of Loimer *et al.* had normal along the vorticity direction of a band-driven simple shear flow, and thus were not stress-free as the surfaces here are, and it is thus interesting to note the relative similarity of the observations.

2.3.1 Particle imaging velocimetry

Experiments from this study have shown that particle migration in thin films occurs under a range of conditions, characterized in dimensionless form by the particle-scale capillary number, Ca_p, $h_o/(2a)$, and ϕ_B. Velocity profiles for all experiments show a decrease in effective viscosity of the material nearest the wall as the suspension moves down the inclined plane, implying a reduction in ϕ here. The influence of migration upon the film velocity leads also to a decrease in film thickness.

The depth, or z, coordinate has been scaled with h_o, taken as the film depth $x = 15$ cm, slightly downstream of the point suspension is placed on the inclined plane. All velocities reported here have been scaled by U_o, which is chosen such that the scaled total flux is equal to the total flux of a pure fluid scaled by the velocity at the free surface. Pure Newtonian fluid inclined plane flow, with maximum scaled velocity of 1, has a flux of 2/3. Figure 2.6 (b – d) shows that the fully developed velocity profile scales with α and h_o^2. It is unclear, from the limited results presented here, how ϕ_{bulk} affects the scaled fully developed velocity profile.

The velocity profile evolution from the velocity profile of a Newtonian fluid with the effective viscosity of the bulk particle concentration to the fully developed velocity profile is shown in Figure 2.7. As the fluid moves down the inclined plane the velocity near the wall is observed to increase. Figure 2.7 shows that the distance required to achieve a fully developed state decreases as the bulk particle concentration increases. It is important to note that model predictions from §2.4 suggest that the velocity profile for $\phi = 0.20$ at $x = 137$ mm is not fully developed.

The large velocity gradient near the wall, shown in Figures 2.6 and 2.7, suggests that the particle concentration near the wall has become nearly zero in the fully developed state. This is confirmed by an examination of histograms of counted particles

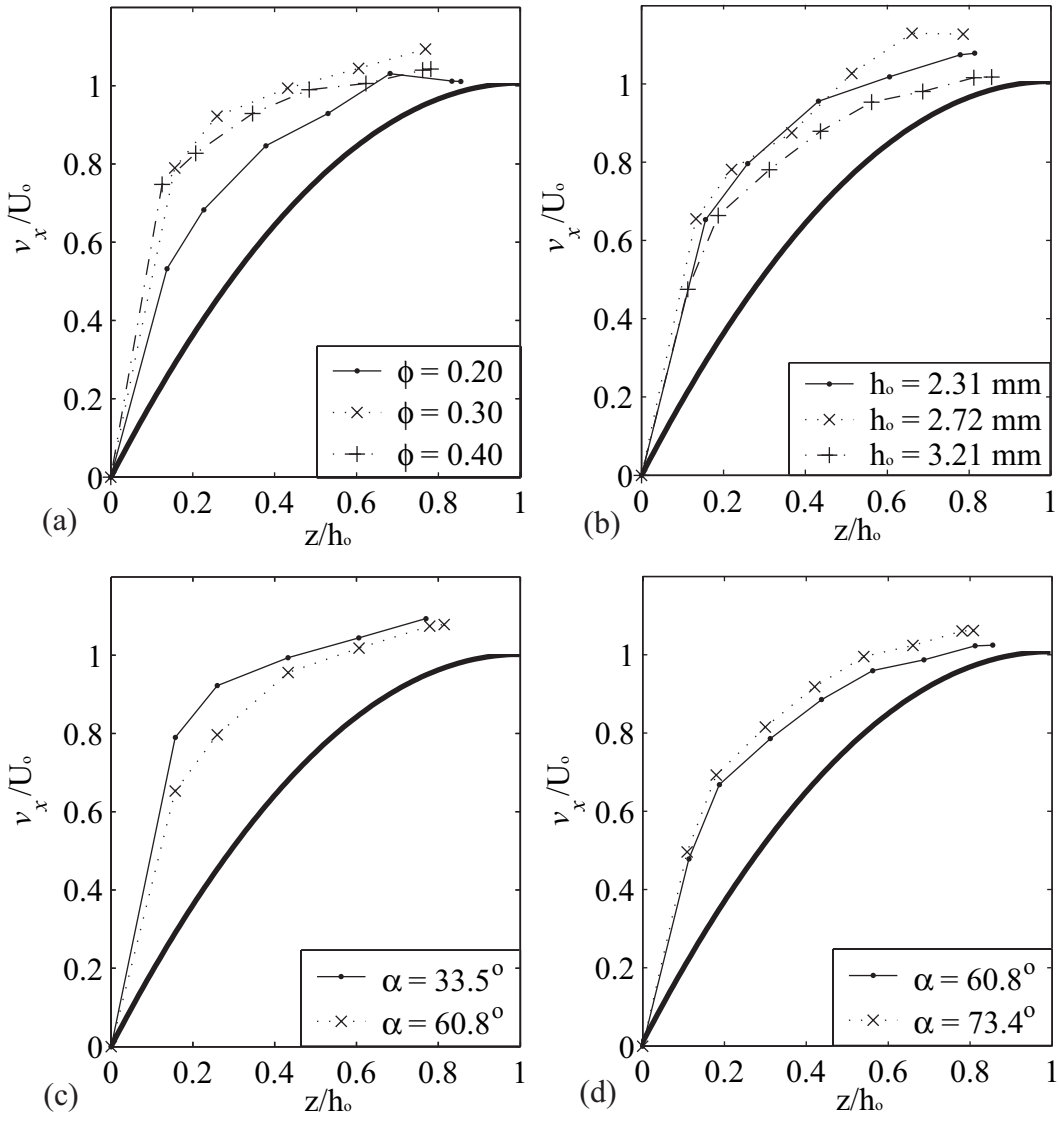

Figure 2.6: Comparison of velocity profiles at $x = 137$ cm for various conditions. (a) Effect of ϕ on final velocity profile for $\alpha = 33.5^o$, and $h_o = 2.64$ mm, $h_o = 2.31$ mm, and $h_o = 2.89$ mm respectively. (b) Effect of h_o on final velocity profile for $\phi = 0.30$, and $\alpha = 60.8^o$. Effect of α on final velocity profile for $\phi = 0.30$, and (c) $h_o = 2.3$ mm (d) $h_o \approx 3.3$ mm. The heavy line in (a–d) represents the parabolic, pure Newtonian fluid profile of the same flux.

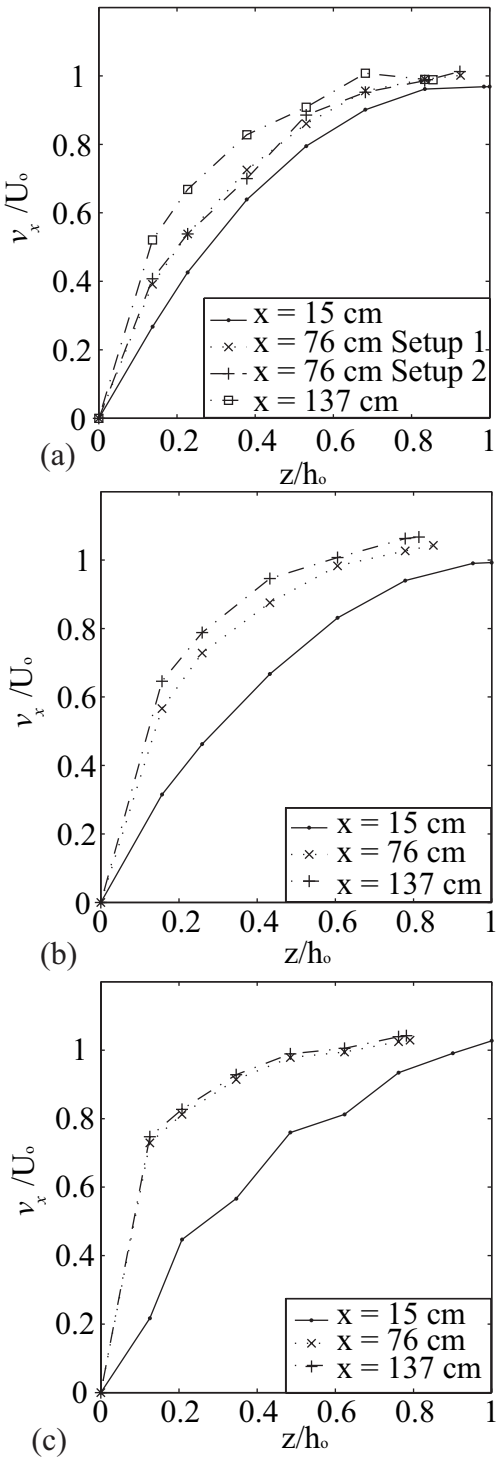

Figure 2.7: Axial evolution of dimensionless velocity profile. (a) $\phi_{\text{bulk}} = 0.20$, $\alpha = 33.5^o$, and $h_o = 2.6$ mm; (b) $\phi_{\text{bulk}} = 0.30$, $\alpha = 60.8^o$, and $h_o = 2.3$ mm; and (c) $\phi_{\text{bulk}} = 0.40$, $\alpha = 33.5^o$, and $h_0 = 2.9$ mm.

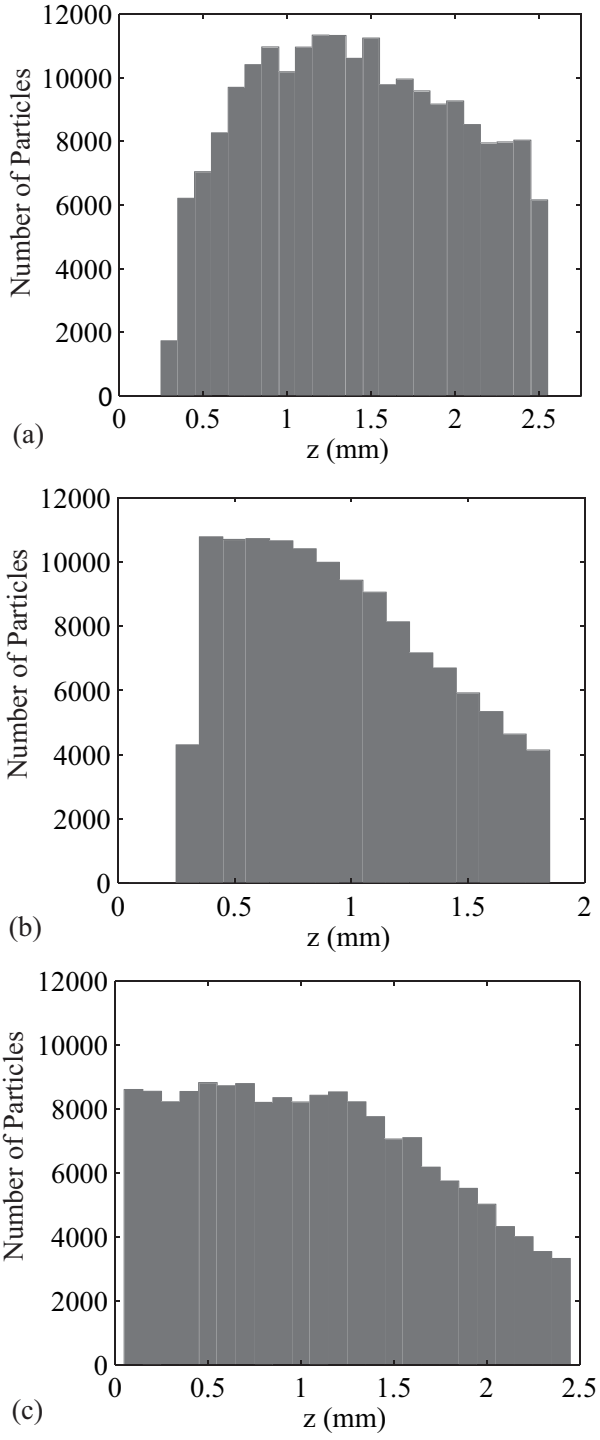

Figure 2.8: Histogram of particle locations for (a) $\phi = 0.30$, $\alpha = 60.8^o$, $h = 2.14$ mm, and $x = 137$ cm (b) $\phi = 0.30$, $\alpha = 33.5^o$, $h = 1.78$ mm, and $x = 137$ cm (c) $\phi = 0.30$, $\alpha = 33.5^o$, $h = 2.31$ mm, and $x = 15$ cm.

Table 2.2: Results from all PIV experiments discussed here, labeled in the leftmost column by experiment number. The variables η_{S_1}, η_{S_2} and Δ are the results from the two layer Newtonian viscosity model, where 1 refers to the region closest to the solid surface and the variable Δ is the fraction of the total film which is made up of the layer next to the free surface. The particle fractions implied by the viscosities found from the two layer Newtonian viscosity model are given as ϕ_1 and ϕ_2. Units of dimensional quantities are indicated in the second line of the top row. The particle diameter range used in these experiments was 250-300 μm.

	ϕ	α	Q	x	h	η_{S_1}	η_{S_2}	Δ	ϕ_1	ϕ_2	η
		deg	mL/min	cm	mm	Pa s	Pa s				Pa s
1	0	33.5	13.390	76	2.68	7.99	8.10	0.88	0.00	0.00	8.1
2	0.2	33.5	13.390	15	2.64	7.70	8.07	0.54	0.19	0.20	3.9
				76	2.44	4.84	8.40	0.83	0.07	0.21	
				76	2.44	4.57	8.15	0.86	0.05	0.20	
				137	2.26	3.34	9.60	0.81	0.00	0.24	
3	0.3	33.5	5.683	15	2.31	12.11	15.60	0.57	0.29	0.33	3.7
				76	1.89	5.07	15.96	0.76	0.09	0.34	
				137	1.78	3.70	19.07	0.78	0.00	0.36	
4	0.3	60.8	5.683	15	2.31	17.97	19.89	0.86	0.29	0.31	5.6
				76	1.97	8.23	20.72	0.79	0.11	0.31	
				137	1.88	6.86	20.84	0.79	0.06	0.31	
5	0.3	60.8	9.520	15	2.72	20.02	17.48	0.63	0.31	0.28	5.6
				76	2.34	8.52	20.50	0.83	0.13	0.31	
				137	2.14	6.22	17.89	0.83	0.04	0.29	
6	0.3	60.8	14.297	15	3.21	21.26	19.36	0.60	0.30	0.29	6.0
				76	2.80	8.50	24.98	0.83	0.10	0.33	
				137	2.74	7.81	25.84	0.82	0.08	0.34	
7	0.3	73.4	17.610	15	3.33	19.47	20.64	0.90	0.29	0.30	5.9
				137	2.69	6.68	21.54	0.82	0.04	0.31	
8	0.4	33.5	2.778	15	2.89	45.46	48.27	0.94	0.40	0.41	6.5
				76	2.28	8.30	73.13	0.90	0.08	0.46	
				137	2.26	7.58	72.23	0.91	0.05	0.46	

(see the method described in §2.2.2). Very few particles were found within 0.3 mm of the solid surface for the fully developed cases shown in Figure 2.8 (a,b), while a similar examination of the initial flow, Figure 2.8 (c), shows that particles are initially present in this region. Reduced particle concentration at the wall is also supported by the fact that all experiments with suspensions of $\phi \geq 0.2$ resulted in a film thickness which decreased as the mixture flowed down the inclined plane. The film thickness in inclined plane flow is quite sensitive to changes in viscosity near the solid wall.

Results for all experiments for which film thickness are available, are presented in Table 2.2. All experiments of concentrated suspensions resulted in downstream velocity profiles which exhibited an increase in the velocity gradient near the wall. Implied viscosities determined from a two-layer Newtonian viscosity model and implied particle fractions are presented. Implied particle fractions were determined by solving the following relation,

$$\eta_S = \eta \left(1 - \frac{\phi}{\phi_{max}}\right)^{-2}$$

where η_S is the viscosity found from the two layer Newtonian viscosity model, η is the pure fluid viscosity, and $\phi_{max} = 0.65$. Particle flux matching to the experimental value was within 15%.

It is not possible to determine the particle concentration at the free surface precisely from our data. With a two-layer model for the velocity, decreases in viscosity at the solid surface are more likely to be detected than decreases at the free surface since they will result in a greater change in the velocity. Changes in the effective viscosity at the free surface will result in a very small change in the velocity and therefore are difficult to infer from the measured velocity profile.

Experiments were also done for $\phi = 0.30$, and $\alpha = 90^o$. There was a smooth transition from a flat film, evenly spread across the width of the channel to a film

where all of the fluid was flowing down the corners between the bottom of the channel and the side walls with almost no suspension in the center of the channel. This result was repeatable and stable to forced disturbances of the free surface. The film was not sufficiently uniform to warrant PIV measurements.

The film thicknesses reported in this study were determined by integrating the particle velocity to find the point where the total material flux was equal to the total flux which was physically set in the experiment. There was close agreement between this thickness and the film thickness determined by depth micrometer. We are unable to determine the thickness of the film for the $\phi = 0.30$, $\alpha = 90^o$ experiment, since our method requires the assumption of no variations in the thickness in the spanwise direction.

The reproducibility of the stereoscopic PIV technique employed in this study is demonstrated in Figure 2.7. Two independent camera setups, with images taken over two different time periods, were used during the course of a single experiment to measure the velocity profile at $x = 76$ cm. The figure illustrates close agreement between the measured velocity profiles. The largest velocity difference in the results from the two trials was 3% of the maximum velocity 2.85 mm/s, or about 0.08 mm/s. This reproducibility indicates the significance of the difference in the velocity profiles, resulting apparently from particle migration, measured at $x = 15$ cm and $x = 137$ cm from these results.

2.3.2 Surface imaging

The surface deformation, resulting from particle interactions in the bulk, has been characterized by the method described in §2.2.3. This deformation reflects a balance between surface tension and viscous forces, commonly given by a capillary number. Two capillary numbers were considered in this study. The first was based on the

stress averaged over the film thickness,

$$Ca_f = \frac{\rho g_x h a}{\sigma}$$

and the second based on the mean stress within a particle diameter of the free surface

$$Ca_p = \frac{2\rho g_x a^2}{\sigma},$$

where σ is the measured surface tension. The former definition was used, using radius instead of diameter, to characterize their numerical evaluation of film flows containing particles and immiscible liquid drops by Li and Pozrikidis [12, 13] under fairly dilute conditions. Interestingly, at concentrated conditions, comparison of surface images indicate that Ca_p provides a better delineation of behavior than does Ca_f. Experiments conducted at the same Ca_f but of different particle size display different surface topography, as shown in Figure 2.9. There is a discernible change in surface topography for a particle fraction of 0.30 at a Ca_p of $1 \cdot 10^{-4}$. Surfaces with a Ca_p above $1 \cdot 10^{-4}$ are deformed by subsurface particles while surfaces with Ca_p below $1 \cdot 10^{-4}$ are not noticeably deformed.

The relevance of the stress at particle-scale distances from the surface, which is captured by Ca_p, rather than the stress proportional to film depth captured by Ca_f, is also supported by PSD results. Experiments run under constant particle fraction and incline angle at varying h_o have PSDs of very similar wavenumber content. This can be seen in both the two and one dimensional power spectral densities shown in Figures 2.10 and 2.11 respectively. Surface deformation is not seen at a larger Ca_f for the small particles, which implies that the particle scale must be considered in setting the stress in C_a. This is clear from the visual similarity of free surfaces at different h, as well as from the similarity seen in the one and two dimensional power spectral densities.

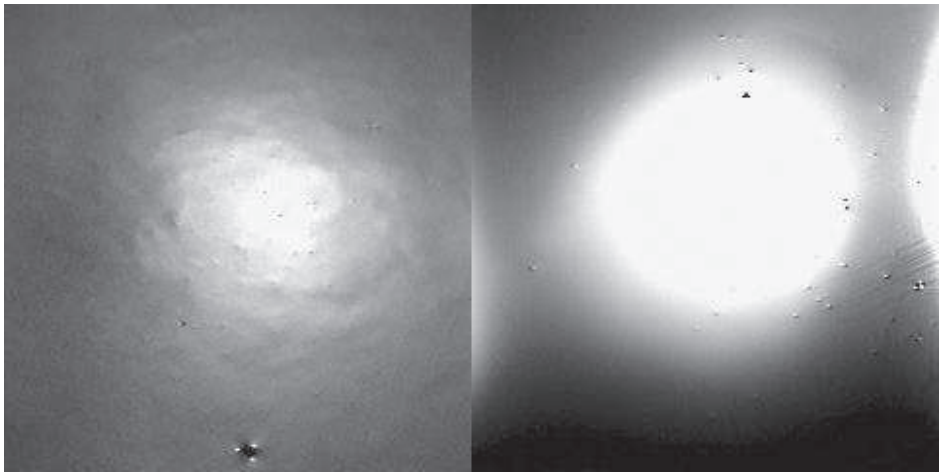

(a) (b)

Figure 2.9: Comparison of initial surface topography with each Ca. (a) $2\bar{a} = 178$ μm, $Ca_f = 2.56 \cdot 10^{-3}$, $Ca_p = 2.19 \cdot 10^{-4}$ (b) $2\bar{a} = 9.9$ μm, $Ca_f = 4.02 \cdot 10^{-3}$, $Ca_p = 1.65 \cdot 10^{-5}$. Images are 2.4 cm wide and 3.0 cm tall, where an individual pixel is 100 μm wide and 125 μm tall. The suspension is flowing from the top of the images towards the bottom.

One dimensional power spectral densities are presented here for limited cases, as they directly compare with the results presented by Loimer *et al.* [15]. For a given wavenumber in the flow direction (k_x), where $k_x = 2\pi/\lambda_x$ with λ_x taken as the wavelength in the x direction, the power in a one dimensional PSD is a function of the two dimensional fast Fourier transform coefficients. There have been limited cases where the one and two dimensional power spectral densities appear to exhibit contradicting behaviors, for reasons not completely understood. We believe that the trends shown by the two dimensional PSDs are valid.

It is clear that the surface topography becomes more deformed as the angle of inclination is increased, as seen in Figure 2.12. As incline angle increases the high wavenumber content of the surface also increases relative to all other wavenumber content, as seen in the two dimensional PSDs in Figure 2.13 and the one dimensional power spectral density in Figure 2.14.

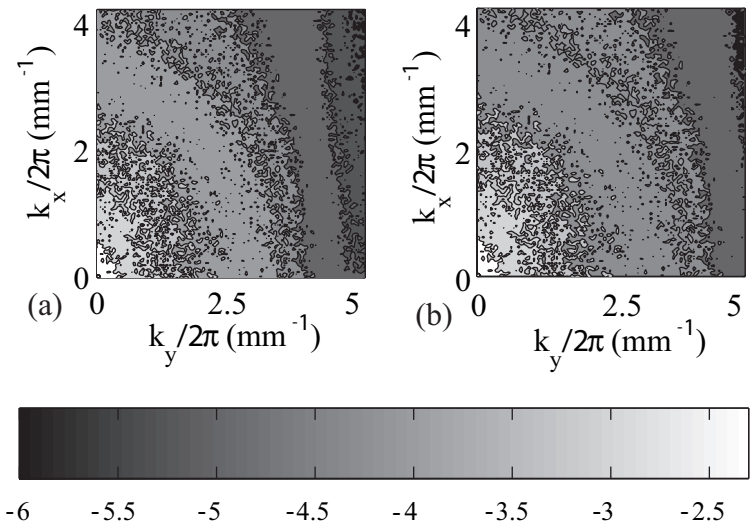

Figure 2.10: Effect of changing initial film thickness, h_o, on the two dimensional power spectral densities of initial surfaces for $2\bar{a} = 178$ μm, $\phi = 0.30$, and $\alpha = 34.6^o$. (a) $h_o = 2.1$ mm (b) $h_o = 3.9$ mm. The values plotted are $\log_{10}$ of the power. A mapping from grey scale color to $\log_{10}$ of the power is shown in the color bar above.

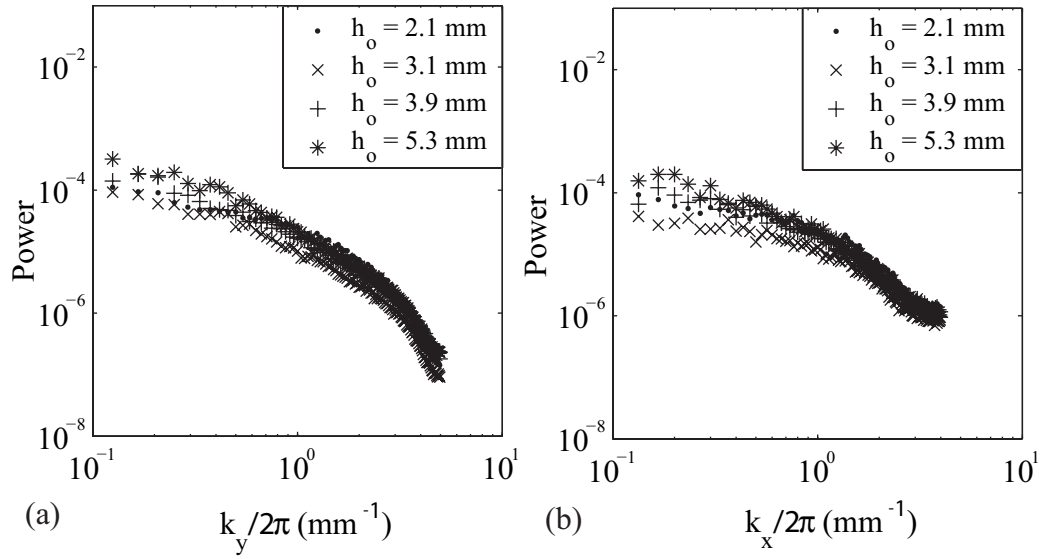

Figure 2.11: Effect of changing h_o on the one dimensional power spectral densities of initial surfaces for $2\bar{a} = 178$ μm, $\phi = 0.30$, and $\alpha = 34.6^o$, in (a) spanwise direction and (b) streamwise direction.

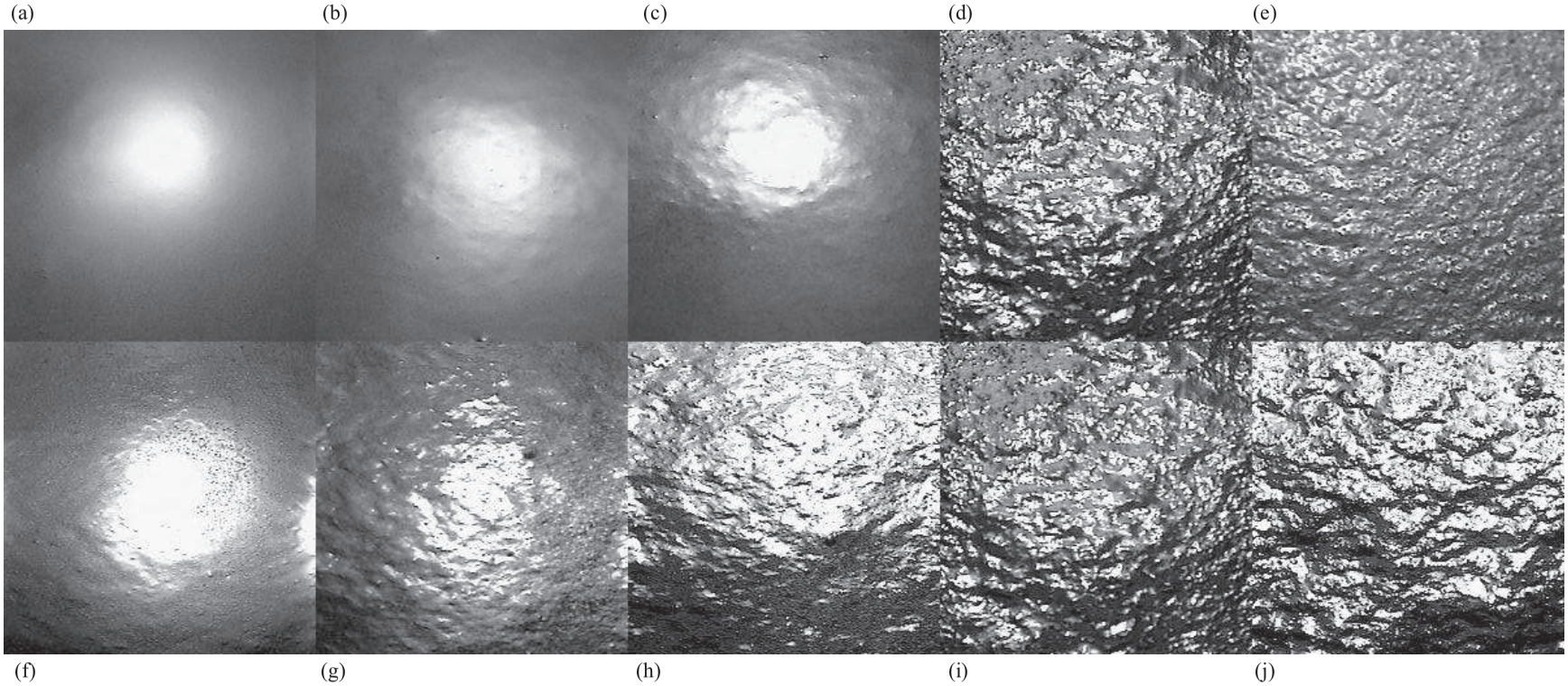

Figure 2.12: Initial surface images. Upper row, varying α with $2\bar{a} = 178$ μm, $\phi = 0.30$ and $h \approx 2$ mm. (a) $\alpha = 0.16^o$, (b) $\alpha = 2.86^o$ (c), $\alpha = 7.30^o$ (d), $\alpha = 34.6^o$, and (e) $\alpha = 60.8^o$. Lower row, varying ϕ with $2\bar{a} = 178$ μm, $\alpha = 34.6^o$ and $h \approx 2.0$ mm. (f) $\phi = 0.01$, (g) $\phi = 0.10$, (h) $\phi = 0.20$, (i) $\phi = 0.30$, and (j) $\phi = 0.40$. Images are 2.4 cm wide and 3.0 cm tall, where an individual pixel is 100 μm wide and 125 μm tall. The suspension is flowing from the top of the images towards the bottom.

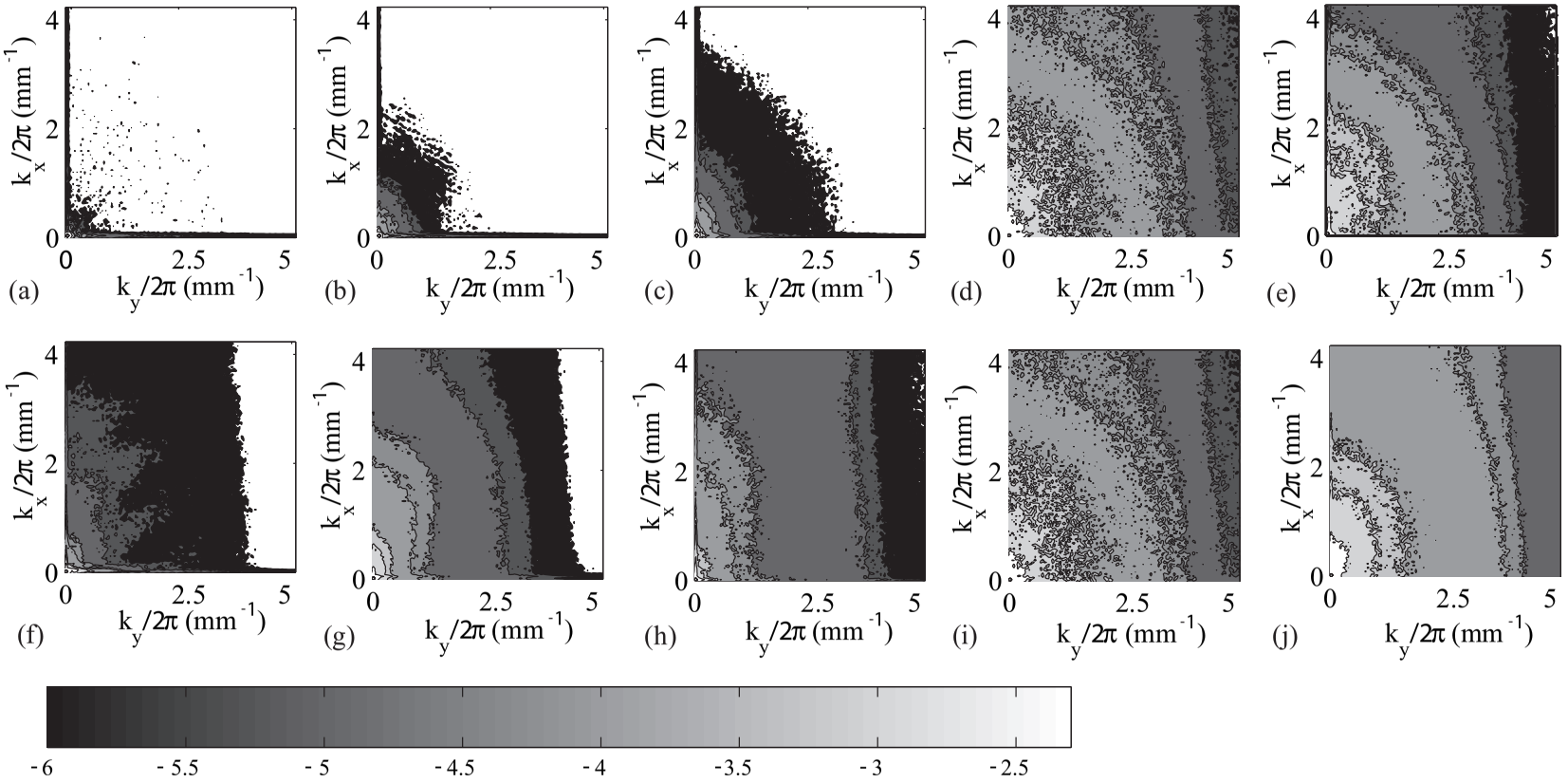

Figure 2.13: Two dimensional power spectral density for conditions corresponding to Figure 2.12. Upper row, varying α, with $2\bar{a} = 178$ μm, $\phi = 0.30$ and $h_o \approx 2$ mm. (a) $\alpha = 0.16^o$ (b) $\alpha = 2.86^o$ (c) $\alpha = 7.30^o$ (d) $\alpha = 34.6^o$ (e) $\alpha = 60.8^o$. Lower row, varying ϕ with $2\bar{a} = 178$ μm, $\alpha = 34.6^o$ and $h_o \approx 2.0mm$. (f) $\phi = 0.01$, (g) $\phi = 0.10$, (h) $\phi = 0.20$, (i) $\phi = 0.30$, and (j) $\phi = 0.40$. The values plotted are $\log_{10}$ of the power. A mapping from grey scale color to $\log_{10}$ of the power is shown in the color bar. The large regions of white space in the high wavenumber region represent powers which are smaller than 10^{-6}.

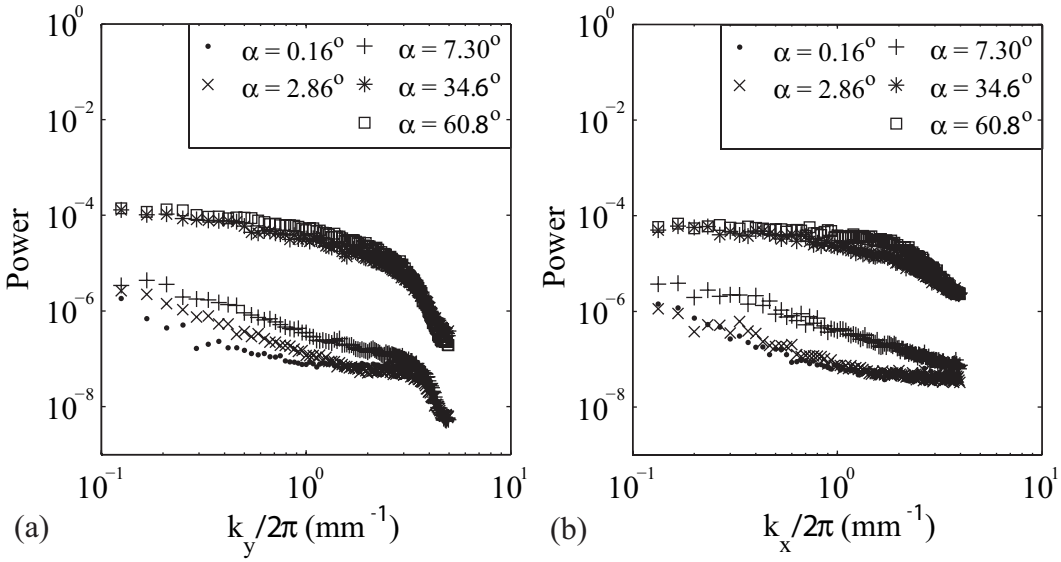

Figure 2.14: One dimensional power spectral density for initial α experiments with $2\bar{a} = 178$ μm, $\phi = 0.30$, and $h_o \approx 2$ mm in (a) spanwise direction, and (b) downstream direction.

The effect of the particle concentration on the surface topography can be seen in Figure 2.12. As the particle fraction increases the surface becomes more deformed, and the relative high wavenumber content of the surface increases as shown in Figure 2.13.

Low pass and band pass filters have also been applied to the images in an attempt to determine if structures on all scales move down stream. Low pass filtering was done with cutoff wavenumbers (wavelength) of 1.2 mm^{-1} ($\lambda = 5.3$ mm), 2.6 mm^{-1} ($\lambda = 2.4$ mm), 4.2 mm^{-1} ($\lambda = 1.5$ mm), 12.6 mm^{-1} ($\lambda = 0.5$ mm), and 20.9 mm^{-1} ($\lambda = 0.3$ mm), where all wavenumbers which were larger than these were discarded. Examples of these filtered images can be seen in Figure 2.16. When the filtered images are viewed one after another as a time series it is possible to see structures associated with all wavenumbers move down stream. Structures associated with all wavenumbers move down stream for all band pass filtered image series as well. Band

pass filtering was done with wavenumber ranges of 2.6 – 5.7 mm^{-1} (λ = 2.4 – 1.1 mm), 5.7 – 12.6 mm^{-1} (λ = 1.1 – 0.5 mm), and 12.6 – 20.9 mm^{-1} (λ = 0.5 – 0.3 mm).

Table 2.3: Ca_p and Ca_f for all initial free surface experiments.

	ϕ	α deg	$2\overline{a}$ μm	h mm	Ca_p	$h/(2\overline{a})$	Ca_f	Surface Description
1	0.30	34.5	9.9	2.413	$1.0 \cdot 10^{-5}$	243.7	$2.4 \cdot 10^{-3}$	smooth
2	0.30	34.5	9.9	3.073	$1.0 \cdot 10^{-5}$	310.4	$3.0 \cdot 10^{-3}$	smooth
3	0.30	0.16	178	1.854	$1.2 \cdot 10^{-5}$	11.7	$1.4 \cdot 10^{-4}$	smooth
4	0.30	75.6	9.9	2.413	$1.6 \cdot 10^{-5}$	243.7	$4.0 \cdot 10^{-3}$	smooth
5	0.30	0.48	178	1.854	$3.7 \cdot 10^{-5}$	11.7	$4.3 \cdot 10^{-4}$	smooth
6	0.30	0.97	178	1.854	$7.4 \cdot 10^{-5}$	11.7	$8.7 \cdot 10^{-4}$	smooth
7	0.30	1.94	178	1.854	$1.4 \cdot 10^{-4}$	11.7	$1.7 \cdot 10^{-3}$	deformed
8	0.30	2.86	178	1.854	$2.1 \cdot 10^{-4}$	11.7	$2.6 \cdot 10^{-3}$	deformed
9	0.30	7.30	178	1.854	$5.5 \cdot 10^{-4}$	11.7	$6.5 \cdot 10^{-3}$	deformed
10	0.30	7.30	178	13.37	$5.5 \cdot 10^{-4}$	84.1	$4.7 \cdot 10^{-2}$	deformed
11	0.01	34.6	178	1.981	$2.5 \cdot 10^{-3}$	12.5	$3.1 \cdot 10^{-2}$	deformed
12	0.05	34.6	178	2.108	$2.5 \cdot 10^{-3}$	13.3	$3.3 \cdot 10^{-2}$	deformed
13	0.10	34.6	178	2.032	$2.5 \cdot 10^{-3}$	12.8	$3.2 \cdot 10^{-2}$	deformed
14	0.20	34.5	178	2.337	$2.5 \cdot 10^{-3}$	14.7	$3.7 \cdot 10^{-2}$	deformed
15	0.20	34.5	178	3.200	$2.5 \cdot 10^{-3}$	20.1	$5.0 \cdot 10^{-2}$	deformed
16	0.20	34.5	178	4.039	$2.5 \cdot 10^{-3}$	25.4	$6.3 \cdot 10^{-2}$	deformed
17	0.30	34.5	178	2.134	$2.5 \cdot 10^{-3}$	13.4	$3.3 \cdot 10^{-2}$	deformed
18	0.30	34.6	178	2.210	$2.5 \cdot 10^{-3}$	13.9	$3.5 \cdot 10^{-2}$	deformed
19	0.30	34.5	178	3.099	$2.5 \cdot 10^{-3}$	19.5	$4.9 \cdot 10^{-2}$	deformed
20	0.30	34.5	178	3.912	$2.5 \cdot 10^{-3}$	24.6	$6.1 \cdot 10^{-2}$	deformed
21	0.30	34.5	178	5.334	$2.5 \cdot 10^{-3}$	33.5	$8.4 \cdot 10^{-2}$	deformed

Table 2.3: (continued).

	ϕ	α deg	$2\overline{a}$ μm	h mm	Ca_p	$h/(2\overline{a})$	Ca_f	Surface Description
22	0.40	34.5	178	2.083	$2.5 \cdot 10^{-3}$	13.1	$3.3 \cdot 10^{-2}$	deformed
23	0.40	34.5	178	3.048	$2.5 \cdot 10^{-3}$	19.2	$4.8 \cdot 10^{-2}$	deformed
24	0.40	34.5	178	4.191	$2.5 \cdot 10^{-3}$	26.4	$6.6 \cdot 10^{-2}$	deformed
25	0.20	60.8	178	2.108	$3.8 \cdot 10^{-3}$	13.3	$5.1 \cdot 10^{-2}$	deformed
26	0.20	60.8	178	3.124	$3.8 \cdot 10^{-3}$	19.6	$7.5 \cdot 10^{-2}$	deformed
27	0.20	60.8	178	3.785	$3.8 \cdot 10^{-3}$	23.8	$9.1 \cdot 10^{-2}$	deformed
28	0.30	60.8	178	2.134	$3.8 \cdot 10^{-3}$	13.4	$5.2 \cdot 10^{-2}$	deformed
29	0.30	60.8	178	3.048	$3.8 \cdot 10^{-3}$	19.2	$7.4 \cdot 10^{-2}$	deformed
30	0.30	60.8	178	4.039	$3.8 \cdot 10^{-3}$	25.4	$9.8 \cdot 10^{-2}$	deformed
31	0.30	60.8	178	5.969	$3.8 \cdot 10^{-3}$	37.5	$1.4 \cdot 10^{-1}$	deformed
32	0.40	60.8	178	2.057	$3.8 \cdot 10^{-3}$	12.9	$5.0 \cdot 10^{-2}$	deformed
33	0.40	60.8	178	3.124	$3.8 \cdot 10^{-3}$	19.6	$7.5 \cdot 10^{-2}$	deformed
34	0.40	60.8	178	4.597	$3.8 \cdot 10^{-3}$	28.9	$1.1 \cdot 10^{-1}$	deformed
35	0.20	75.0	178	1.854	$4.2 \cdot 10^{-3}$	11.7	$5.0 \cdot 10^{-2}$	deformed
36	0.20	75.0	178	2.869	$4.2 \cdot 10^{-3}$	18.0	$7.7 \cdot 10^{-2}$	deformed
37	0.20	75.0	178	4.293	$4.2 \cdot 10^{-3}$	27.0	$1.2 \cdot 10^{-1}$	deformed
38	0.40	75.0	178	1.823	$4.2 \cdot 10^{-3}$	11.5	$4.9 \cdot 10^{-2}$	deformed
39	0.40	75.0	178	3.124	$4.2 \cdot 10^{-3}$	19.6	$8.3 \cdot 10^{-2}$	deformed
40	0.40	75.0	178	4.318	$4.2 \cdot 10^{-3}$	27.2	$1.2 \cdot 10^{-1}$	deformed
41	0.40	90.0	178	2.083	$4.4 \cdot 10^{-3}$	13.1	$5.8 \cdot 10^{-2}$	deformed
42	0.40	90.0	178	3.073	$4.4 \cdot 10^{-3}$	19.3	$8.5 \cdot 10^{-2}$	deformed

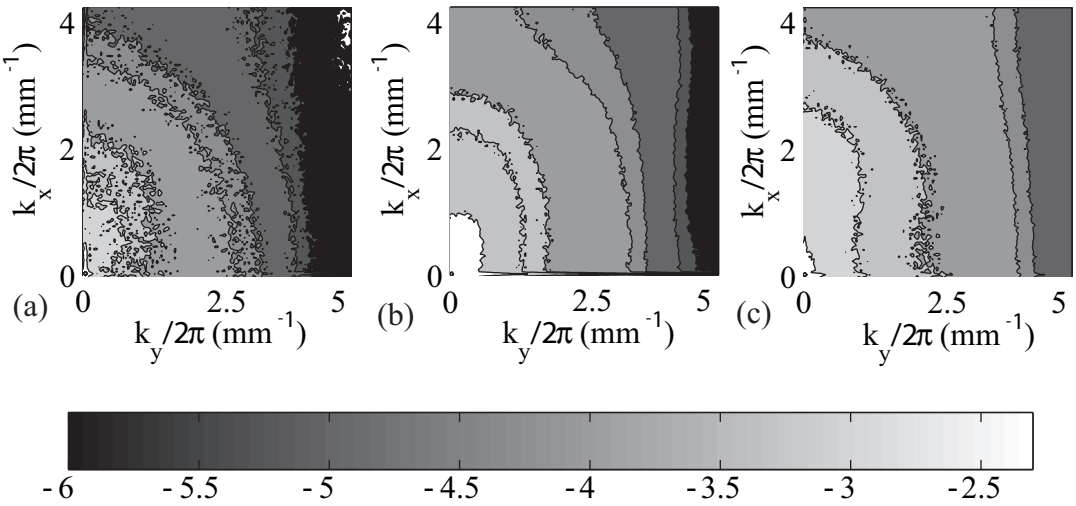

Figure 2.15: Two dimensional power spectral density for different axial locations, with $2\bar{a} = 178$ μm, $\phi = 0.30$, $\alpha = 60.8^o$, and $h_o = 2.1$ mm. (a) Initial surface, $x \to 0$, (b) $x = 76$ cm, and (c) $x = 137$ cm. The values plotted are $\log_{10}$ of the power. A mapping from grey scale color to $\log_{10}$ of the power is shown in the color bar above.

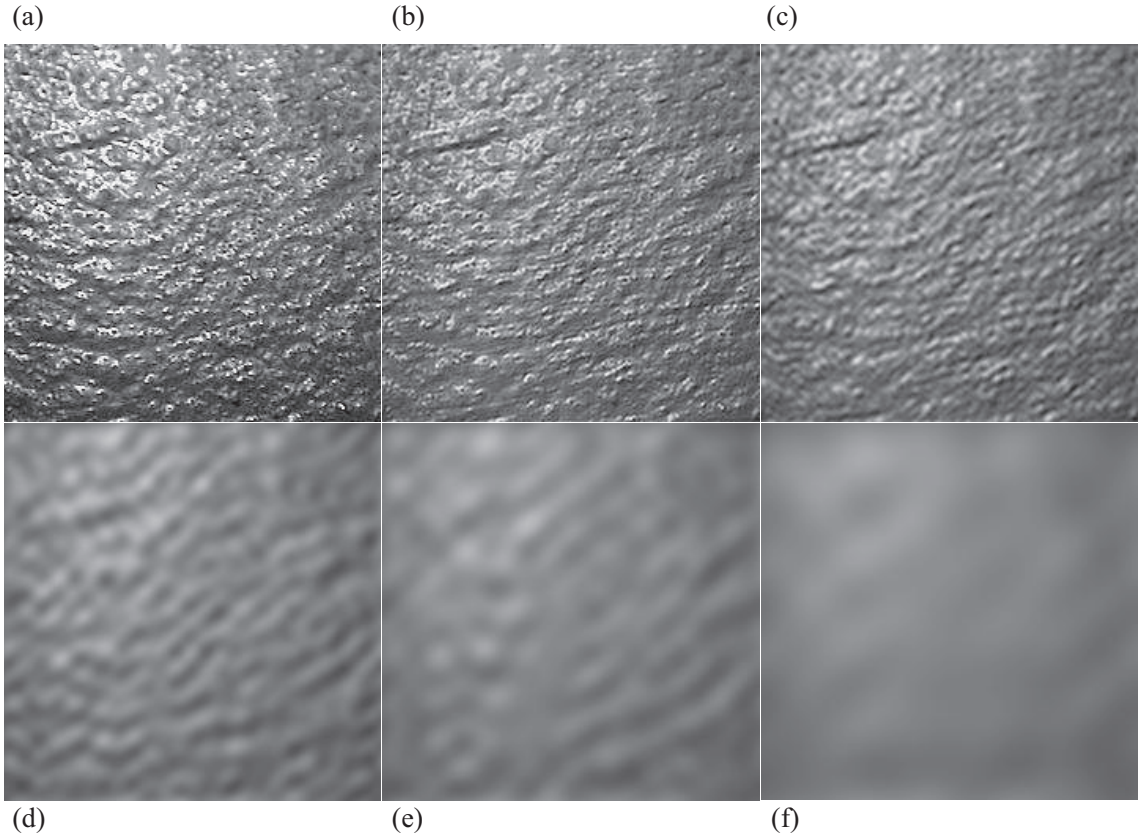

Figure 2.16: Filtered images for $2\bar{a} = 178$ μm, $\phi = 0.30$, $\alpha = 60.8^o$, and $h_o = 2.1$ mm (a) Original image (b) Longest wavenumber of 1.2 mm^{-1} ($\lambda = 5.3$ mm), (c) 2.6 mm^{-1} ($\lambda = 2.4$ mm), (d) 4.2 mm^{-1} ($\lambda = 1.5$ mm), (e) 12.6 mm^{-1} ($\lambda = 0.5$ mm), and (f) 20.9 mm^{-1} ($\lambda = 0.3$ mm). Images are 2.4 cm wide and 3.0 cm tall, where an individual pixel is 100 μm wide and 125 μm tall. The suspension is flowing from the top of the images towards the bottom.

2.4 Model

Here we develop a model for the particle concentration and bulk velocity as a function of location in a two dimensional suspension in inclined plane flow. The model is developed using the framework presented by Morris and Boulay [1]. A boundary condition for the free surface is evaluated and the model results are compared to the experimental results found in §2.3.1.

Gravity-driven Stokes flow of a film of Newtonian fluid down an inclined plane results in a quadratic velocity profile. The standard assumption of vanishing shear stress at the gas-liquid interface, or free surface, results in a flow mathematically identical to pressure-driven channel, or plane Poiseuille, flow with the gravitational driving force replacing the gradient of pressure, of form $u(\xi) = U_s[1 - (\xi/h)^2]$ with ξ measured from the free surface into the liquid or $\xi = h - z$, and where U_s is the surface velocity and h is the film depth. Suspensions of neutrally-buoyant particles in pressure-driven channel flow exhibit shear-induced migration, with elevated concentration developing in the center of the channel as the flow proceeds axially. It is thus natural to apply modeling successful for predicting migration phenomena in pressure-driven and other flows to the study of gravity-driven suspension film flow. The model we use is based on the suspension balance approach of Nott and Brady [7] with a different description of the normal stress rheology. The model formulation is largely similar to the description by Morris and Boulay [1] and the treatment will be kept brief except in those features which are introduced in this work, primarily to account for the free surface nature of the flow.

The new features considered here are the potential for a normal stress jump across the free surface and the free-boundary character of the upper surface of the film. The latter allows the mean film depth to vary as the mixture flows axially, and thus

provides the capability to match the experimentally observed thinning of the film, as shown by the $h(x)$ data in Table 2.2. The mean free surface takes on too weak a curvature to be of significant influence under the conditions studied, but the potential for a normal stress jump resulting from the smaller-scale deformation the mean free surface of the suspension is addressed below.

We consider flows in which the film-scale inertia ($Re_f = \frac{\rho^2 g_x h_o^3}{\eta_{S_o}^2} < 0.035$) and the particle-scale inertia ($Re_p = \frac{32\rho a^3}{3\eta h^2} u_{max} \leq 5 \cdot 10^{-6}$) are small, justifying neglect of inertia at all scales. In the suspension balance approach, neutrally-buoyant suspension flow at zero Reynolds number is described by mass and momentum conservation equations for the bulk mixture,

$$\nabla \cdot \langle \boldsymbol{u} \rangle = 0 \quad \text{and} \quad \nabla \cdot \boldsymbol{\Sigma} = \rho \boldsymbol{g}, \tag{2.15}$$

and for the particle phase. The mean suspension velocity and bulk stress are given by $\langle \boldsymbol{u} \rangle$ and $\boldsymbol{\Sigma}$, respectively. Particle mass conservation is described by

$$\frac{\partial \phi}{\partial t} + \langle \boldsymbol{u} \rangle \cdot \nabla \phi = -\nabla \cdot \boldsymbol{j}_\perp \tag{2.16}$$

in which $\boldsymbol{j}_\perp \equiv \phi(\boldsymbol{U} - \langle \boldsymbol{u} \rangle)$ is the suspension flux relative to the mean motion, with $\boldsymbol{U}$ the mean velocity of the particle phase, which is governed by

$$0 = \nabla \cdot \boldsymbol{\Sigma}_p - \frac{9\eta}{2a^2} \phi f^{-1}(\phi)(\boldsymbol{U} - \langle \boldsymbol{u} \rangle), \tag{2.17}$$

for neutrally buoyant particles[1] in which the last term represents the hydrodynamic force on the particle phase represented as analogous to a sedimentation (with f the sedimentation hindrance function) and $\boldsymbol{\Sigma}_p$ is the particle contribution to the bulk stress, modeled as

$$\boldsymbol{\Sigma}_p = -\eta \dot{\gamma} \boldsymbol{Q}(\phi) + 2\eta \eta_p(\phi) \boldsymbol{E}, \tag{2.18}$$

[1] As shown in Morris and Brady [31], only the difference in density $\rho_p - \rho_f$ enters in this equation.

where η_p is the dimensionless particle contribution to the suspension viscosity, and $\boldsymbol{E}$ is the local bulk rate of strain, $\dot{\gamma} = (2\boldsymbol{E}{:}\boldsymbol{E})^{1/2}$. The normal stresses are specified by the dimensionless material property tensor $\boldsymbol{Q}$, which is taken to be

$$\boldsymbol{Q}(\phi) = \eta_n(\phi) \begin{pmatrix} 1 & 0 & 0 \\ 0 & \lambda_2 & 0 \\ 0 & 0 & \lambda_3 \end{pmatrix} \equiv \eta_n(\phi)\hat{\boldsymbol{Q}}, \tag{2.19}$$

where $\eta_n(\phi)$ is termed the "normal stress viscosity." The sedimentation hindrance function, f, relates the sedimentation rate of a homogeneous suspension of spheres at volume fraction ϕ to the isolated Stokes settling velocity, *i.e.*, $f(\phi) = U_{sed}(\phi)/U_{sed}(0)$. A standard form, $f(\phi) = (1-\phi)^{\alpha}$, is used here [32] with $\alpha = 4$. The anisotropy of the stress is given by $\lambda_{2,3}$ differing from unity, with values of $\lambda_2 = 0.5$ and $\lambda_3 = 0.8$ providing best fits of various suspension flows. It is important to note that the vorticity direction is placed in the 2 position and the gradient in the 3 position, which is unusual (and differs from the original work). Here, we are interested only in Σ_{22} but have provided the full constitutive behavior for completeness. The particle contributions to the shear and normal stress viscosities were treated empirically as

$$\eta_p = 2.5\eta\phi_{\max}\left(1-\frac{\phi}{\phi_{\max}}\right)^{-1} + K_s\eta_c\left(\frac{\phi}{\phi_{\max}}\right)^2\left(1-\frac{\phi}{\phi_{\max}}\right)^{-2}, \tag{2.20}$$

$$\eta_n = K_n\eta\left(\frac{\phi}{\phi_{\max}}\right)^2\left(1-\frac{\phi}{\phi_{\max}}\right)^{-2}, \tag{2.21}$$

where $\phi_{\max}$ is the maximum packing fraction, and $K_s = 0.1$ and $K_n = 0.75$ provided reasonable agreement with experimental data.

The problem studied is steady in average but axially varying, and variations of stresses in the axial direction are much smaller than those across the channel. These features reduce the governing equation for $\phi(x,z)$ to

$$\langle u_x\rangle\cdot\frac{\partial\phi}{\partial x} = -\frac{\partial j_z}{\partial z} = -\frac{2a^2}{9\eta}\frac{\partial}{\partial z}\left(f(\phi)\frac{\partial\Sigma_{zz}^P}{\partial z}\right) \tag{2.22}$$

in which it is assumed that the average mixture velocity has only an axial component in writing the left-hand side. Note that z in this problem is the direction of the velocity variation, or the gradient direction, and thus $\Sigma_{zz}^P = \Sigma_{22}^P$. The boundary conditions associated with (2.22) are that no particle flux occurs through either the solid boundary or the free surface; we require constant axial flux of both particles and bulk suspension at any value of x, which condition is related to the determination of the free surface position (*i.e*, to the value of $h(x)$).

We assume the particles move with the mean suspension velocity in the axial direction, neglecting the lag velocity of $O[(2a/h)^2]$ predicted by Faxén's law. The solution is obtained using a marching method, such that the axial momentum equation uses only local information, meaning values at the axial position x of interest,

$$0 = -\frac{dP(x)}{dx} + \frac{\partial}{\partial z}\left(\eta_s(\phi)\frac{\partial u_x}{\partial z}\right) \tag{2.23}$$

and from this we determine u_x and $\dot{\gamma} \equiv |\frac{\partial u_x}{\partial z}|$. This information, along with the profile $\phi(z)$ at this x, is used to evaluate Σ_{zz} and its variation with z, and hence the cross-stream particle flux due to particle migration, j_z. This leads to the update equation for ϕ which, following from (2.22), yields

$$\Delta\phi = -\frac{\Delta x}{u_x(z)}\frac{\partial j_z}{\partial z} = -\frac{2a^2\,\Delta x}{9\eta\,u_x(z)}\frac{\partial}{\partial z}\left(f\frac{\partial \Sigma_{zz}}{\partial z}\right). \tag{2.24}$$

In order to apply the model to the film flow, a boundary condition for the free surface must be developed. Considering the local conditions at a free surface, a normal stress jump is admitted across the interface. This does not have much effect. The normal stress jump at the free surface is set as follows,

$$\Sigma_{zz} = \Sigma_{zz(o)} - C \cdot \eta_n \cdot \frac{\overline{u_x}}{h}$$

where $\Sigma_{zz(o)}$ is the locally calculated particle stress. The second term on the right hand side of the above expression is the nonlocal portion of the particle stress. Increasing

Table 2.4: Effect of C on dimensionless film thickness (h/h_o) for $\phi_{\text{bulk}} = 0.30$.

C	h/h_o
10	0.997
2	0.980
1.3	0.913
1.1	0.907
1.1	0.905
1.0	0.903
0.1	0.852
0.01	0.847
0.001	0.842

the magnitude of the particle stress everywhere in the film causes a normal stress jump at the free surface. The variable C was varied from 0.001 to 10. The migration effect was significantly reduced for values of C on the order of 1. Only small differences in the velocity and concentration profiles were seen, and the film thickness changed by less than 2% between the model solution for $C = 0.001$ and 0.1. The dimensionless film thickness is closest to the experimentally determined dimensionless film thickness for values of $C \leq 0.10$.

The model velocity scales with α, and h_o^2 in the same manner the experimentally determined velocity does. However, the fully developed model velocity profile found is significantly slower than the fully developed experimentally determined velocity near the wall, but faster than the experimentally determined velocity near the free surface. In an attempt to gain more agreement between model and experimentally determined velocity profiles an *ad. hoc.* method was used to modify the particle stress. The stress field was increased at the wall and then allowed to decay exponentially back to the unchanged stress field with distance from the wall,

$$\Sigma_{zz} = \Sigma_{zz} \cdot \left[1 + \beta \cdot exp\left(-\frac{h^* - z}{\epsilon}\right)\right], \tag{2.25}$$

where ϵ can be thought of as a/h_o which was set to 0.05 for all model results presented in this work.

The β effect on the fully developed velocity profile can be seen in Figure 2.17 (a). As β is increased the particle concentration at the wall decreases. Increasing β to a value of 50 forces the fully developed model velocity to match the experimentally determined velocity near the wall however the velocity near the free surface predicted by the model is still larger than the experimentally determined velocity. The reason for this difference can be seen by comparing the model concentration profile to the implied concentration found from the two layer Newtonian viscosity model that was applied to the experimentally determined velocity profile. The concentration predicted by the model, shown in Figure 2.17 (b), is low near the solid wall and then rises sharply to the concentration at the free surface. We believe that the model over estimates the concentration near the free surface. If the concentration was lower near the free surface, and therefore higher in the middle of the film, the velocity at the free surface would be slower.

Li and Pozrikidis [13] have simulated suspensions of solid particles in Stokes flow films; these authors have also considered film flows of suspensions of deformable drops [12]. They find that a single particle in inclined plane flow moves away from the free surface. For a single particle in inclined plane flow, the crest of the disturbance created in the free surface is upstream of the particle. This results in a net surface force on the particle pushing it away from the free surface balanced by drag due to downward velocity of the particle relative to bulk flow to achieve a force-free condition. Finite solid fractions up to areal fraction $\phi_A = 0.1$ were computed but no results describing the distribution are given. Note that calculations for areal fractions up to $\phi_Z = 0.2$ were reported in Li and Pozrikidis [12] showing that the dispersed drops were generally pushed away from both the solid and free surface.

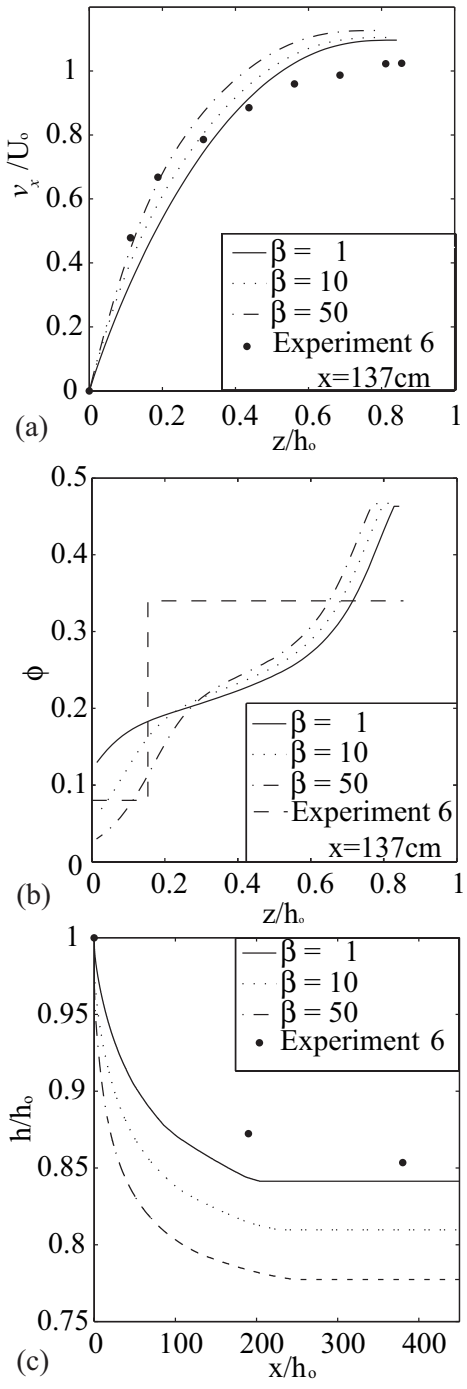

Figure 2.17: Model predicted (a) dimensionless fully developed velocity compared to experimentally determined velocity, (b) fully developed particle concentration profile, and (c) evolution of the film thickness.

The results of Li and Pozrikidis [12, 13] suggest that the particle concentration near the free surface is being over-estimated by our model, which implies that the normal stress jump produced by the boundary condition we have chosen at the free surface is not large enough, or is of inappropriate form. However when the variable C is increased there is insufficient migration away from the solid surface. This suggests the boundary condition we have chosen at the free surface is not of a proper form.

The model in its current form predicts that the scaled film thickness will decrease with increasing ϕ, and that the scaled velocity will increase with ϕ. This can be seen in Figure 2.18 (b). The model results presented in Figure 2.18 (c) suggest that PIV experiment 2, shown in Table 2.2 did not reach a fully developed state.

2.5 Conclusions

We have shown experimentally that, in free-surface, inclined-plane flow of a suspension, particles migrate away from the solid surface. We have also shown that the film thickness decreases as the fluid flows down the inclined plane until it reaches its fully developed thickness, at some location downstream from where it began. These results agree with modeling results.

There is not sufficient information to make conclusive statements about the particle concentration next to the free surface. This is necessary to properly model the boundary condition at the free surface. Although the mean location of the free surface is flat, the root mean square curvature is not zero; therefore as the work of Li and Pozrikidis shows [13] it is possible for the free surface to push the particles away, and therefore decrease the local particle concentration. It is important to understand the correlation between the surface shape and the location of the particles in the flow. This would allow the direct determination of whether the surface pushes the particles away.

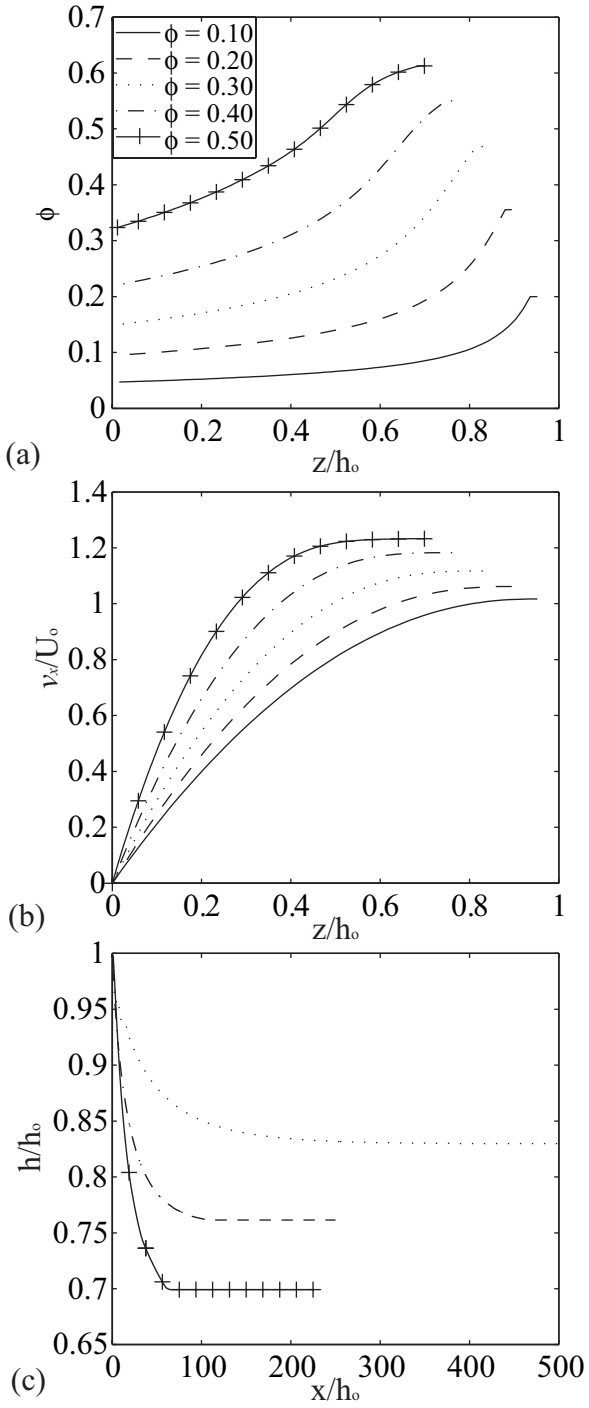

Figure 2.18: Model solutions for various ϕ_{bulk} with $\beta = 0$, and $C = 0.10$. (a) Model ϕ profile. (b) Model velocity ϕ dependence. (c) Evolution of h/h_o. The fully developed location of h/h_o for $\phi = 0.10$ and 0.20 occurs at 10,000 and 2,750 respectively and was omitted from (c). The legend in (a) applies to all plots in this figure.

CHAPTER III

CONCENTRATION BAND DYNAMICS IN FREE-SURFACE COUETTE FLOW OF A SUSPENSION

3.1 Introduction

Despite[1] its intrinsic interest to coatings applications, the interaction of a flowing bulk suspension with a free surface has received little attention. The usual approach in such flows has been to treat the suspension as an effective fluid in which the particles alter the rheology. Recent observations of a segregation phenomenon in the free-surface suspension flow generated by partial filling of a concentric-cylinder shear flow (Couette) apparatus with a viscous suspension have, however, demonstrated that the presence of a free surface in a particle-laden flow can have remarkable effects. In particular, we note the axial concentration banding in a partially-filled horizontal Couette flow, recently examined for viscous flow conditions by Tirumkudulu, Tripathi, and Acrivos [17], although photographs showing similar axial particle fraction variation in the same flow geometry at much larger Reynolds number were presented

[1]This chapter appeared as "Concentration band dynamics in free-surface Couette flow of a suspension" by Brian D. Timberlake and Jeffrey F. Morris in Physics of Fluids. (2002) **14**,1580-1589

earlier [33]. A similar segregation has been observed in flow of a suspension partially filling a single rotating cylinder [19, 16]. While axial segregation of dry granular materials flowing in the latter geometry is well-known, free-surface-induced segregation in viscous suspensions occurs at vanishingly small inertia and is of a different origin.

The phenomenon of interest is the following: when a noncolloidal suspension partially fills the annulus between the cylinders in a Couette device to leave a free surface, rotation of the inner cylinder results in axial segregation of the suspended particles into alternating concentrated and dilute bands. The mechanism leading to this segregation remains an open question. In the initial observation in a Couette device [17], the particles and fluid were equal density (neutrally buoyant), but the occurrence of banding in free-surface flows is not limited to suspensions of neutrally-buoyant particles as was shown in experiments using heavy particles by Boote and Thomas [19] in a partially-filled rotating single cylinder.

Shear-induced migration in concentrated suspensions leading to nonuniform particle concentration in fully-bounded suspensions has been of considerable interest for over a decade [8, 6, 7, 1], with some of this work specifically considering the radial migration in wide-gap Couette flow [7, 1]. It is natural to consider that shear-induced migration may play a role in the axial segregation under a free surface, but segregation in a partially-filled Couette device has previously been reported [17] to occur at a particle volume fraction of $\phi = 0.05$, and in this work has been observed to occur in a suspension of $\phi = 0.01$. The multiparticle interactions necessary to generate the changes in rheology leading to shear-induced migration scale as ϕ^2 in the dilute limit [8, 7, 1], and a scaling analysis presented in §3.4 suggests that this mechanism would yield a migration rate too slow to explain the observed behavior at larger ϕ as well.

The range of behaviors possible in the free-surface Couette flow was not clear from

the prior study. This work aims to expand understanding by considering free surface-induced segregation in a Couette flow under viscous-flow conditions differing in two ways from those of Tirumkudulu *et al.* [17]. In that work, the bands bridged the entire gap between inner and outer cylinder. Because our interest is in examination of the dynamics of the bands, this bridging which restricts the motion of the bands is undesirable. Thus we study the free-surface flow in a Couette device with a ratio of inner to outer cylinder radii, $R_i/R_o = 0.29$, which is markedly smaller than the value of 0.64 in the prior work. A photograph at a typical condition of 50% fill of the annular space with a suspension of bulk average particle fraction $\phi_{\text{bulk}} = 0.2$ is shown in Figure 3.1. Second, the inclination of the entire Couette device with respect to gravity has been allowed to vary. These changes are apparently simple ones, yet each opens a window to dynamics previously unobserved. Reducing R_i/R_o removes the interference by the outer cylinder, and also allows us to examine flows with free surfaces of qualitatively different form. Specifically, the free surface of the suspension may either cover the driving inner cylinder or not before flow commences, depending on the fraction of the cylindrical annulus filled with suspension. Previously unobserved phenomena occur at large fill fraction, meaning that the inner cylinder is completely covered prior to flow. Here, the segregation rate becomes progressively slower with increasing fill fraction, but the concentrated bands are eventually separated by narrow zones essentially devoid of particles.

The most striking novel behavior reported here is due to inclination of the Couette device. Inclination breaks a basic symmetry found in prior studies, [17, 19, 16] and under inclination, concentration bands migrate down the axis away from the elevated end of the device. In general, the bands are identifiable over many hours as bands form periodically at the elevated end of the device to form a train of bands which flow down the axis, with individual bands remaining intact for the entire transit of

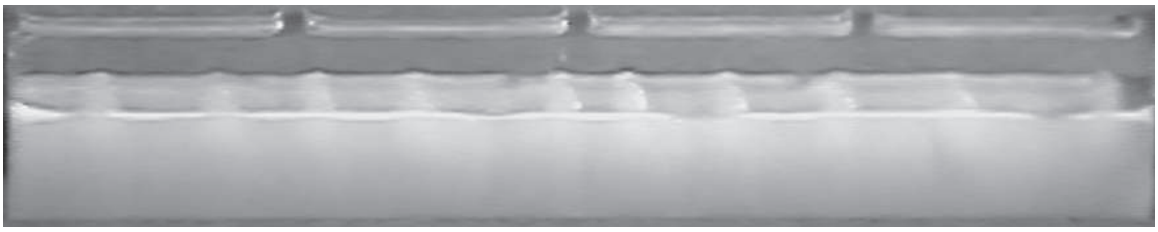

Figure 3.1: Concentration bands formed in the Couette device with inner to outer cylinder ratio of $R_i/R_o = 0.29$ at a fill fraction of $f = 0.50$ and particle volume fraction of $\phi_{\text{bulk}} = 0.2$. The rotation rate is 8 RPM and the particles are neutrally buoyant.

the device.

The following section provides a description of our experimental methods and image analysis techniques. The number of parameters of the problem is large, and to provide context for the conditions probed by this work, a dimensional analysis of the suspension-flow problem in the Couette device is presented in §3.2.4. Results of our experiments are presented in §3.3, with conclusions drawn from our investigations presented in §3.4. This final section also includes a discussion of a proposed mechanistic basis for the onset of the segregation.

3.2 Experimental procedures

3.2.1 Suspensions and apparatus

Our experiments were performed in a concentric cylinder, or Couette, device shown schematically in side and end views in Figure 3.2. The actual device is seen from the side in Figure 3.1. This device consists of two concentric, 27.2 cm cylinders. The outer cylinder is a tube of Lexan (polycarbonate plastic), and the solid interior cylinder is stainless steel. The annulus is closed at each end by Lexan caps into which a sealed bearing is mounted, allowing the inner cylinder to turn while the outer cylinder is stationary. The cylinder motion is driven by a 1/15 horsepower electric motor. The

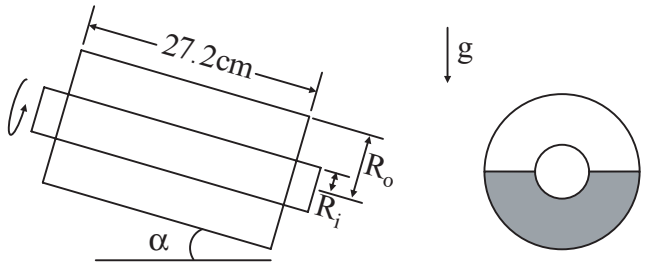

Figure 3.2: Schematic in side and end views of the Couette device. The inner cylinder is stainless steel and has radius $R_i = 0.6$ cm, while the outer Lexan cylinder has inner radius $R_o = 2.2$ cm, and the annulus has length $L = 27.2$ cm.

device can be mounted horizontally (axis perpendicular to gravity) or in an inclined position; as seen in Figure 3.2, this inclination is defined by the angle, α, which the cylinder axis makes with the horizontal. Angles studied were $0 \leq \alpha \leq 6.5^o$.

The radius of the solid inner cylinder is $R_i = 0.64$ cm, while the outer cylinder has inner radius $R_o = 2.2$ cm, and the annulus has length $L = 27.2$ cm. The fill fraction occupied by the suspension is given by $f = V_{susp}/\pi(R_o^2 - R_i^2)L$; the volume of suspension, V_{susp}, in the annulus was determined from the known suspension density and the measured mass of suspension placed into the device.

Two types of outer cylinder were used. For sufficiently small fill fraction, an outer cylinder with four 2.54 cm by 6.2 cm rectangular holes in the top was used, allowing easier filling and optical access to the annular region. Larger fill fractions required, in order that suspension not spill, the use of a complete outer cylinder which was filled through two 0.6 cm radius circular holes.

Spherical poly-(methyl methacrylate) (PMMA; ICI Acrylics) particles were sieved to diameters in the range $2a = 250$–300 μm where we introduce a for the radius. The suspending fluid was a mixture of 76% Triton X-100 (t-Octylphenoxypolyethoxyethanol, a surfactant produced by Sigma), 16.2% zinc chloride ($ZnCl_2$), and 7.8% water, with the percentages based on mass. This mixture was density-matched ($\rho = 1.180$ g/cm^3)

and roughly refractive index (RI)-matched to the PMMA particles (RI = 1.491 at $T = 20^o$C). This suspending liquid mixture had a viscosity of $\mu = 160$ Poise at $T = 20^o$C. A few runs used the Triton X-100-based suspension with different ratios of components in order to vary the ratio of fluid to particle density (ρ_f/ρ_p) from unity. These will be noted where the results are described.

3.2.2 Particle concentration measurements

The particle concentration was measured in a limited number of experiments by direct sampling of the suspension from the Couette device. A variable volume pipette with tip manually cut to an opening of diameter 1.5 mm was used to remove approximately 0.3 cm^3 of fluid from a position in the flow. The mass of the sample, m, was determined by weighing the pipette and sample together and subtracting the previously-determined weight of the pipette tip alone. The suspending liquid was removed by flooding the suspension with warm water in a 20 μm sieve. The captured particles were dried and weighed to find their mass, m_p. The suspensions sampled were made up of neutrally buoyant particles and fluid, yielding $\phi = m_p/m$. The method was determined to be accurate to ± 0.01 in the absolute value of ϕ based upon sampling from known-ϕ suspensions.

3.2.3 Band tracking

Band positions and velocities were determined for many of the experiments from time-lapsed video imaging of the Couette device taken for the duration of an experiment. This video was digitally downloaded from videotape to a personal computer by video capture card. Individual images were analyzed by an algorithm, implemented using the Matlab Image Processing Toolbox, to determine positions of all identifiable bands, with bands recognized by characteristic image properties. For example, at small f,

the concentrated bands cause an elevation of the free surface, and there is an increase in the intensity of the light reflected from the band to the camera, relative to the reflection from the undisturbed free surface. The algorithm was "tuned" for each condition (for example, through the threshold level of the light intensity associated with a band) in order that the band positions captured computationally agreed with direct visual inspection. The information on band positions obtained in this manner was further processed using a minimum spanning tree algorithm [34], which serves to identify bands by finding points forming lines (straight or curved) in a space-time plot of band positions. Once points had been grouped, groups with fewer than ten points were discarded, as these are determined by visual inspection of the video to be spurious in most cases.

3.2.4 Dimensional analysis

The scope of our study is limited primarily to examination of the role of f and α upon the segregation phenomenon, with examination of limited ranges of certain other variables. Because numerous parameters are needed to fully characterize mixture flow in the Couette device, the number of relevant dimensionless variables needed to describe the problem in the general case is rather large. A dimensional analysis is presented here to delineate the factors which may influence the flow phenomena under the conditions studied.

We study the flow of a suspension with a very viscous suspending fluid. The bulk scale Reynolds number, $Re_R = \rho_f 2\pi\omega R_i \Delta R/\mu$ with $\Delta R = R_o - R_i$, satisfies $Re_R < 0.1$ for all conditions described and the Reynolds number based on the particle scale is much smaller, $Re = (a/\Delta R)^2 Re_R = O(10^{-6})$. Inertia is thus negligible. Particle sedimentation is negligible for the standard case of neutrally buoyant particle suspensions, although we have examined cases with weak positive and negative

particle buoyancy. The particles are of noncolloidal scale at 250–300 μm in diameter and are readily dispersed in the surfactant solution used as suspending fluid. Brownian motion and nonhydrodynamic interparticle forces are therefore also negligible influences.

Geometric variables include the ratios $a/(R_o - R_i)$ and R_i/R_o, both of which are held fixed. Also fixed for our examination of the role of f and α is the bulk particle volume fraction, ϕ_{bulk}. Our studies find that banding occurs in a horizontal device over the range $0.01 \leq \phi_{\text{bulk}} \leq 0.40$. We have not probed outside this range.

The remaining dimensionless variables for a monodisperse suspension are the fraction of the annulus filled by suspension, f, the angle of inclination, α, and the ratio of gravitational to viscous stresses given by

$$G \equiv \frac{\Delta\rho g R_i}{\mu\omega},$$

where $\Delta\rho$ is the density difference between the suspension and the overlying fluid, ω is the angular velocity of the inner rod of radius R_i, and μ is the suspending fluid viscosity. A measure of the role of surface tension through a capillary number (viscous to surface tension effects) or Bond number (gravity to surface tension effects) is also needed based simply on dimensional considerations. Although it is expected that particle motions at the free surface may be influenced by surface tension [35, 36, 37, 38, 39], we have not successfully examined this issue.

The primary variables considered here are the fill fraction, f, the angle of inclination, α, and the rotation rate of the inner cylinder, ω, typically expressed in rotations per minute (RPM). Although the rotation rate varies the dimensionless quantity G, results are presented only for a suspension with fixed physical properties and it is convenient to describe the results in terms of the dimensional rotation rate.

3.3 Results

As in prior experimental examination of free-surface Couette flow of a suspension [17], we observe the formation of particle-rich bands separated in the axial direction by relatively dilute regions. However, we have also observed several features of the phenomenon not previously described, and we summarize these here. These include bands undergoing a fluctuational motion, coalescence (two bands combine to form one) or simple disappearance of bands, and uniform-speed axial migration of the bands when the device is angled relative to the horizontal. We have also determined that the banding has different regimes depending upon whether the fill fraction of the annulus is less or greater than the fraction leading to coverage of the inner cylinder without flow, defined as $f \equiv f_c$ with $f_c \approx 0.65$ for the apparatus of this study. The banding rate slows dramatically, the bands increase in axial extent, and the number of bands decreases for $f > f_c$.

The focus in the investigations reported here was on the experimental characterization of band formation and dynamics for a range of f and inclination angle, α. The majority of these were performed at $\phi_{\text{bulk}} = 0.2$ and our standard rotation rate was $\omega = 8$ RPM; where it is not noted, these are the values used for these variables. We begin by considering in §3.3.1 the influence of inclination angle upon the band dynamics, followed by a consideration of the influence of fill fraction in §3.3.2; the experiments which probed these dependencies are numerous and appear to adequately demonstrate the range of behaviors. We have also examined in more limited studies the influence of varying the rotation speed of the driving cylinder, the role of weak particle buoyancy, and the spreading of a drop of suspension; the latter study was performed to gain insight to drainage flows of suspensions. A brief description of results from these experiments is presented in §3.3.3.

3.3.1 Influence of inclination angle, α

Our experiments have shown that for appropriate conditions, the concentrated bands form and move at nearly constant speed, v, down the axis of the Couette for inclination angles $0.8^o \leq \alpha \leq 5.3^o$. In general, as shown by Figure 3.3 for $\phi_{\text{bulk}} = 0.2$, $f = 0.50$, and $\omega = 8$ RPM the speed increases with increasing angle. At each value of α, several points are plotted. The velocity points plotted each correspond to the velocity of a particular band; because the band velocity varied slightly with time and with location of the band in the Couette, several fairly-closely grouped values of the velocity are found for a single experiment. At $\alpha > 5.3^o$, bands are no longer observed to form. However, at these large angles, particles concentrate at the "lower" end of the Couette, *i.e.*, at the end where the fluid is deeper. For $\alpha = 6.5^o$, $f = 0.50$, and a bulk fraction of $\phi_{\text{bulk}} = 0.2$, the steady-state concentration was measured at a several points along the axis, with the results shown in Figure 3.4. It should be noted that for angles sufficiently large, $\alpha > 4.5^o$, the inner cylinder is raised completely out of the suspension at its elevated end and the process of band formation and motion is clearly altered. This is the reason for the break in the linear increase of v with α seen in Figure 3.3, but it is important to emphasize that even for angles $4.5^o < \alpha < 5.5^o$ bands continuously formed over the leftmost wetted portion of the inner cylinder.

From image analysis of the time-lapse video, the band positions have been identified. We consider first the band dynamics for zero and very small inclination angles. The axial positions of all of the identified bands as functions of time, $Z(t)$, are seen in Figure 3.5 (a) and (b), respectively, for representative experiments at $\alpha = 0$ and $\alpha = 0.4^o$. All cases for which results are presented in Figure 3.5 are at $\phi_{\text{bulk}} = 0.2$, $f = 0.50$, and $\omega = 8$ RPM. In the case of zero inclination, $\alpha = 0$, the particle-rich band positions are found to fluctuate. Near the ends of the annulus, the band motion

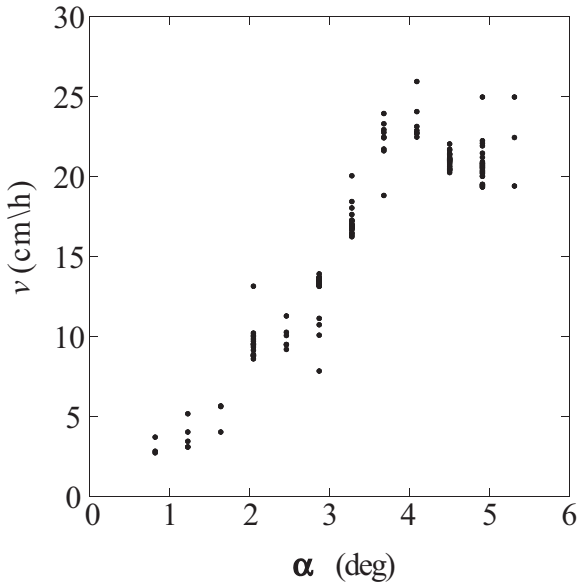

Figure 3.3: Measured band velocity as a function of the incline angle α, for the conditions $\phi_{\text{bulk}} = 0.2$ and $f = 0.50$, and inner cylinder rotation rate of 8 rotations/minute. The velocity plotted is the velocity of a particular band. The range of velocities determined for all bands measured is shown at each angle.

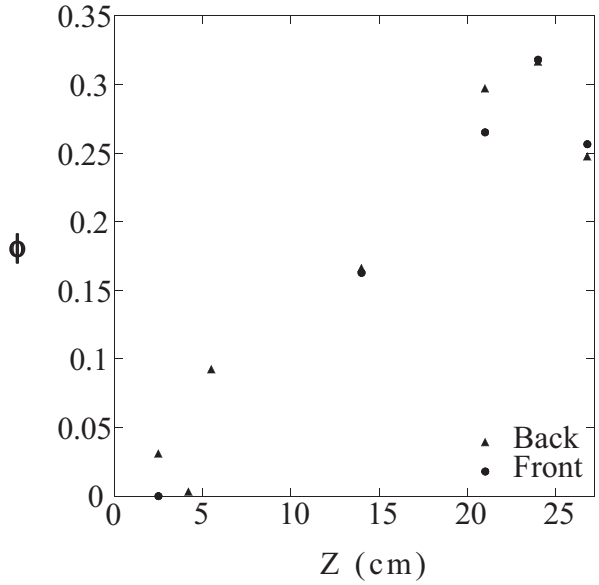

Figure 3.4: Measured particle fraction along axis at $\alpha = 6.5^o$ for the conditions $\phi = 0.2$ and $f = 0.50$, and inner cylinder rotation rate of 8 rotations/minute. Here, "front" is defined as the side of the device on which the cylinder surface moves up, while "back" is defined as the side of the device on which the cylinder moves down.

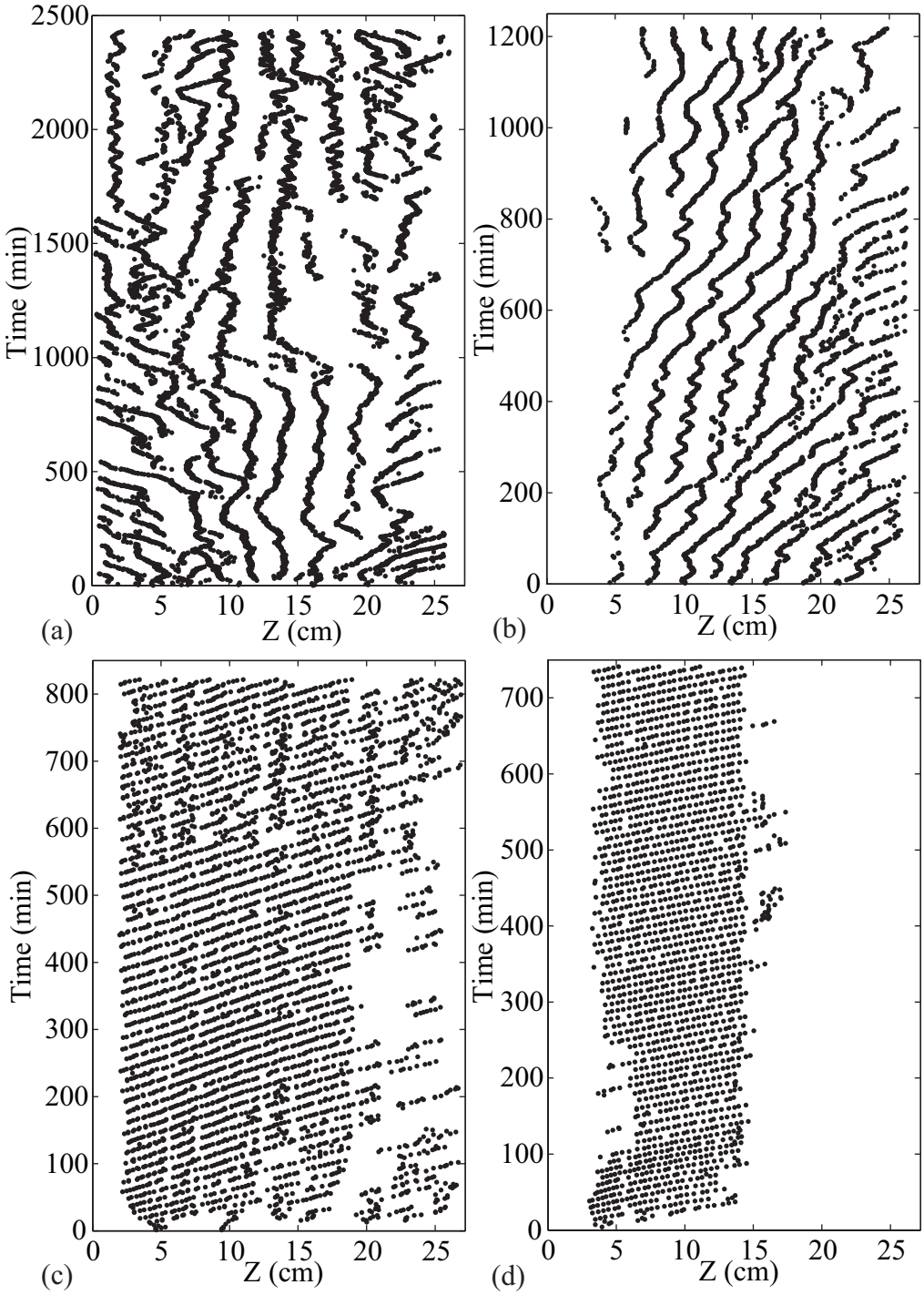

Figure 3.5: Diagrams showing the concentration band positions as functions of time in the (a) horizontal Couette ($\alpha = 0$), and at inclination angles of (b) $\alpha = 0.4^o$, (c) $\alpha = 2.0^o$, and (d) $\alpha = 3.3^o$. Time was set equal to zero when the presence of bands was first observed. In all cases, the suspension is at $\phi_{\text{bulk}} = 0.2$ and the inner cylinder rotates at 8 rotations/minute.

is biased by the fixed endcaps (in a manner we do not understand), but in the center of the device the bands undergo an unbiased oscillatory motion with a characteristic time of 60–80 minutes; the motion is not sufficiently regular to define a period, as seen in Figure 3.5 (a). Similar oscillatory motion is observed for small angles, but is accompanied by an average motion of the bands from the elevated to the lower end of the device. Note also that there is correlation between the motions of adjacent bands; for example, consider t = 200–500 minutes in Figure 3.5 (b), which illustrates the band dynamics for $\alpha = 0.4^o$. As noted the endcaps play a role, and for both $\alpha = 0$ and $\alpha = 0.4^o$, the tendency of the particle-rich bands to move toward and "die" at the ends of the device is evident. In the case of $\alpha = 0$, the bands near the center of the apparatus (between $Z = 10$ and 20 cm) last essentially for the entire experiment, of duration greater than 24 hours, while those near the ends of the Couette are seen to form, migrate toward the wall, and vanish in one to four hours. At $\alpha = 0.4^o$, the migration of bands on average is down the incline, but is far from uniform for bands at different axial positions. Bands at the low end (to the right in the diagram) are observed to migrate much more rapidly than those at the elevated end, and as a result vanish into the boundary. This difference in the axial speed of the bands, coupled with the fact that bands vanish as they encounter the end cap, results in gaps larger than what may be termed the "natural" spacing of the bands, and new bands form between existing bands. This event is readily apparent in a video image, and can be seen in Figure 3.5 (a) at $(Z = 9, t = 420)$ or $(Z = 12, t = 500)$, and in (b) at $(Z = 14, t = 260)$ or $(Z = 14, t = 350)$.

We turn now to larger angles of inclination. For $0.8^o \leq \alpha \leq 4.5^o$, the bands migrate at a rate which is seen from Figure 3.3 to be roughly linear in α: $v \approx k\alpha$ with $k \approx 5$ (cm/h)/degree of inclination. The band positions as a function of time for $\alpha = 2.0^o$ and $\alpha = 3.3^o$ are shown as Figure 3.5 (c) and (d), respectively. It is

important to note that the bands are separate and do not form a continuous spiral structure. These plots illustrate that regular band formation occurs at the elevated end of the apparatus (left in the diagram) followed by regular motion of the bands toward the lower end. As the bands move down axis at these values of α, the interband spacing remains nearly constant, which is evident from parallel lines formed by the sequential positions of adjacent bands in Figure 3.5 (c,d). This spacing is found to decrease as α increases.

To conclude, we note that observation of the complete dynamics in this flow requires, in general, experiments of many hours duration. Both the band fluctuational motions at small α and the slow evolution of the bulk concentration field at large α take place over many cylinder rotations. For intermediate α, relatively short experiments provide information on the band formation and motion down the axis, although as the experiments progressed the appearance of new bands near $Z = 0$ occurred at slightly longer intervals. This result is thought to be attributable to an apparatus-scale variation of the concentration similar to but weaker than that illustrated by Figure 3.4 for $\alpha = 6.5^o$. It is interesting to take note of this last observation from a different perspective: despite the motion of the bands, there is only a very slow net transport of particles toward the shallow end of the device.

3.3.2 Influence of filling fraction, f

We begin consideration of the influence of fill fraction by noting that the banding behavior depends qualitatively upon whether there is suspension completely covering the inner cylinder in the absence of flow. Note that all results in this section are for the horizontal configuration, $\alpha = 0$. For $f < 0.65$, the free surface of the mixture at rest lies below the topmost point on the inner cylinder, and the film formed over the inner cylinder is due entirely to the flow. The depth of the suspension over the inner

cylinder in the absence of flow, as a function of f, is illustrated in Figure 3.6 (a).

As f increases beyond $f \approx 0.65$, the number of bands decreases, the width of a band increases, and the number of rotations required for band formation increases dramatically. To illustrate the difference in the band structure, bands formed at $f = 0.50$ and $f = 0.90$ are illustrated in Figure 3.6 (b) and (c), respectively.

The observed range in number of bands as a function of f is plotted in Figure 3.7; the number of bands fluctuated during the course of an experiment and thus a range is plotted. For $f = 0.50$, eight to eleven bands are present, while at $f = 0.90$ only three bands form. The abrupt change in number of bands occurs at $f \approx 0.65$, a value distinguished by the fact that the inner cylinder is just covered by suspension at $f = 0.65$ in the absence of flow, as illustrated in Figure 3.6 (a). For this reason and its impact on the observed banding, we define $f_c = 0.65$ as a critical fill fraction for $R_i/R_o = 0.29$.

The concentration banding structure for $f > f_c$ is qualitatively different from that observed for small fill fraction. The concentrated bands are wider, and for $f > 0.8$, the regions between the bands are swept essentially free of particles after two to three days at 8 RPM (over 25,000 rotations). A similar complete removal of particles from the dilute regions is observed for certain parameters in the segregation associated with suspension in a partially-filled and rotating single cylinder[4]. For the Couette flow at $R_i/R_o = 0.29$ in this work, this is in sharp contrast to the dilute regions formed for $f < f_c$. For $f < f_c$, the concentrated bands are at ϕ well above ϕ_{bulk}, but because of the narrowness of these elevated-ϕ regions, it is possible for the "dilute" regions to differ little from the bulk average concentration: we have made measurements of $\phi = 0.35$ within a band for $\phi_{\text{bulk}} = 0.2$, while the separating regions were measured at $\phi = 0.19$.

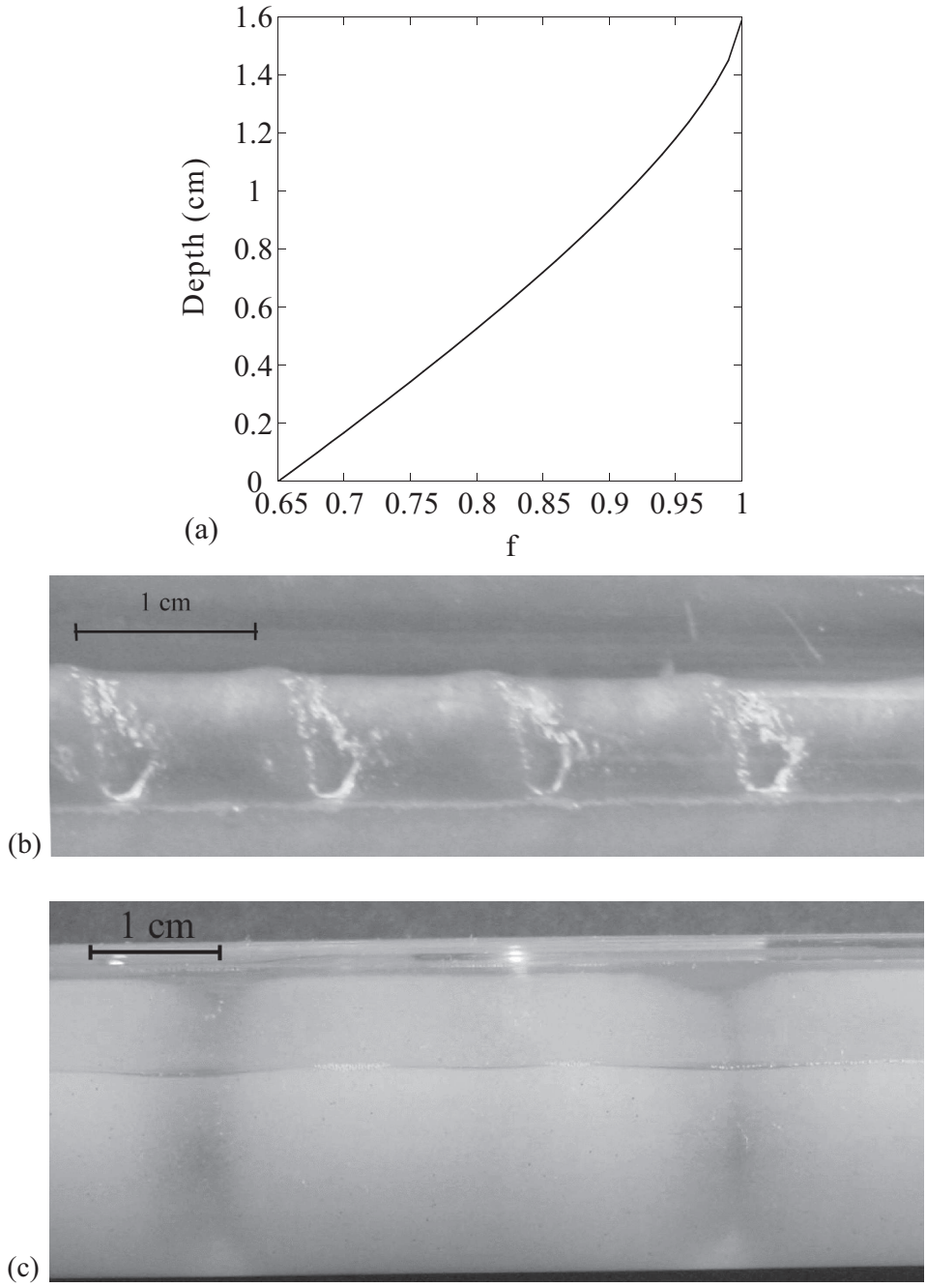

Figure 3.6: In (a) is a plot of film thickness (when the inner rod is not rotating) above the inner cylinder of the device at several f; $f_c = 0.65$ is the fill fraction at which the suspension just covers the inner cylinder. Photographs of bands at $f = 0.50$ and $f = 0.90$ at $\phi_{\text{bulk}} = 0.2$ and $\omega = 8$ RPM are shown in (b) and (c), respectively. The bands in (b) are observed after roughly 200 rotations of the inner cylinder, while those in (c) were first observable after approximately 25,000 rotations, and the image was taken after about 50,000 rotations.

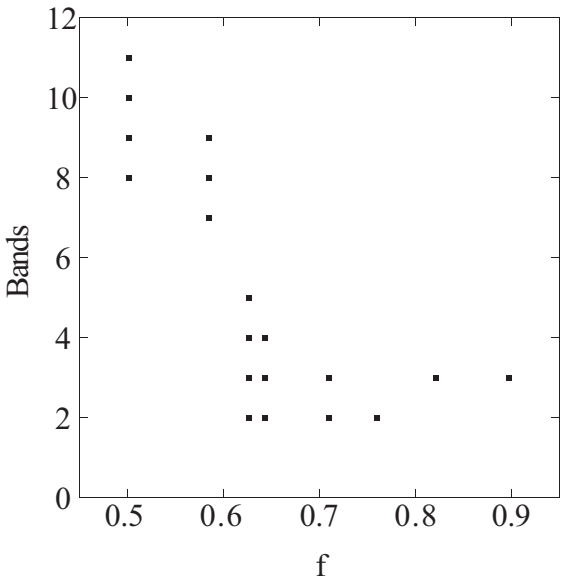

Figure 3.7: Number of bands observed for the Triton X-100/ZnCl/water suspension as a function of fill fraction for $\phi_{\text{bulk}} = 0.2$ at an inner cylinder rotation rate of 8 RPM. The symbols indicate the range of number of bands observed at a given f.

The characteristic time for band formation and fluctuational motion is also affected by fill fraction. It was noted above in the discussion of Figure 3.5 that the time required for accessing the full dynamics of the bands was many hours at small fill fraction, and this timescale increases dramatically for $f > f_c$. Considering a suspension of $\phi_{\text{bulk}} = 0.2$, for $f = 0.50$ bands are clearly apparent after about 200 rotations of the driving inner cylinder at a rotation rate of 8 RPM. By contrast, for the same volume fraction at $f = 0.90$ and 8 RPM, there was no observable concentration variation after 12,000 rotations (roughly one full day), definite bands were observed only after 25,000 rotations (two full days into the experiment), and ϕ in the dilute regions continued to decrease until it was essentially zero (after four days). The band motions described in §3.3.1 for $f < f_c$ are not observed at elevated f. For $0.5 < f < 0.7$, the bands are found to migrate at $\alpha = 0$, but this motion subsides rapidly with further

increase in f. For $f > 0.8$, the bands do not move measurably even over experiments of several days duration at the standard driving rate of 8 RPM.

3.3.3 Other results

Finite α at $f > f_c$: The behavior at small incline angle for high fill fraction was considered. This provided a test of the role of the film depth in the segregation process. At $\alpha = 0.7^o$ and $f = 0.75$, the free surface lay above the inner cylinder at all axial positions before flow commenced, but the minimum depth of suspension over the cylinder at the elevated and lower ends was equivalent to that in a horizontal Couette where $f \doteq 0.7$ and $f \doteq 0.8$, respectively. The expectation based upon arguments presented in prior work [16] was that bands would form, if at all, first at the elevated end of the device where the "film" was of least depth. A single band was, in fact, observed at the elevated end of the device within roughly 300 rotations of the cylinder. This band became more pronounced over the course of an hour and another band formed toward the opposite end of the device after several hours. These bands did not, however, migrate down the axis.

Rotation rate: At $\alpha = 0$, $f = 0.5$, and $\phi = 0.2$, the rotation speed was found to have the effects summarized in Table 1. The most notable variation occurred in the range $\omega = 4$–6 RPM, as the time for band formation was much larger at the slower rate and the number of bands was seven at $\omega = 4RPM$ and increased to 12 at $\omega = 6$ RPM. The formation time is an estimate based on the ability to clearly identify concentration bands on the videotape of the flow. The number of cylinder rotations for the formation of bands at 4 RPM was found to be over an order of magnitude larger than at 6 RPM (~ 1900 to ~ 160 rotations). Furthermore, the band structure for the lower rotation rate continued to evolve for a further ten hours after the bands were initially observed. The number of bands was found to be essentially constant

throughout an experiment for the 4 and 6 RPM conditions, but became quite variable as the rotation speed was increased to $\omega \geq 8$ RPM and is reported in Table 3.1 as the observed range.

It is important to note that along with the abrupt change in segregation rate from $\omega = 4$ RPM to $\omega = 6$ RPM, there is a qualitative change in the band structure. At the slower rate, the bands are similar to those formed at large fill fraction, $f > 0.65$ (see Figure 3.6 (c)), with broad concentrated bands separated by relatively narrow and very dilute regions. This change in behavior is apparently related to the fact that the drainage from the inner cylinder is more thorough at the slower rate. This results in a very thin film of the suspension on the inner cylinder, apparently too thin for band formation processes to occur as the bands are observed to form throughout the entire radius of the annulus (from R_i to R_o) at $\omega = 4$ RPM, rather than directly adjacent to the inner cylinder as seen at the higher rates. The mechanism which drives the axial migration is thought to depend upon gravity-driven flows caused by variations in surface elevation, as discussed in §3.4. The rotation rate has a visible influence on the thickness of the film on the inner cylinder, although we have not measured the thickness. A plausible argument for the similarity in structure of bands at the slow rate and $f = 0.5$ with that at $f > 0.65$ (and the relatively slow formation in both cases) is that these situations involve formation of bands over a relatively deep fluid layer rather than within a thin film. In the case of small ω at $f = 0.5$, the deep fluid is that in the annular region.

A comparison of the role of ω seen in this work with prior observations shows that the separation between the bands in a Couette device with $R_i/R_o = 0.64$ was found by Tirumkudulu *et al* [17] to increase with rotation rate, and the same trend was seen in the banding in a single cylinder by Boote and Thomas [19]. The latter study was at a larger Reynolds number. For $\omega = 4 - 6$ RPM, we observe the opposite

Table 3.1: Summary of band formation time and number of bands, reported as the complete range observed when variable, as a function of inner cylinder rotation rate, for $\phi_{\text{bulk}} = 0.2$, $f = 0.5$, and $\alpha = 0$.

Rotation rate, ω (RPM)	Band formation time (min)	Number of bands
4	480	7
6	26	12
8	21	8–11
12	6	9–12
16	4	9–12
24	5	8–10
32	–	9–11

trend, but as noted there is a change in band structure in this range of ω. For $\omega \geq 6$, our results show a trend similar to the earlier work, as the "average" separation between concentrated bands is observed to increase slightly with the driving rate: for a substantial fraction of the time the number of bands is at the lower end of the range shown. Due to the variation of number and the band motions described in §3.3.1, however, assignment of a single separation distance at a condition is not performed.

Non-neutral buoyancy: By altering the ratios of components, the liquid density was varied while keeping the viscosity roughly constant. The particles were the same PMMA particles used in all of the experiments. At the standard 8 RPM conditions and $\phi_{\text{bulk}} = 0.2$ at $\alpha = 0$, slightly less dense particles ($\rho_f/\rho_p = 1.38$) result in a behavior indistinguishable from that neutrally buoyant particles, while in our Couette geometry a weak excess particle density ($\rho_f/\rho_p = 0.89$) at the same conditions noted just above results in formation of bands which then detach from the inner cylinder and settle to the bottom of the annulus.

Spreading of a suspension drop on a wetted surface: The banding leads to elevated portions of the free surface, and prior work [16] has suggested that fluctuations of

the free surface could be a factor in the segregation behavior. These fluctuations could be due, for example, to viscosity variation caused by temperature of particle fraction variation. Such fluctuations lead to gravity-driven (drainage) flows for which there is little understanding in the case of suspensions. To gain some insight, simple experiments on the spreading of a suspension drop were performed, using a suspension of neutrally buoyant particles and fluid. In these experiments, the Triton X-100 suspending fluid is dyed very dark purple (RIT liquid dye, Wine 10) and the particle surfaces are dyed black (RIT liquid dye, Black 15). The PMMA particles used were in this case not from a narrowly sieved fraction and the diameters ranged roughly from 100–300 μm, with the majority of the volume in the 250–300 μm fraction. To examine the potential role of diffusion of dye, a drop of the dyed suspension was introduced from a wide-mouthed syringe below the surface in a volume of the undyed suspension. Because the dyed and undyed suspension were equal density, spreading was by diffusion only and was negligible compared with the spreading observed due to flow in the experiment described below.

A drop of dyed suspension, volume approximately 0.1 cm^3, is dropped from an orifice at a height of two centimeters onto a horizontal plate covered by a thin (sub-millimeter) flat film of the clear (undyed) suspending liquid only. The viscous drop lost its inertia almost immediately upon impact. The subsequent spreading behavior is illustrated by the sequence of images presented in Figure 3.8. These images are taken from a fixed vantage and focal point, with the first image shown, labeled by time $T = 0$ s, taken at the instant the image first came clearly into focus (after perhaps one second during which the initial curvature of the drop surface is reduced by spreading). This first image illustrates the rapid formation of a leading "foot" of the dyed suspending liquid, which is observed as a dark region advancing ahead of the particles. In the subsequent images, the region of clear fluid advances progressively

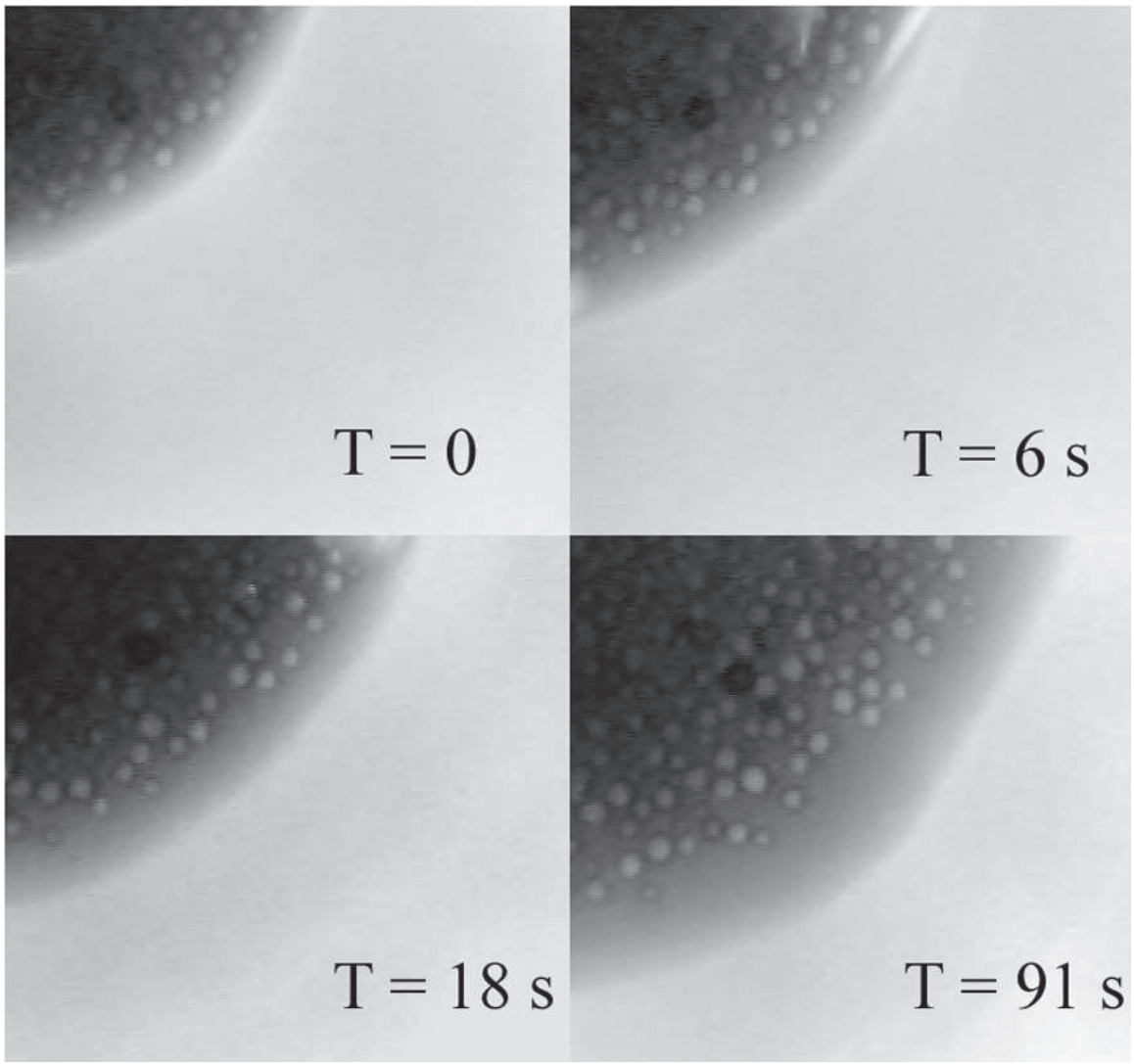

Figure 3.8: Sequence of four images in the spreading of a dyed drop of the Triton X-100 suspension, of $\phi = 0.2$, on a thin film of the suspending fluid. The times at which the images were taken are shown relative to an arbitrary zero time for the upper left image. The dark region free of particles results from the spread of the dyed suspending liquid.

further ahead of the particles, which also continue to spread. The characteristic distance between the fronts of the particle and fluid components of the drop is 600 μm, 1000 μm, 1400 μm, and 2000 μm (2 mm), respectively, in the four images taken at 0, 6, 18, and 91 s. The advancing of the liquid front ahead of the particles indicates that there is "differential drainage" in the thin film: the film-averaged velocity of the particles is smaller than that of the liquid in the direction of spread. This differential drainage is discussed in connection with a proposed mechanistic basis for the onset of the banding segregation in the following section.

3.4 Discussion

Particle segregation in the Couette device is caused by repeated exposure of the suspension to a free surface. Our examination of this phenomenon has focused upon the role of fill fraction and angle of inclination, as we have sought to explore the behavior under conditions previously unstudied. Introduction of inclination breaks a basic symmetry of the system relative to prior studies, and the dynamics at finite inclination include a highly regular down-axis motion of evenly-spaced bands. The observation of this regular motion of long-lived bands prompted consideration of the general characteristics of the band motions, and the bands have been shown to undergo sustained fluctuational motion in the horizontal device.

Such fluctuational motions of the concentrated bands have not been described previously, and this may be related to the geometry of the Couette device used. The device used for this work was a wide-gap Couette of radius ratio $R_i/R_o = 0.29$, and while we find qualitative behavior similar to that found [17] at $R_i/R_o = 0.64$, the bands formed have a different appearance at small fill fractions, being narrow, directly adjacent to the inner cylinder rather than spanning the annulus, and separated by regions only slightly diluted relative to the mean ϕ of the suspension in the device of

smaller R_i/R_o. Because of the small ratio of R_i/R_o, there was no bridging of the gap by suspension over the inner cylinder as seen in prior work in this geometry, leaving the free surface relatively undisturbed by the outer wall. Of most significance from our perspective, the use of the smaller R_i/R_o allowed examination of the flow for a range of values of the fill fraction both above and below the value of f which provides complete coverage of the inner cylinder, specifically $f_c = 0.65$ in the stationary device used in this work.

The summary observation is that f_c separates two regimes of behavior; the change from low fill fraction behavior to high fill fraction behavior is centered very near $f = 0.65$ at $\alpha = 0$ under our standard conditions ($\phi_{\text{bulk}} = 0.2$ and driving rate of 8 RPM). While this may change with rotation rate, ϕ_{bulk}, and fluid properties, the primary influence appears to be related to the thickness of the "film" of suspension covering the inner cylinder. At $f < f_c$, this film is generated by the cylinder carrying the suspension over to the opposite side of the device and thus drainage competes with the driving rotation to establish a film thickness. This thickness is generally thinner than the film depth generated in the case when $f > f_c$. There appears to be a lower limit to the film thickness for which the banding occurs due to flows on the inner cylinder; very slow rotation rates at $f < f_c$ result in a very thin film and banding occurs in the entire radial extent of the annular region rather than on the rotating cylinder.

The flow is also influenced by fill fraction: for $f < f_c$ the fluid is forced to return predominantly under the cylinder rather than flowing over the driving cylinder. This flow effect and its coupling to the particle fraction certainly warrants further study, as this flow has has been shown to be a factor in the centrifugal instability leading to recirculation eddies and pattern formation of pure liquids in the partially-filled Couette geometry [40, 41]. However, our studies are at vanishing inertia and the

results obtained for varying f and α have shown that banding occurs for a range of base state flows in the cylinder. Hence, we do not believe the banding results from instability of the subsurface flow.

In regard to the cause of the banding, it has been suggested [19, 42, 43] that shear-induced migration is the mechanism leading to the segregations. A scaling analysis shows that for the migration distances in the Couette flow, which are comparable to the inner cylinder radius, the time required is $t \sim R_i^2/D_{\rm sh}$, where $D_{\rm sh} = \dot{\gamma} a^2 \mathcal{D}(\phi)$ is the shear-induced diffusivity and $\mathcal{D}(\phi)$ is a dimensionless function of particle fraction. Simulation and experiment have been performed to determine $\mathcal{D}$ and an upper estimate from experimental work [44] (smaller values are found in simulation [45]) for the component in the vorticity direction $\mathcal{D}_{zz}(\phi = 0.2) \approx 0.02$. The shear rate in the thin film is estimated as $\Delta\rho g h/\mu$. The particles are of maximum radius 150 μm and the film prior to banding is at most $h = 0.2$ cm in thickness for the eight RPM conditions, while the pure fluid viscosity is used (thereby overestimating the shear rate). We will use the full gravitational acceleration, and will assume the suspension is subjected to driving shear rate at all times; both choices overestimate the rate of migration, as the film is vertical only at isolated points, and the suspension is in the film only about half of each rotation. With these numbers, we find that $t \sim 6 \times 10^4$ s, or almost 17 hours, during which time the cylinder would undergo roughly 8,000 rotations at $\omega = 8$ RPM. Development of bands occurs in about 200 rotations in most cases for $f < f_c$ (see Table 1), a factor 40 times more rapidly than predicted by shear-induced migration. We further note that migration is observed in a suspension of $\phi_{\rm bulk} = 0.01$ after several hours of shearing (at 8 RPM) in the Couette at $f = 0.5$, and the procedure above yields an estimate for shear-induced migration on the order of several hundred hours, an estimate too large by two orders of magnitude. Hence, there is strong evidence against shear-induced migration as the mechanism

responsible for the observed segregation.

Experimental results from this work suggest that the minimum film depth is a controlling factor in the rate and structure of the observed banding. For fill fractions $f < 0.65$ in which the film is thin at the driving rates of this study, about ten narrow bands of elevated ϕ are formed within 200 rotations of the inner cylinder, with the intervening regions only slightly diluted relative to ϕ_{bulk}. The bands formed at these low fill fractions are mobile, and their positions fluctuate, leading to coalescence and vanishing at the axial endcaps at zero inclination, $\alpha = 0$. For small values of α, the band formation rate and migration speed are observed to be regular. As the fill fraction increases beyond $f_c = 0.65$, the timescale, or number of rotations of the driving cylinder, required for banding increases rapidly. From less than 200 rotations to establish bands at a characteristic low fill fraction of $f = 0.50$, the number increases to about 4000 at $f = 0.71$, and to at least 25,000 rotations at $f = 0.90$. At large f, the concentrated bands become wider and the dilute regions, as seen in Figure 3.6 (c), tend toward $\phi = 0$. The behavior for $f > 0.90$ remains unknown. An experiment at a fill fraction of $f = 0.95$ was driven at 25 RPM in hopes of reducing the required experimental duration, but was stopped when no observable effects had been observed after 75,000 rotations.

The mechanistic basis which appears most plausible for the earliest stages, or onset, of axial segregation to concentrated bands is differential rates of drainage of particles and fluid by gravity-driven flows when a fluctuation in surface elevation occurs. We interpret this argument to be consistent with the discussion of banding segregation in the partially-filled single cylinder presented by Tirumkudulu et al. [16]. In that study, the particle size relative to the film thickness in the drainage flow down the cylinder wall was noted to be a controlling factor in the degree of segregation. The central idea upon which the mechanism rests is that gravity-driven

flow in a thin film of suspension over a solid surface will discriminate between the solid and liquid phases, *i.e.* the fluid and particle phase film-averaged velocities will differ. Results of the drop spreading experiments described in §3.3.3 support this argument. If we consider fluctuations of the free surface of a Couette flow along the cylinder z-axis of form $\delta h = \epsilon \cdot cos(z/\lambda)$ in a suspension of uniform ϕ, the more rapid fluid drainage would result in a slight elevation of the local ϕ at the crests of the fluctuation. Such a mechanism is self-propagating in that the increase in ϕ will lead to an increase in the local effective viscosity of the suspension at this position, which will cause the free surface to be elevated as the fluctuation passes through the surface again on the next rotation (the increase in effective viscosity decreases the value of G, and gravity effects are weakened relative to viscous flow). The primary factors which cause "differential drainage" of the phases appear to be the following: (a) the layer of material directly adjacent to the free surface is liquid if the particles are wetted, and has the largest gravity-driven velocity, and (b) the motion of a particle within a thin film will be hindered by the presence of the solid (and to a lesser degree the free) surface. Both factors will result in fluid flowing ahead of the particles in an experiment such as the drop-spreading tests described in §3.3.3. Both factors also have relatively less influence at film depths which are many times the particle size. For this reason, the segregation is expected to be most rapid in regions of small film depth, and under limited testing we find this expectation holds. As noted in §3.3.3, at $f = 0.75$ and small inclination, banding occurs rapidly in the elevated end of the Couette where the film is shallow, while the bands appeared much later in sections of the Couette at greater depth over the inner cylinder.

The arguments above are only intended to hold for the onset of the segregation. The subsequent evolution of the band structure involves secondary flows owing to the complex structure of the particle fraction field, which in recent work by Thomas

et al. [42] on the single cylinder banding segregation has been shown to exhibit a "triplet" band structure where an individual concentrated band is made up of a central and two side bands. While this structure is not seen in the Couette flow, the flow becomes three-dimensional when the particle concentration varies axially, and in our experiments we have observed—after the banding is well-developed—pronounced extensional flows which pull suspension into the bands on the upflow side of the driving cylinder. Further study is planned to describe the full three dimensional flow.

CHAPTER IV

FILM DEPTH AND CONCENTRATION BANDING IN FREE-SURFACE COUETTE FLOW OF A SUSPENSION

4.1 Introduction

This work[1] considers phenomena observed in the free-surface flow of a suspension. Suspension flow with a free surface occurs in the coating of paper with kaolin suspension to obtain a glossy surface [46], as well as in the very different application of bioreactors [33]; in the latter case, the suspended materials include cells and the continuous flow adjacent to the free surface provides oxygen for the growth and/or replication process in a low-shear environment. There are a range of conditions in the various applications and thus there is motivation to develop fundamental understanding of the behavior of a suspension at a free surface in order to facilitate engineering design.

The presence of a free surface for a liquid flow adjacent to gas is well-known to

[1]This chapter appeared as "Film depth and concentration banding in free-surface Couette flow of a suspension" by Brian D. Timberlake and Jeffrey F. Morris in Philosophical Transactions of the Royal Society of London A. (2003) **361**,895-910

be associated with the Kelvin-Helmholtz and Rayleigh instabilities [47], water waves [48], and numerous other phenomena. In the case of a suspension flow with a free surface, similar phenomena clearly remain possible, but particle interaction with the free surface also introduces the possibility for instabilities involving the concentration of suspended solids. The point to be taken from this is that the instabilities may affect not only the interface shape, but also induce changes in the material properties which depend upon the concentration. The interest here is in such instabilities which have been observed in rotating flows of free-surface suspensions. Specifically, we are interested in a phenomenon observed in the geometries of partially-filled concentric cylinders with the inner cylinder driving the flow [17, 18] and a partially-filled single rotating cylinder [19, 16]; in each geometry, an axial segregation of particles into bands alternately rich and dilute in particles has been reported. This variation of the local particle volume fraction, ϕ, gives rise to an axially-varying effective viscosity of the suspension, $\eta_s(\phi)$, after the instability is established. The present work examines the Couette geometry, schematically illustrated in Figure 4.1, considering a particle volume fraction of $\phi = 0.2$ in all experiments described, while varying other system parameters.

The film formed over the inner cylinder under flow (or present without flow, at sufficiently large filled fractions of the annulus) has been, both by the present authors [18] and others [16], suggested to play a role in the segregation. Consequently, we focus in this work upon providing measurements of film thickness, and relating this thickness to other features such as the band formation time in the concentric-cylinder free-surface flow. Our results show that the film thickness indeed plays a quantifiable role in the band formation process, but that role is not one which can be stated independent of other variables, including the inclination and rotation rate. Beyond providing the first quantitative results on the film thickness and its correlation to

banding time, we also present results which show that the film evolves with time prior to banding The experimental techniques and results are presented in §4.2.

The banding phenomenon in the Couette device involves a complex flow influenced by many parameters, and appears to require repeated exposure to the free surface. This latter feature leads to the need for the cyclic flows in which it has appeared, and we have yet to find a simpler flow geometry in which banding occurs. We have, however, developed a physically-based model requiring phenomenological input to describe the concentration evolution in thin films which we feel captures features of the initial stages of the segregation process. The mechanistic basis of this model was described previously in Chapter 3, and relates the onset of segregation to fluctuations in the surface elevation; these fluctuations are presumably driven by fluctuations in viscosity through the variation of particle fraction or perhaps, at sufficiently small ϕ, temperature. The concept underlying the mechanism is that there is a deviation in velocity between the phases in gravity-driven flow caused by the fluctuations in surface elevation. The deviation in phase velocities was demonstrated for the spreading of a drop of suspension in Chapter 3. This difference in velocities we have termed a "differential drainage" flow. The model, described in §4.3, gives rise to a set of coupled equations for volume fraction, axial velocity, and variation of the film depth. We summarize the work in §4.4.

4.2 Experiments

4.2.1 Apparatus, materials and methods

Experiments were performed in concentric cylinder, or Couette, devices shown schematically in side and end views in Figure 4.1. The devices consist of two concentric cylinders. The outer cylinder is a tube of Lexan (polycarbonate plastic), and the solid interior cylinder is stainless steel. The annulus is closed at each end by Lexan caps

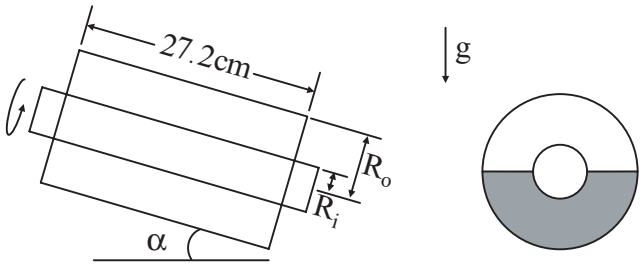

Figure 4.1: Schematic in side and end views of the Couette device. The inner cylinder is stainless steel and has radius $R_i = 0.64$ cm, $R_i = 0.95$ cm, or $R_i = 1.27$ cm, while the outer Lexan cylinder has inner radius $R_o = 2.22$ cm, and the annulus has length $L = 27.20$ cm. All experiments use a volume fraction of $\phi = 0.2$.

into which a sealed bearing is mounted, allowing the inner cylinder to turn while the outer cylinder is stationary. The cylinder motion is driven by a 1/4 horsepower feedback controlled electric motor (Dayton, model 1L497); rotation speed was accurate to ± 0.007 rotations per minute (RPM). The device can be mounted horizontally (axis perpendicular to gravity) or in an inclined position; as seen in Figure 4.1, this inclination is defined by the angle, α, which the cylinder axis makes with the horizontal.

The radii of the solid inner cylinders used for this study were $R_i = 0.64$, 0.95, and 1.27 cm, while the outer cylinder has inner radius $R_o = 2.22$ cm, and the annulus has length $L = 27.20$ cm. The majority of experiments in this work were performed using $R_i = 0.64$ cm, for which $R_i/R_o = 0.29$; this quantity varies from 0.29 to 0.58 in our studies (prior work by Tirumkudulu *et al.* [17] was performed at $R_i/R_o = 0.64$). The fill fraction occupied by the suspension is given by $f = V_{susp}/\pi(R_o^2 - R_i^2)L$; the volume of suspension, V_{susp}, in the annulus was determined from the known suspension density and the measured mass of suspension placed into the device.

Spherical poly-(methyl methacrylate) (PMMA; ICI Acrylics) particles were sieved to diameters in the range $2a = 250$–300 μm where we introduce a for the radius. A group of experiments was performed with particles of maximum diameter 106 μm.

The suspending fluid was a mixture of 76% Triton X-100 (a surfactant; Union Carbide), 16.2% zinc chloride ($ZnCl_2$), and 7.8% water, with the percentages based on mass. This mixture was density-matched ($\rho = 1.180$ g/cm^3) and roughly refractive index (RI)-matched to the PMMA particles (RI = 1.491 at $T = 20^oC$). This suspending liquid mixture had a viscosity of $\eta_0 = 160$ Poise at $T = 23^oC$. A particle volume fraction of $\phi = 0.2$ was used in all of the experiments described in this work.

The rotation rate was varied from $\omega = 2$–16 RPM in this work. The bulk scale Reynolds number under the largest rotation rate was much less than unity, and thus inertia is negligible.

4.2.1.1 Film thickness and interface shape

The film thickness under flow was determined by video imaging. For most of the experiments, this was performed by mounting the camera on the same horizontal plane as that containing the film surface, and orienting the camera with its focal axis perpendicular to the axis of the cylinder. The distance per pixel was determined by observing an object of known size before beginning the experiment. The film thickness was calculated by determining the number of pixels between the surface in the current picture and the inner cylinder at the beginning of the experiment. We report instantaneous film depths for purposes of visualization of the structure of bands. However, for the film depths characteristic of a given condition, the measured film depth was averaged over one or more cycles of the cylinder rotation to eliminate the influence of slight asymmetries apparent even in the absence of the suspension; these result from imperfections in the device including slight noncircularity of the inner cylinder.

The interface shape has also been investigated. For this study, a laser light sheet was projected onto the free surface perpendicular to the cylinder axis and the position

from which the light was reflected was recorded by a CCD camera looking along the axis. From this, the interface of the air-suspension interface was determined as a function of position for different rotation rates. The location on the interface of a stagnation point is also readily found from observation of a sequence of these images and the stagnation points are reported along with the interface shape.

4.2.2 Results

As in prior work with suspensions in free-surface Couette flow we observe the formation of particle-rich bands separated in the axial direction by regions which are relatively dilute in particles. We have observed several features of the film thickness over the inner cylinder, a quantity of particular interest to the band formation process, which have not previously been reported. The bulk of the results here represent quantified visualization information, but we also present results of the band formation time for roughly a decade of rotation rates (ω = 2–16 RPM) for the smaller inner cylinder. The film thickness prior to and immediately after bands form is reported, as are limited results on the interface shape as a function of rotation rate.

The shape of the free surface over the inner cylinder was determined using a laser light sheet, and can be seen in Figure 4.2. For sufficiently low fill fraction, a stagnation point is observed on the free surface. It is not currently known for what large value of f this stagnation point ceases to exist. Writing the distance from the cylinder axis in the horizontal plane as r and the elevation from this plane as y (both reported in cm), the stagnation point for $f = 0.51$ occurs at $(r, y) = (1.02, 0.06)$ for $\omega = 4$ RPM and at $(r, y) = (1.34, 0.11)$ for $\omega = 16$ RPM; both points are identified in Figure 4.2. This information was determined by visual inspection of the video of the laser sheet over the free surface. In the video there is a point on the surface from which all particles are observed to move away, and this is identified as a point on the

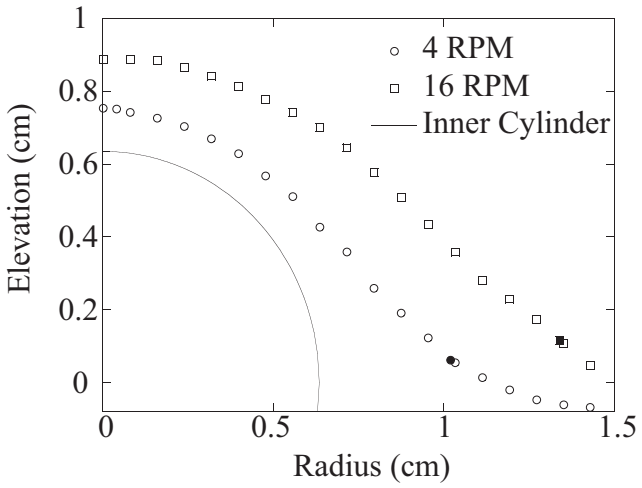

Figure 4.2: Elevation of the free surface prior to onset of band formation, at $f = 0.50$, $\phi = 0.2$, and $\omega = 4$ RPM and 16 RPM. Rotation of the inner cylinder is counter-clockwise in this view. The stagnation points are marked by a solid circle for $\omega = 4$ RPM and by a solid square for $\omega = 16$ RPM.

stagnation line traversing the length of the device. The stagnation line exists because there is a reverse flow in the suspension: the stagnation line divides material which flows over the inner cylinder from that which follows the reverse flow. Apparently there is insufficient flow over the inner cylinder and thus the added elevation on the "upflow" side of the cylinder drives a reverse flow (opposite in sense to the driving cylinder motion) near the outer cylinder. The reverse flow in a partially-filled Couette at finite Reynolds number was considered by Normand, Mutabazi and Wesfried [41]. Bands are observed to form initially in the elevated region on the upflow side of the inner cylinder, lying to the right in Figure 4.2, slightly closer to the cylinder than the stagnation point.

Bands form first next to the end caps and soon thereafter are observed throughout the device. The measured film depth along the uppermost surface of the inner cylinder adjacent to the elevated end cap is shown for $\alpha = 2.0^o$ and three values of ω in Figure

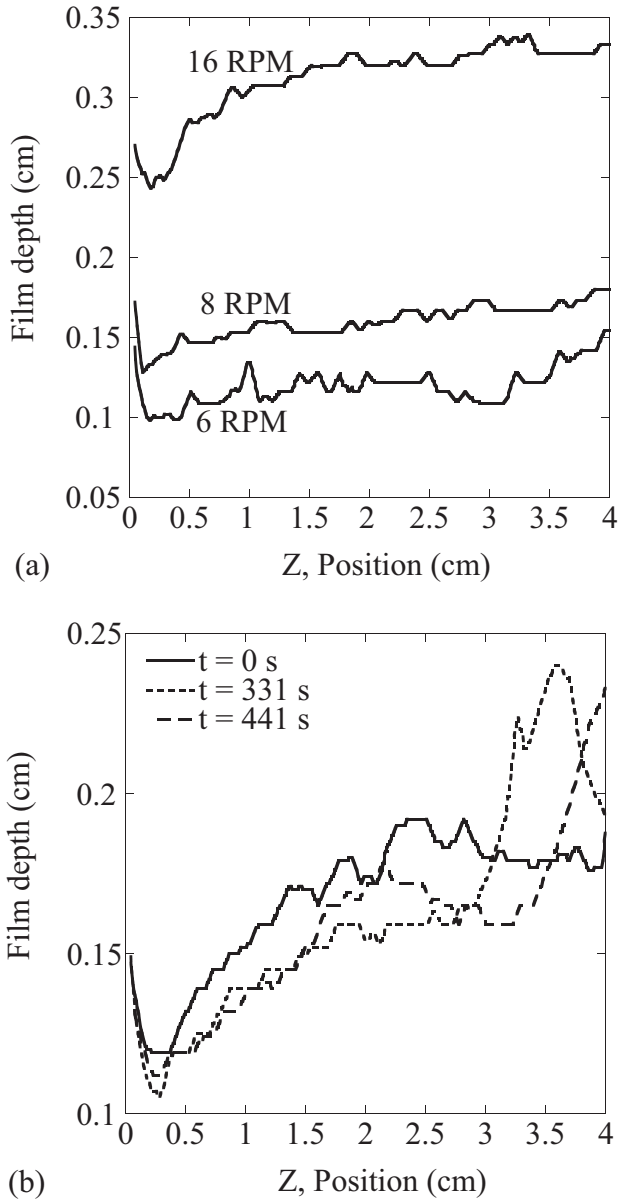

Figure 4.3: Instantaneous film depths over the uppermost surface of the inner cylinder in an inclined condition, with $Z = 0$ representing the position of the end cap at the elevated end of the device: (a) immediately after flow begins for $\alpha = 2^o$, $f = 0.5$, $\phi = 0.2$, and varying ω; and (b) as a function of time for $\alpha = 2^o$, $f = 0.5$, and $\omega = 8$ RPM. Time in (b) is measured from the first sign of a band rather than the time from when the inner cylinder was set in motion. In this view the top of the inner cylinder is rotating away from the viewer.

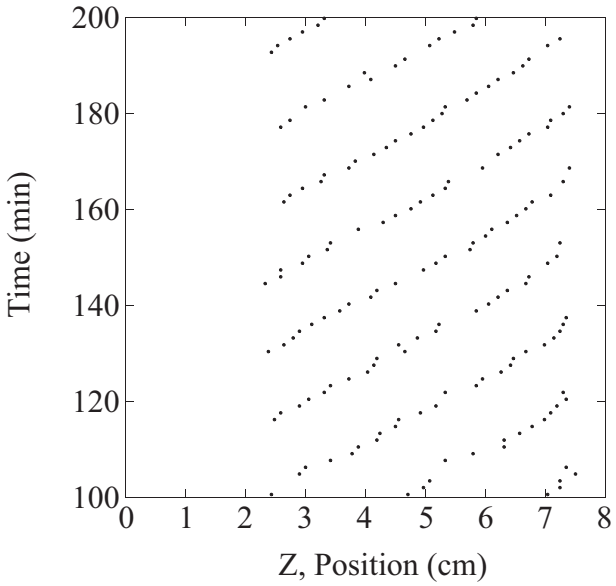

Figure 4.4: Diagram showing band locations for the conditions $\phi = 0.2$, $\omega = 8$ RPM, and $f = 0.5$ identified by the method described in Chapter 3. The axial position from the endcap of the device at the elevated end is given by Z and time is measured from commencement of the flow. Note the nearly periodic appearance of bands at $Z \approx 2.5$ cm.

4.3 (a), and we note that it has negative curvature, a point we shall consider in §4.3. In the inclined operation, it is in this region where the interface is curved due to interaction with the endcap that initial band formation occurs. The formation occurs regularly in this case between the end cap and a down-axis location where the film thickness reaches its uninfluenced center value. This location is at $Z \approx 3.0$ cm for all rotation rates investigated.

The film thickness as a band grows, while the device is inclined, can be seen in Figure 4.3 (b). In this case, a band begins to form at $Z = 2.5$ cm, at a time arbitrarily denoted $t = 0$, and begins to migrate down axis due to the inclination of the device. At $t \approx 440$ s, the band has migrated to a location more than 4 cm from the endcap. Once the band has migrated sufficiently down axis, a new band forms at about the same position, and migrates in the same manner; this process is repeated indefinitely. The process is visualized in Figure 4.4, which presents a diagram of the positions of bands with respect to time and axial position. The method used to obtain this information in automated fashion from the video is outlined in Chapter 3.

When the device is not inclined, bands form without a directed migration. The film thickness as a band grows, with $\omega = 12$ RPM, $\alpha = 0$ and $f = 0.51$, is illustrated in Figure 4.5. From the time the band is first visually observable, approximately 100 seconds pass before the band reaches its final height.

The mean film thickness is found to grow monotonically until bands form, as illustrated for four rotation rates in Figure 4.6 (a). The variation occurs over many rotations of the driving cylinder, and thus is not a transient which can be explained by pure fluid behavior. This phenomenon thus raises a number of new possibilities for the banding phenomenon as it suggests that, prior to the banding, there is a radial segregation counter to particle migration in a full wide-gap Couette device [5, 6, 1]. We have yet to measure the spatial variation of ϕ, because the measurement of ϕ by the

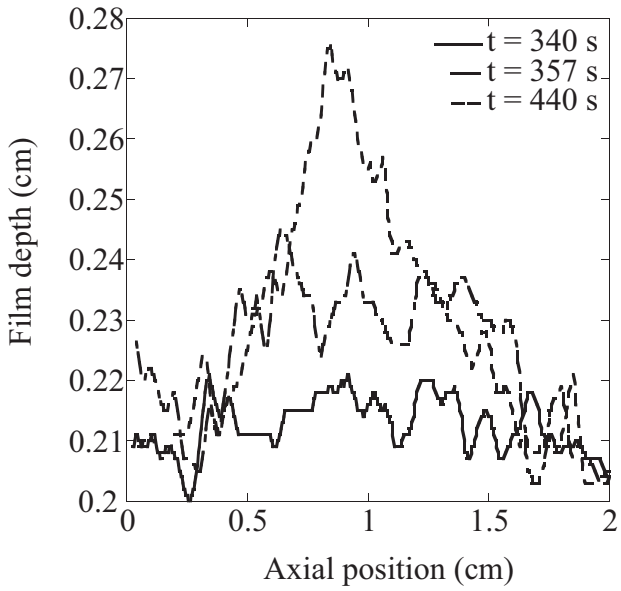

Figure 4.5: Film depth over the uppermost surface of the inner cylinder, as a band grows, for $\alpha = 0$, $\phi = 0.2$, $f = 0.51$, and $\omega = 12$ RPM. Time is measured from onset of motion of the inner cylinder.

direct sampling technique described in Chapter 3 does not have the spatial resolution needed. It is our conjecture that the distortion of the free surface as particles pass over the inner cylinder results in capillary force upon the particles, generating a net flux of particles toward the inner cylinder. This would cause a variation of the local particle fraction, with a larger ϕ and larger effective viscosity adjacent to the inner cylinder. Once bands begin to form, the mean film thickness decreases. It is not understood why this decrease takes place. The behavior of the film depth during onset of banding is also shown as the ratio of the maximum to mean film depth over the inner cylinder as a function of time in Figure 4.6 (b). Except for the smallest rotation rate included in this figure, $\omega = 4$ RPM, the depth ratio is essentially constant at a value between 1.0 and 1.1 before growing. At $\omega = 4$ RPM, the ratio decreases slowly to a minimum centered around 1.05 at which it remains for a period before the growth characteristic

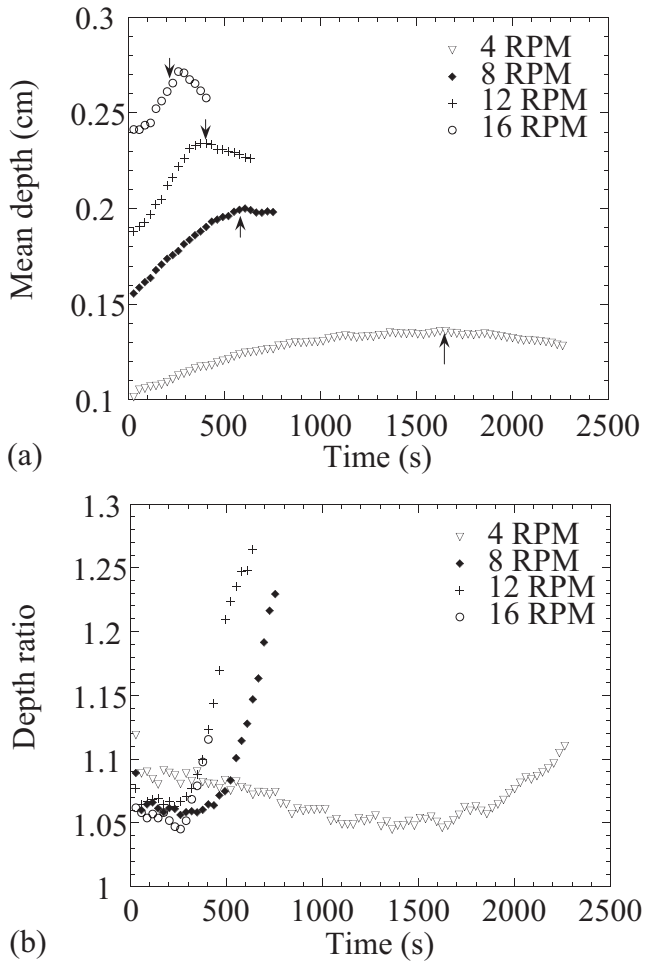

Figure 4.6: (a) Mean film depth and (b) ratio of maximum to mean film depth over the uppermost surface of the inner cylinder. These results are for $\alpha = 0$, $\phi = 0.2$, and $f = 0.51$. A time of zero here indicates the time the inner cylinder was set in motion. In (a), arrows denote the time of initial observation of concentration bands.

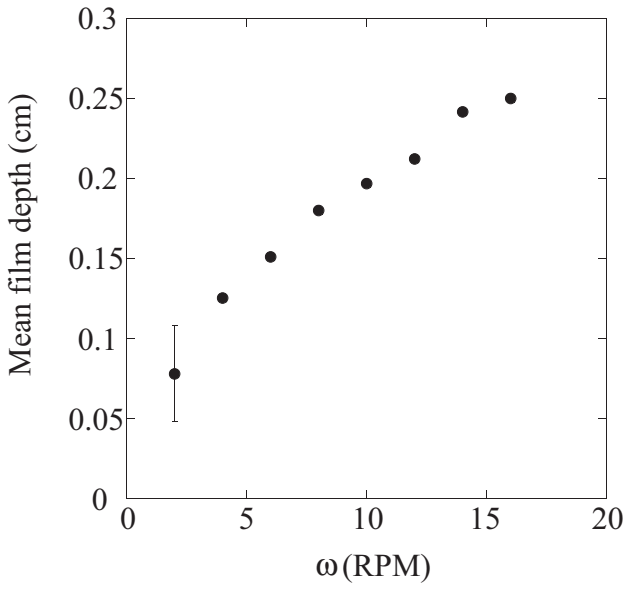

Figure 4.7: Film depth over the top of the inner cylinder for $f = 0.51$, $\phi = 0.2$, and $\alpha = 0$, averaged over the entire period prior to onset of banding. The error bar is applicable to all points.

of banding occurs. The film thickness averaged over the entire time prior to band formation increases with increasing rotation rate, as seen in Figure 4.7.

The time until visual detection of band formation in the horizontal device has been determined at different rotation rates for $f = 0.51$. Under these conditions, bands appear sooner for higher rotation rates. Data have been taken for $\omega = 2$–16 RPM for particles of 250–300 μm diameter, and for $\omega = 4$–12 RPM for a suspension made up of particles of diameter less than 106 μm, with the results presented in Figure 4.8. Considering first the larger particles, a noteworthy change in the formation time is seen between a rotation rate of 2 RPM, for which bands took 38,500 seconds to appear (note that this point is excluded from the data plotted in the figure), and 4 RPM where bands required 1600 seconds to form. A similar large increase in the time to band formation as ω is decreased was reported in Chapter 3, although there

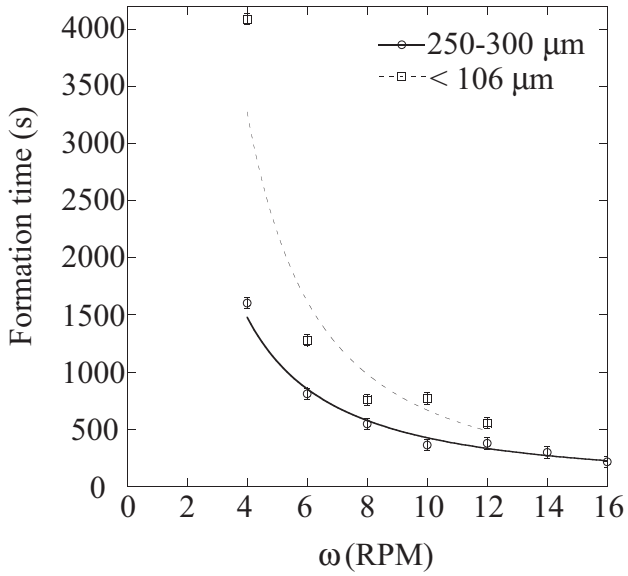

Figure 4.8: Time required for bands to form at $f = 0.51$, and $\alpha = 0$, for $\phi = 0.2$ and two particle sizes, diameter 250–300 μm, and diameter less than 106 μm. For the larger particles, a data point for $\omega = 2$ RPM and formation time of 38,500 s has been excluded for visualization and fitting purposes. Power-law fits shown are $t = 9740\omega^{-1.38}$ and $t = 36400\omega^{-1.74}$ for the large and small particles, respectively.

it was determined that the time to band formation for $\omega = 4$ RPM was 480 minutes, much longer than the 1600 seconds found here. The discrepancy is due, we believe, to unreliable rotation rate at the smallest accesible ω in the prior work (Chapter 3), as a result of use of a motor with substantial internal resistance leading to periods of nearly stalled motion. This behavior prompted use of a motor in the present work, which, as noted above, was accurate to less than one percent of an RPM even at the lowest rate reported of $\omega = 2$ RPM. The bands which form with $\omega = 2$ RPM are not raised out of the surface as they are for all other rotation rates investigated under these conditions. For the smaller particles, the bands were less visible and showed a less pronounced elevation above the remainder of the surface. For these smaller particles, the formation time is longer at each rotation rate. The relationship between rotation rate and band formation time plotted in Figure 4.8 has been fitted to a power law for each size of particle: formation time scales roughly as $\omega^{-1.38}$ and $\omega^{-1.73}$ for the large and small particles, respectively. We note the appearance of a local maximum in each set of data, which suggests that a single power law does not hold well for this dependence.

The number of observed bands is found to decrease weakly with increasing rotation rate in this work, over the entire range $\omega > 4$ RPM. In our prior work (Chapter 3), the same general trend was observed except that a smaller number of bands were observed for $\omega = 4$ RPM than for the larger rates. Results from both sets of experiments at $R_i/R_o = 0.29$, $f \doteq 0.5$, and $\phi = 0.2$ are presented in Table 4.1. It is clear that we have a narrower range in number of bands at most rates than was observed in our prior work. The most plausible explanation for the difference lies in the variability of ω in our prior work where the flow was driven by a motor without feedback in its speed control; as the drive from that motor to the cylinder was belt-driven, a further possible source of error lies in slip of the belt. The new results reported here are

Table 4.1: The number of bands observed in the uninclined Couette at $R_i/R_o = 0.29$, $f = 0.51$ in the present paper and $f = 0.50$ in Chapter 3, and $\phi = 0.2$. The particles are of diameter 250-300 μm. The present experiments were performed with a motor having better accuracy in ω than in the work described in Chapter 3.

Rotation rate, ω (RPM)	Number of bands, present work	Number of bands, (Chapter 3)
4	12	7
6	11–12	12
8	10–11	8–11
10	8–9	—
12	8–10	9–12
14	8–9	—
16	9	9–12
24	—	8-10
32	—	9–11

believed to be a more accurate representation of the state of the system at the given conditions. It is not completely clear why variation of ω would lead to variation in the number of bands, and this may be of interest for further study of the dynamics of this phenomenon.

Mixing experiments have been performed with a region of the inclined device ($\alpha > 0$) initially filled exclusively with dyed particles and the remainder with the undyed particles. The goal of the experiments was to elucidate the exchange of particles from the bands to the "bath" of fluid lying below the inner cylinder. Images from these experiments can be seen in Figure 4.9, at conditions of $R_i = 0.64$ cm ($R_i/R_o = 0.29$), $f = 0.5$, and $\alpha = 2^o$. The region of dyed particles consisted of one fourth of the total suspension and was placed at the raised or lowered end of the device. From these experiments it is clear that particles travel with the bands as they migrate; mixing of the particles visually identifiable as a band with the surrounding suspension occurs only over significant migration distance. The repeated formation

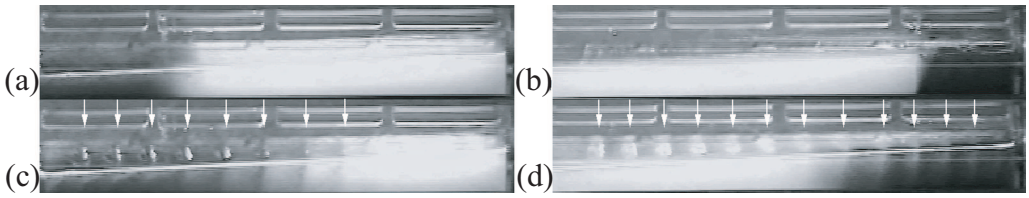

Figure 4.9: Images from mixing experiments with $R_i = 0.64$ cm, $f = 0.5$, $\phi = 0.2$, and $\alpha = 2^o$. (a) Initial image with dyed particles in the elevated end of the device. (b) Initial image with dyed particles in the lowered end of the device. (c) Image from case (a) after bands of dyed particles begin migration. (d) Image from case (b) after banding of nondyed particles begin migration. The white arrows in (c) and (d) indicate the positions of the bands.

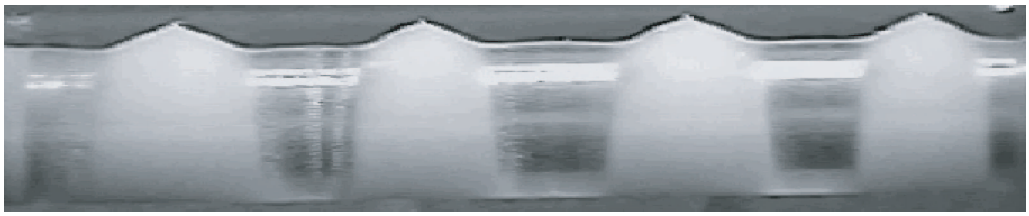

Figure 4.10: Complete segregation of particles and fluid for $R_i = 1.27$ cm, $f = 0.8$, $\phi = 0.2$, and $\omega = 12$ RPM.

of bands and down-axis transport of particles through their migration is balanced by a return flow of suspension along the bottom of the device.

Limited experiments have been performed at $R_i = 0.95$ cm and $R_i = 127$ cm ($R_i/R_o = 0.43$ and 0.58, respectively), with the goal of determining the transition from the behavior observed in Chapter 3, with very mobile particle bands, to that of Tirumkudulu *et al.* [17] where bands bridged the annulus at $R_i/R_o = 0.64$. Bands that form using these larger inner cylinders indeed exhibit less freedom of motion without inclination, and to date we have performed no experiments at inclination ($\alpha > 0$) for these larger inner cylinders. One of the most striking results obtained using the larger cylinders is that, at elevated fill fractions it is possible to cause extreme and quite rapid segregation of the particles, as seen in Figure 4.10 for $\omega = 12$

RPM, $f = 0.8$ and $R_i/R_o = 0.58$. The state illustrated was attained, beginning from a uniformly distributed state, in about 20 minutes, or under 250 rotations.

4.3 Model: suspension film drainage

It has been suggested in prior work [19, 42] that the mechanism leading to the onset of banding is one involving shear-induced migration. This does not appear to be the case because band formation occurs in very dilute suspensions ($\phi \geq 0.01$ in our experiments, with smaller ϕ not necessarily non-banding but unstudied). Furthermore, as described in Chapter 3, the onset of band formation occurs on a time scale too short to be a result of shear-induced migration.

Repeated observation of the Couette device leads us to a different view of the onset of banding. The basic concepts were outlined in Chapter 3, where the presence of a deviation between the mean velocities of the solid and liquid components of the suspension was demonstrated to occur in a simple flow. Specifically, we considered the drainage flow of a pool of suspension created by placing a droplet of suspension on a planar surface previously wetted by a thin film of the suspending liquid. In this flow, the liquid from the suspension pool is found to drain more rapidly than the particles, creating a front which advances ahead of the particle front. Arguments were presented to suggest the manner in which this "differential drainage" could give rise to the initial stages of the observed banding; later stages involve convection of particles by complex three-dimensional flow fields and the arguments are not expected to have validity when these flows are present.

Here, we formulate differential drainage mathematically to demonstrate its impact on the particle fraction in drainage of a suspension film. The result is a model for the film-averaged particle fraction, $\tilde{\phi}$, coupled to the equations for both the bulk velocity and the film thickness. The consequences are probed through examination

of properties of the equation rather than solutions for $\tilde{\phi}$.

The particle conservation equation on a pointwise basis may be written

$$\frac{\partial \phi}{\partial t} + \nabla \cdot (\phi \boldsymbol{U}_p) = 0, \tag{4.1}$$

with $\boldsymbol{U}_p$ the mean particle-phase velocity. We consider here only suspension flows with a free surface, and wish to average the equation over a depth. For concreteness, we will first consider a suspension film draining on a planar surface with motion constrained to a single direction, say x. The film interface is described by $z = h(x,t)$, and gravity is along the negative z axis. The film thickness varies such that $h(x,t) = h_o + \delta h(x,t)$ in which h_o is the mean depth. We make the "long wavelength" assumption that variations in the film thickness occur on lengthscales l, with $l \gg \delta h$. It is simplest to determine the particle conservation equation by recognizing that the particle volume is conserved and thus we may immediately write, for the unidirectional motion of interest,

$$\frac{\partial P}{\partial t} + \frac{\partial (P \tilde{U}_p)}{\partial x} = 0, \tag{4.2}$$

where

$$P(x,t) = \int_0^h \phi(x,z,t) dz,$$

and $\tilde{U}_p$ is the film-averaged particle velocity in the x direction. The film-averaged particle fraction is $\tilde{\phi} = P/h$. The conservation of mass for the bulk material provides the well-known equation (Whitham 1974) for the variation of h:

$$\frac{\partial h}{\partial t} + \frac{\partial (h \tilde{U})}{\partial x} = 0, \tag{4.3}$$

with $\tilde{U}$ the *bulk suspension* film-averaged velocity in x. We assume that the particle and suspension average velocities are related through $\tilde{U}_p = \beta \tilde{U}$, where $0 < \beta(2a/h) \leq 1$ is a "hindrance function" which represents the influence of the confining geometry of a film with solid lower boundary upon particle motion. Basic hydrodynamic theory for

neutrally buoyant particles indicates the limiting values of $\beta(0) \to 1$, and $\beta(1) \ll 1$. The former condition indicates no hindrance, while $\beta(1) \ll 1$ is meant to imply substantial hindrance in films of the order of the particle size. It should be noted that a small nonzero β may be expected even for arguments greater than unity provided there remains a substantial wetting film over the particle surfaces directly adjacent to the free surface.

The equation (4.2) may be reexpressed in terms of $P/h = \tilde{\phi}$ by multiplying by h^{-1} and performing appropriate manipulations to obtain

$$\frac{\partial \tilde{\phi}}{\partial t} + \frac{\partial}{\partial x}\left(\beta \tilde{\phi} \tilde{U}\right) = -\frac{\tilde{\phi}}{h}\left(\frac{\partial h}{\partial t} + \beta \tilde{U} \frac{\partial h}{\partial x}\right), \tag{4.4}$$

which may be combined with (4.3) to yield

$$\frac{\partial \tilde{\phi}}{\partial t} + \beta \tilde{U} \frac{\partial \tilde{\phi}}{\partial x} = \frac{\tilde{\phi}}{h} \frac{\partial}{\partial x}\left[(1-\beta)\tilde{U} h\right] \tag{4.5}$$

which is the model equation we seek. To obtain detailed predictions, this equation must be solved together with the x-momentum equation for the bulk suspension and (4.3) for the film depth. The use of the suspension-averaged velocity, $\tilde{U}$, and β is preferred over a form containing $\tilde{U}_p$ because it allows for simple interpretation of the expected behavior in the dilute limit, where $\tilde{U}$ may be assumed to be well-approximated by the pure fluid velocity. For use as an evolution equation it is also preferred, because h is related directly to $\tilde{U}$.

For purposes of interpretation of the initial stages of banding, we make several simplifications. Although in the actual flow variation in film depth may arise due to weak variations in $\tilde{\phi}$, here we simply assume a film depth of sinusoidal form, $h = h_o(1 + \epsilon \cos \lambda x)$ with $\epsilon \ll 1$, and study the consequences, assuming that $\nabla \tilde{\phi} = 0$ initially. For low-Reynolds-number flow,

$$\tilde{U} = -\frac{\rho g}{9 \eta_0 \eta_s} \frac{\partial h^3}{\partial x},$$

with $\eta_s(\phi)$ the suspension relative viscosity, which may be estimated as $\eta_s(\tilde{\phi})$. Replacing $\tilde{U}$ in (4.5) with this form, assuming $\beta < 1$ but of negligible variation, and expanding yields

$$\frac{\partial \tilde{\phi}}{\partial t} + \beta \tilde{U} \frac{\partial \tilde{\phi}}{\partial x} = -\frac{(1-\beta)\tilde{\phi}\rho g}{\eta_0 \eta_s} \left[h \left(\frac{\partial h}{\partial x} \right)^2 + \frac{h^2}{3} \frac{\partial^2 h}{\partial x^2} \right]. \tag{4.6}$$

Note that η_s is taken outside the differentiation because $\tilde{\phi}$ is constant.

If we consider the two points within a period of h where $\frac{\partial h}{\partial x} = 0$, namely at a crest and a trough, the equation at such points initially reduces to

$$\frac{\partial \tilde{\phi}}{\partial t} = -\frac{(1-\beta)\tilde{\phi}\rho g}{3\eta_0 \eta_s} h^2 \frac{\partial^2 h}{\partial x^2}, \tag{4.7}$$

implying that in the initial stages of flow when $\tilde{\phi}$ is essentially constant the curvature of the surface will drive concentration variations in the presence of differential drainage of the phases. Specifically, $\tilde{\phi}$ is predicted to increase at the crest, where the curvature is negative, and to decrease at the trough. Note also that for very deep films relative to the particle size, $\beta \to 1$, and the equation reduces to

$$\frac{\partial \tilde{\phi}}{\partial t} + \tilde{U} \frac{\partial \tilde{\phi}}{\partial x} = 0,$$

indicating that the particle fraction is predicted to be convected passively with the mean bulk flow.

A test of the model prediction is provided by considering its predictions for the suspension droplet studies described in Chapter 3, taking the flow to be unidirectional rather than the actual radial to match the above analysis. Here we assume the droplet immediately takes up a shape which is concave down with smooth variation of h but abrupt variation of $\tilde{\phi}$ at the edge of the droplet. For a droplet sufficiently small that the film depth satisfies $2a/h = O(1)$ so that $1 - \beta \neq 0$, the model predicts concentration will increase near the center of the drop where $\tilde{\phi}$ is governed by the

balance in (4.7), while $\tilde{\phi}$ will locally increase (from zero) in regions the particle front is entering and the dominant balance is

$$\frac{\partial \tilde{\phi}}{\partial t} = -\beta \tilde{U} \frac{\partial \tilde{\phi}}{\partial x}.$$

At points between these, it is necessary to solve the model for predictions.

In the Couette flow studied in this work, an increase in $\tilde{\phi}$ beneath a surface crest acts to amplify surface elevation at points elevated above the mean. Noting that $\eta_s'(\phi) > 0$, the increase in $\tilde{\phi}$ also yields a larger viscosity, which reduces the rate of drainage and thus yields a thicker film at the same position. This sequence of events will propagate the fluctuation in elevation. We have noted that the onset appears to occur first near the stagnation line and thus the appropriate place to apply the theory developed here is probably in this region.

4.4 Summary and concluding remarks

In this work, we have examined the suspension film flows generated in a free-surface Couette device and the relation of film properties to the banding phenomenon. Prior work in this geometry [17] and the related partially-filled single cylinder have shown that segregation to bands occurs, and in Chapter 3 the bands were shown under small R_i/R_o conditions to be highly mobile and long-lived. This work has added substantially to the quantitative knowledge base on the segregation to particle-rich bands by measuring film thickness as a function of various operational parameters, as well as measuring the band formation time.

The general characteristics of free-surface Couette flow elucidated by the work are several. The first is that the film thickness at small fill fractions increases with rotation rate, as expected. In both the inclined and horizontal cases, the band formation time decreases with the increased rotation rate. Note that this implies a more rapid band

formation as the film grows thicker. However, at large fill fraction, we have previously shown, in Chapter 3, that the band formation time undergoes an abrupt increase as f increases beyond a critical value, $f = f_c \doteq 0.65$ for $R_i/R_o = 0.29$; $f = 0.65$ is the minimum fill fraction for which there is a finite film depth over the inner cylinder prior to the onset of flow and the films for $f > f_c$ become progressively deeper. It can be concluded that the film thickness alone does not control the banding rate, and that surface deformation and rate of the drainage flow must also be considered.

A related point is that the flow for our smaller fill fractions of $f \approx 0.5$–0.6 exhibits a reversal zone, *i.e.*, a region of suspension which does not pass over the inner cylinder. This flow zone is separated from the flow which forms the film over the inner cylinder by a surface ending in a stagnation line along the free surface on the upflow side of the driving inner cylinder. It is in the vicinity of this stagnation line that the banding is first observed as elevated points on the "inner" side of the line, toward the driving cylinder.

There is potentially further relevance to the region of flow which does circulate around the driving cylinder. For $f \approx 0.5$ and $\alpha = 0$, we have measured the film thickness and shown that it slowly increases over many rotations prior to banding onset. Recalling that the flow is at low Reynolds number and should establish a fluid mechanical steady state rapidly, this implies that the local particle fraction undergoes a slow evolution in the plane perpendicular to the cylinder axis. Our best understanding at present is that the particles within the film cause a distortion of the interface, which generates a surface tension that in turn causes a net flux of particles toward the cylinder surface. This buildup results in a locally higher ϕ and higher effective viscosity directly adjacent to the cylinder, allowing for a thicker film.

In Chapter 3, particle bands were found to form very regularly at a position near the elevated end of the Couette, adjacent to the endcap. Measurement of the film

thickness on the upper surface of the inner cylinder in this region revealed an effect from the endcap, namely that the film thins over about three cm near the wall (with a small increase just at the wall). The interface is concave downward with respect to axial position (negative axial curvature), and it is in this curved region that the band first appears before beginning to migrate down-axis. It is unclear that the curvature at the upper surface is relevant, but a similar influence of the endcap may be at work near the stagnation line, where the bands are seen to arise in the uninclined case.

Further study to elucidate the role of surface curvature is needed, as the physically-based model for suspension film drainage presented in §4.3 suggests that such curvature in the presence of deviation in the mean velocities of particle and liquid phases can lead to segregation. Previously we have termed this phenomenon of a deviation in the velocities of the mixture components in gravity-driven flows "differential drainage" and we have presented a mathematical formulation of the concepts in this work. The influence of surface curvature is readily seen by examination of the model, but detailed predictions from solution of the model have not been obtained.

CHAPTER V

CONCLUSIONS

The work which has been presented here on free-surface suspension flows has relevance to industrial applications, including coating flows as well as flows in nature, such as mud and pyroclastic flows. This work has focused on coating flows and has presented experimental information as well as theoretical modeling of the flows investigated.

The inclined plane flow of a suspension has been studied both experimentally and theoretically. Stereoscopic PIV has been used to determine velocity profiles, and these velocity profiles have been further analyzed to make a coarse measurement of the particle concentration in the flow. Theoretical treatments and experiment both show that particles move away from the solid surface, and that the film thickness decreases as the suspension moves down the inclined plane, until it reaches some fully developed value.

We are not able to make conclusive statements about the particle concentration near the free surface. It appears that the easiest way to determine this will be by some sort of direct sampling. The unknown location of the free surface makes the use of most optical techniques difficult especially when trying to measure particle concentration very near this surface of unknown shape. It is also important to understand the correlation between the shape of the free surface and the position of the sub-surface

particles. This type of information can be used to determine if the free surface does indeed push the particles away. This would allow for the modeling of a more realistic boundary condition at the free surface. Based on the results of experiments and the modeling presented here, it is clear that the boundary condition at the free surface must depend on $\dot{\gamma}$ in the film and not just the shear rate next to the free surface. The migration of particles away from the solid surface is driven by the shear rate at the solid surface and since the free surface must push back against this migration to prevent the particles from leaving the film it must somehow be related to $\dot{\gamma}$ away from the free surface.

The free surface shape may be better determined by observing the reflection of an interference pattern from the surface. This would allow for the exact determination of surface normal vectors at certain locations, which potentially could be used to completely reconstruct the shape of the free surface, and subsequently to gain information about the force which the free surface places on the particles. This would allow for insight into the functional form of the relationship between $\dot{\gamma}$ and the normal stress jump at the free surface.

We have shown that under certain conditions repeated exposure to the free surface can cause instabilities in the particle concentration. The concentration banding phenomenon has been shown to occur under a variety of different fill fractions, bulk particle concentrations, inclination angles, ratio of inner to outer cylinder, and rotation rates of the inner cylinder. The dynamics of the concentration bands is strongly affected by the inclination angle and by the ratio of inner to outer cylinder. Inclination of the device breaks a basic symmetry and causes the band motion down the axis of the device to become very regular.

A model based on differential drainage has been proposed. This model explains how local disturbances in the height of the free surface can lead to an instability in

the particle concentration which grows into bands. The model also contains several terms which are similar to terms found in the Kuramoto-Sivashinsky equations which exhibit similar dynamics.

Coupling the model with the dynamics requires further investigation. A model which properly describes the dynamics of the concentration bands must also describe the band formation process in order to be complete. This is evident from the inclined experiments where concentration bands are observed to form and then migrate away, with another band forming in its place. The model we have proposed shows band formation and has components which are appropriate for a dynamical systems treatment of the system. The model has certain components which could result in the types of dynamical systems which have been found, however further work is required to determine if the model properly accounts for all phenomena or if it is lacking some component. Further effort must also be spent on characterizing the band dynamics under a wider variety of conditions.

APPENDIX A

CONCENTRATION BANDING PHENOMENON AND THE KURAMOTO-SIVASHINSKY EQUATION

There is a similarity between the dynamics seen in the concentration bands which form in free-surface Couette flow of a suspension and the dynamics which result from solving the Kuramoto-Sivashinsky equation. An example of this similarity can be seen in Chapter 1 and in Figure A.1, where the Kuramoto-Sivashinsky equation was solved by the method given in Trefethen [20]. If the model we have suggested for the band formation process is complete its solution should account for the dynamics found in the system. As given in Chapter 4 our model for the banding phenomenon is given as

$$\frac{\partial \tilde{\phi}}{\partial t} + \beta \tilde{U} \frac{\partial \tilde{\phi}}{\partial x} = -\frac{(1-\beta)\rho g \tilde{\phi}}{\eta_o \eta_s} \left[h \left(\frac{\partial h}{\partial x} \right)^2 + \frac{h^2}{3} \frac{\partial^2 h}{\partial x^2} \right] \tag{A.1}$$

We desire an equation of a single dependent variable and so we assume that the film thickness is proportional to the effective viscosity raised to some positive power. Relating the effective viscosity to the particle concentration yields the following:

$$h = A \left(1 - \frac{\tilde{\phi}}{\phi_{max}} \right)^{-a} \tag{A.2}$$

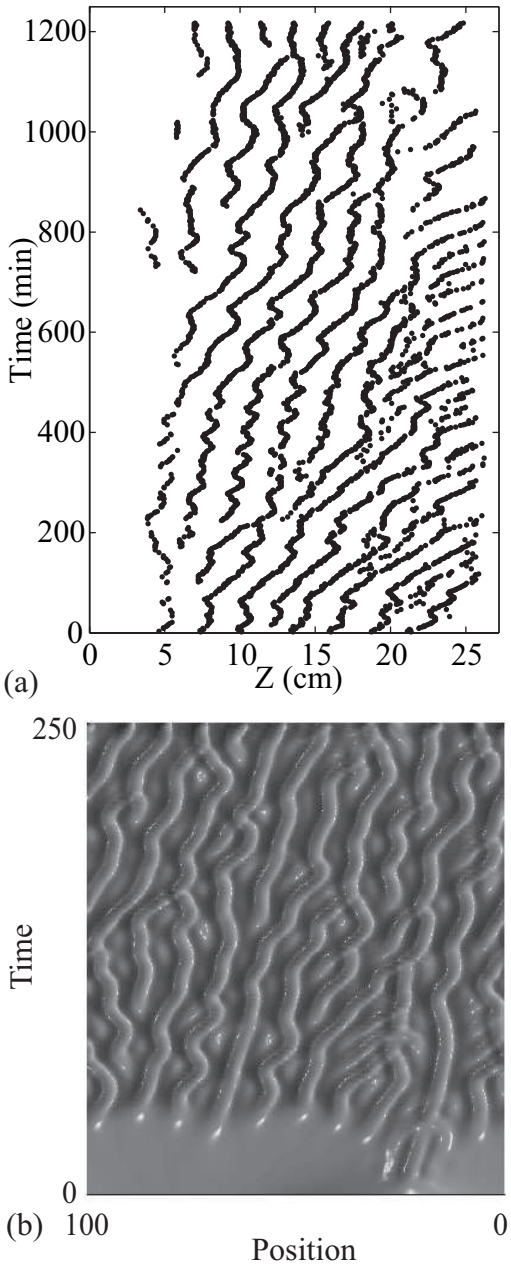

Figure A.1: Spatiotemporal location of concentration bands in free-surface Couette flow of a suspension (a) Forced with inclination angle 0.4^o. (b) Kuramoto-Sivashinsky solutions for $a = 0.03$, $b = 0.15$, and $c = 0$.

where a is greater than zero. We then substitute this into (A.1)

$$\frac{\partial\tilde{\phi}}{\partial t}+\beta\tilde{U}\frac{\partial\tilde{\phi}}{\partial x}=-\frac{(1-\beta)\rho g\tilde{\phi}}{\eta_o\eta_s}\frac{aA^3}{\phi_{max}}\cdot \left[\frac{\left(a+\frac{(a+1)A}{3}\right)}{\phi_{max}}\left(1-\frac{\tilde{\phi}}{\phi max}\right)^{-3a-2}\left(\frac{\partial\tilde{\phi}}{\partial x}\right)^2+\frac{1}{3}\left(1-\frac{\tilde{\phi}}{\phi_{max}}\right)^{-3a-1}\frac{\partial^2\tilde{\phi}}{\partial x^2}\right] \quad \text{(A.3)}$$

and group coefficients for simplicity,

$$\frac{\partial\tilde{\phi}}{\partial t}=-\beta\tilde{U}_\Delta\frac{\partial\tilde{\phi}}{\partial x}-\beta\tilde{U}_\alpha\frac{\partial\tilde{\phi}}{\partial x}-f_1(\tilde{\phi})\left(\frac{\partial\tilde{\phi}}{\partial x}\right)^2-f_2(\tilde{\phi})\left(\frac{\partial^2\tilde{\phi}}{\partial x^2}\right). \quad \text{(A.4)}$$

The variable $\tilde{U}$, and β are both functions of $\tilde{\phi}$. It is possible to think of $\tilde{U}$ as the sum of the fluid velocity caused by the local fluctuations in the film thickness ($\tilde{U}_\Delta$), and the fluid velocity caused by inclining the device ($\tilde{U}_\alpha$). This will prove useful later.

All of the terms on the right side of (A.4) are nonlinear. We will now attempt to find terms which could perform similar functions as the terms in the Kuramoto-Sivashinsky equation,

$$h_t=-h\cdot h_x-a-b\cdot h_x-h_{xx}-c\cdot h_{xxx}-h_{xxxx}$$

The nonlinear term in the Kuramoto-Sivashinsky equation ($h\cdot h_x$) is essential to obtain the chaotic dynamics shown in Figure 1.2 (c); in general, this term results in steepening of fronts [48]. This term is similar to the first term on the right side of Equation (A.4), $\beta\tilde{U}_\Delta\frac{\partial\tilde{\phi}}{\partial x}$, as $\tilde{U}_\Delta$ itself results from a fluctuation. The Kuramoto-Sivashinsky equation contains a diffusion term (h_{xx}) with a negative diffusion coefficient which causes growth. This is similar to the fourth term on the right hand side of (A.4), which although nonlinear, is a diffusion term with a negative diffusion coefficient. The h_{xxxx} term acts as a dissipation term which is known to strongly suppress short length scale features (large wavenumber in a Fourier transform). The model does not

contain a dissipation term although we note the third term on the right hand side of (A.4) acts as a consumption term. Since this term is nonlinear it does not consume equally across the domain. Through this nonlinearity this term will eliminate extreme excursions and in this sense perform some of the function of the dissipation term in the Kuramoto-Sivashinsky equation. It is important to note that all of the terms on the right side of (A.4) are nonlinear and through their interactions may not behave as expected in the analysis above.

Finally the Kuramoto-Sivashinsky equation exhibits a dynamics with regular and periodic structures moving axially because of the h_{xxx} term, and this behavior can also be caused by a term of the form h_x; the solution is numerically less stable with an h_x term in place of $-c \cdot h_{xxx}$. This is very similar to the second term on the right hand side of (A.4), $\beta \tilde{U}_\alpha \frac{\partial \tilde{\phi}}{\partial x}$. The $\tilde{U}$ term is driven by the down axis component of the fluid velocity when the system is inclined, and this overwhelms the nonlinear term, because the fluid velocity is simply down the axis of the device and not as sensitive to small fluctuations in the film thickness.

Analytical progress in solving the model proposed for the onset of banding in Chapter 4 has been made only for certain simple conditions. As noted above, numerical solutions have been obtained only for short times, never for sufficient time to allow the development of chaotic dynamics. Attempted solutions using finite difference or finite element techniques result in unbounded growth in the system. It is possible that more stable solutions could be found using spectral methods [20].

While it thus appears that the model we have proposed contains some of the necessary components to properly describe the concentration band dynamics we observe, more work is necessary to confirm this. Further effort is also needed to determine the model dynamics predicted for longer time. It is likely that the model proposed is insufficient in certain aspects, but the potential relation to Kuramoto-Sivashinksy

equation dynamics warrants further study. The complexity of the geometry in which we have reported the band migrations is a factor which must certainly be kept in mind: while an apparently similar mechanism for the band formation in the related single-cylinder geometry has been proposed [49], no report of similar chaotic dynamics has been made for this geometry, and the mechanism is not proposed in a form which allows ready assessment of whether such banding may in fact be predicted.

REFERENCES

[1] J F. Morris and F. Boulay. Curvelinear flows of noncolloidal suspensions: The role of normal stresses. *J. Rheol.*, 43:1213, 1999.

[2] C J. Koh, P. Hookham, and L G. Leal. Experimental investigation of concentrated suspension flows in a rectangular channel. *J. Fluid Mech.*, 266:1, 1994.

[3] M K. Lyon and L G. Leal. Experimental study of the motion of concentrated suspensions in two-dimensional channel flow. part 1. monodisperse systems. *J. Fluid Mech.*, 363:25, 1998.

[4] D. Leighton and A. Acrivos. Measurement of shear-induced self-diffusion in concentrated suspensions of spheres. *J.Fluid Mech.*, 177:109, 1987.

[5] J R. Abbott, N. Tetlow, A L. Graham, S A. Altobelli, E. Fukushima, L A. Mondy, and T S. Stephens. Experimental observations of particle migration in concentrated suspensions: Couette flow. *J. Rheol.*, 35:773, 1991.

[6] R J. Phillips, R C. Armstrong, R A. Brown, A. Graham, and J R. Abbott. A constitutive model for concentrated suspensions that accounts for shear-induced particle migration. *Phys. Fluids*, 4:31, 1992.

[7] P R. Nott and J F. Brady. Pressure-driven flow of suspensions: simulation and theory. *J. Fluid Mech.*, 275:157, 1994.

[8] D. Leighton and A. Acrivos. The shear-induced migration of particles in concentrted suspensions. *J.Fluid Mech.*, 181:415, 1987.

[9] J F. Morris and J F. Brady. Microstructure of stronly sheared suspensions and its impact on rheology and diffusion. *J. Fluid Mech.*, 348:103, 1997.

[10] J. Eggers. Nonlinear dynamics and breakup of free-surface flows. *Rev. Modern Phys.*, 69:865, 1997.

[11] K D. Danov, R. Aust, F. Durst, and U. Lange. Slow motions of a solid spherical particle close to a viscous interface. *Int. J. Multiphase Flow*, 21:1169, 1995.

[12] X. Li and C. Pozrikidis. Film flow of a suspension of liquid drops. *Phys. Fluids*, 14:61, 2002.

[13] X. Li and C. Pozrikidis. Film flow of suspension down an inclined plane. *Phil. Trans. R. Soc. Lond. A*, 361:847, 2003.

[14] X. Li and C. Pozrikidis. Wall-bounded shear flow and channel flow of suspensions of liquid drops. *Int. J. Mult. Flow*, 26:1247, 2000.

[15] T. Loimer, A. Nir, and R. Semiat. Shear-induced corrugation of free interfaces in concentrated suspensions. *J. Non-Newtonian Fluid Mech.*, 102:115, 2002.

[16] M. Tirumkudulu, A. Mileo, and A. Acrivos. Particle segregation in monodisperse sheared suspensions in a partially filled rotating horizontal cylinder. *Phys. Fluids*, 12:1615, 2000.

[17] M. Tirumkudulu, A. Tripathi, and A. Acrivos. Particle segregation in monodisperse sheared suspensions. *Phys. Fluids*, 11:507, 1999.

[18] B D. Timberlake and J F. Morris. Concentration band dynamics in free-surface couette flow of a suspension. *Phys. Fluids*, 14:1580, 2002.

[19] O A M. Boote and P J. Thomas. Effects of granular additives on transition boundaries between flow states of rimming flows. *Phys. Fluids*, 11:2020, 1999.

[20] L N. Threfethen. *Spectral methods in MATLAB*. Society for Industrial and Applied Mathematics, 2000.

[21] Z. Tasev and L. Kocarev. Synchronization of Kuramoto-Sivashinsky equations using spatially local coupling. *Int. J. Bifurcation and Chaos*, 10:869, 2000.

[22] B. Jin and A. Acrivos. Rimming flows with an axially varying viscosity. *Phys. Fluids*, 16:633, 2004.

[23] B D. Timberlake and J F. Morris. Film depth and concentration banding in free-surface couette flow of a suspension. *Phil. Trans. R. Soc. Lond. A*, 361:895, 2003.

[24] B. Jin and A. Acrivos. Theory of particle segregation in rimming flows of suspensions containing neutrally bouyant particles. *Phys. Fluids*, 16:641, 2004.

[25] F R. Pranckh and L E. Scriven. Elastohydrodynamics of blade coating. *AICHE J.*, 36:587, 1990.

[26] K. Ueda, H. Kanai, and T. Amari. Viscoelastic properties of paint films and formability in deep drawing of pre-painted steel sheets. *Progress in Organic Coatings*, 45:15, 2002.

[27] D B. Watson. Time lags in the impulse voltage breakdown of pmma at high temperatures. *J. Phys. D: Appl. Phys.*, 29:3129, 1996.

[28] Y. Li. Reforming the theory of invariant moments for pattern recognition. *Pattern Recognition*, 25:723, 1992.

[29] M. Born and E. Wolf. *Principles of optics : electromagnetic theory of propagation, interference and diffraction of light.* Cambridge University Press, 7th (expanded) edition, 1999.

[30] J A. Nelder and R. Mead. A simplex method for function minimization. *Comput. J.*, 7:308, 1965.

[31] J F. Morris and J F. Brady. Pressure-driven flow of a suspension: Buoyancy effects. *Int. J. Multiphase Flow*, 24:105, 1998.

[32] J F. Richardson and W N. Zaki. Sedimentation and fluidization: Part I. *Trans. Inst. Chem. Eng.*, 32:35, 1954.

[33] D A. Janes and N H. Thomas. On particle motions within rotating annular vessels. *Proceedings of Fluid Mixing IV Bradford, England September 1990*, 1990.

[34] T H. Cormen, C E. Leiserson, and R L. Rivest. *Introduction to Algorithms.* MIT Press, 1990.

[35] A. Falade. Hydrodynamic resistance of an arbirtary particle translating and rotating near a fluid interface. *Int. J. Multiphase Flow*, 12:807, 1986.

[36] S H. Lee and L G. Leal. Particle motion near a deformable fluid interface. *Adv. Colloid Interface Sci.*, 17:61, 1982.

[37] A S. Geller, S H. Lee, and L G. Leal. Creeping motion of a spherical particle normal to a deformable interface. *J. Fluid Mech.*, 169:27, 1986.

[38] M. Manga and H A. Stone. Low reynolds number motion of bubbles, drops, and rigid spheres through fluid-fluid interfaces. *J. Fluid Mech.*, 287:279, 1995.

[39] J. Blawzdziewicz, V. Cristini, and M. Loewenberg. Stokes flow in the presence of a planar interface covered with incompressible surfactant. *Phys. Fluids*, 11:251, 1999.

[40] I. Mutabazi, J J. Hegseth, C D. Andereck, and J E. Wesfried. Pattern formation in the flow between two horizontal coaxial cylinders with a partially filled gap. *Phys. Rev. A*, 38:4752, 1988.

[41] C. Normand, I. Mutabazi, and J E. Wesfried. Recirculation eddies in the flow between two horizontal coaxial cylinders with a partially filled gap. *Eur. J. Mech. B/Fluids*, 10:335, 1991.

[42] P J. Thomas, G D. Riddell, S. Kooner, and G P. King. Fine structure of granular banding in two-phase rimming flow. *Phys. Fluids*, 13:2720, 2001.

[43] R. Govindarajan, P R. Nott, and S. Ramaswamy. Theory of suspension segregation in partially filled horizontal cylinders. *Phys. Fluids*, 13:3517, 2001.

[44] V. Breedveld, D. van den Ende, A. Tripathi, and A. Acrivos. The measurement of the shear-induced particle and fluid tracer-diffusivities in concentrated suspensions by a novel method. *J. Fluid Mech.*, 375:297, 1998.

[45] D J. Foss and J F. Brady. Self-diffusion in sheared suspension by dynamic simulation. *J. Fluid Mech.*, 401:243, 1999.

[46] P. Lepoutre and D. Lord. Destabilized clay suspensions: Flow curves and dry film properties. *J. Colloid Interface Sci.*, 134:66, 1990.

[47] P G. Drazin and W H. Reid. *Hydrodynamic stability.* Cambridge University Press, 1981.

[48] G B. Whitham. *Linear and nonlinear waves.* Wiley-Interscience, 1974.

[49] B. Jin and A. Acrivos. Theory of particle segregation in rimming flows of suspensions containing neutrally bouyant particles. *Phys. Fluids*, 16:641, 2004.

VITA

Brian Davis Timberlake was born to Robert D. and Doris H. Timberlake in Silver Spring, Maryland on November 15, 1976. He lived in Beltsville, Maryland with his parents and younger brother until graduating from Eleanor Roosevelt High School in 1995. He studied Chemical Engineering at the University of Maryland in College Park, Maryland. Upon completion of his undergraduate work he moved to Atlanta and enrolled in graduate school in the School of Chemical Engineering at the Georgia Institute of Technology. He worked in the area of multiphase flow in the presence of free surfaces under the supervision of Dr. Jeffrey Morris. He was awarded a Ph.D. in May of 2004 for research on "Free-surface film flow of a suspension and a related concentration instability." He concurrently earned a Masters of Science in Quantitative and Computational Finance from the Georgia Institute of Technology in May of 2004. He is the co-author of three peer-reviewed journal articles and has given one oral presentation of his work at an academic conference. He was awarded a bronze medal in 2002 and a gold medal in 2003 for 4-way formation skydiving at the United States National Collegiate Skydiving Championship. He currently works for ING Investment Management in Atlanta.